

1-1-2012

Optical and Laser Spectroscopic Diagnostics for Energy Applications

Markandey Mani Tripathi

Follow this and additional works at: <https://scholarsjunction.msstate.edu/td>

Recommended Citation

Tripathi, Markandey Mani, "Optical and Laser Spectroscopic Diagnostics for Energy Applications" (2012).
Theses and Dissertations. 3382.
<https://scholarsjunction.msstate.edu/td/3382>

This Dissertation - Open Access is brought to you for free and open access by the Theses and Dissertations at Scholars Junction. It has been accepted for inclusion in Theses and Dissertations by an authorized administrator of Scholars Junction. For more information, please contact scholcomm@msstate.libanswers.com.

OPTICAL AND LASER SPECTROSCOPIC DIAGNOSTICS FOR ENERGY
APPLICATIONS

By

Markandey Mani Tripathi

A Dissertation
Submitted to the Faculty of
Mississippi State University
in Partial Fulfillment of the Requirements
for the Degree of Doctor of Philosophy
in Engineering with an Emphasis in Applied Physics
in the Department of Physics and Astronomy

Mississippi State, Mississippi

May 2012

Copyright by
Markandey Mani Tripathi
2012

OPTICAL AND LASER SPECTROSCOPIC DIAGNOSTICS FOR ENERGY
APPLICATIONS

By

Markandey Mani Tripathi

Approved:

Sundar R. Krishnan
Assistant Professor,
Mechanical Engineering, and
Adjunct Assistant Professor,
Department of Physics and Astronomy
(Major Professor)

Jagdish P. Singh
Research Professor, Emeritus,
Energy Institute, and
Department of Physics and Astronomy
(Dissertation Director)

Kalyan K. Srinivasan
Assistant Professor,
Mechanical Engineering
(Minor Professor)

Chuji Wang
Associate Professor,
Department of Physics and Astronomy
(Committee Member)

David L. Monts
Professor,
Department of Physics and Astronomy
(Committee Member and Graduate
Coordinator)

Sarah A. Rajala
Dean of the Bagley College of Engineering

Name: Markandey Mani Tripathi

Date of Degree: May 12, 2012

Institution: Mississippi State University

Major Field: Engineering with an Emphasis in Applied Physics

Major Professor: Dr. Sundar R. Krishnan

Title of Study: OPTICAL AND LASER SPECTROSCOPIC DIAGNOSTICS FOR
ENERGY APPLICATIONS

Pages in Study: 158

Candidate for Degree of Doctor of Philosophy

The continuing need for greater energy security and energy independence has motivated researchers to develop new energy technologies for better energy resource management and efficient energy usage. The focus of this dissertation is the development of optical (spectroscopic) sensing methodologies for various fuels, and energy applications.

A fiber-optic NIR sensing methodology was developed for predicting water content in bio-oil. The feasibility of using the designed near infrared (NIR) system for estimating water content in bio-oil was tested by applying multivariate analysis to NIR spectral data. The calibration results demonstrated that the spectral information can successfully predict the bio-oil water content (from 16% to 36%).

The effect of ultraviolet (UV) light on the chemical stability of bio-oil was studied by employing laser-induced fluorescence (LIF) spectroscopy. To simulate the UV light exposure, a laser in the UV region (325 nm) was employed for bio-oil excitation. The LIF, as a signature of chemical change, was recorded from bio-oil. From this study, it

was concluded that phenols present in the bio-oil show chemical instability, when exposed to UV light.

A laser-induced breakdown spectroscopy (LIBS)-based optical sensor was designed, developed, and tested for detection of four important trace impurities in rocket fuel (hydrogen). The sensor can simultaneously measure the concentrations of nitrogen, argon, oxygen, and helium in hydrogen from storage tanks and supply lines. The sensor had estimated lower detection limits of 80 ppm for nitrogen, 97 ppm for argon, 10 ppm for oxygen, and 25 ppm for helium.

A chemiluminescence-based spectroscopic diagnostics were performed to measure equivalence ratios in methane-air premixed flames. A partial least-squares regression (PLS-R)-based multivariate sensing methodology was investigated. It was found that the equivalence ratios predicted with the PLS-R-based multivariate calibration model matched with the experimentally measured equivalence ratios within 7 %.

A comparative study was performed for equivalence ratios measurement in atmospheric premixed methane-air flames with ungated LIBS and chemiluminescence spectroscopy. It was reported that LIBS-based calibration, which carries spectroscopic information from a “point-like-volume,” provides better predictions of equivalence ratios compared to chemiluminescence-based calibration, which is essentially a “line-of-sight” measurement.

DEDICATION

To my parents,

Smt. (Late) Girija and Shri Yogendra Mani Tripathi,

whose blessings have always invigorated me at every step of my life

and, my wife

Alka

for all of her love, care, and support.

ACKNOWLEDGEMENTS

I would like to express my deepest gratitude to Dr. Jagdish P. Singh, my dissertation director. His endless support and continued encouragement have been the key components in the fructification of this dissertation work. I sincerely thank Dr. Sundar R. Krishnan for being the major advisor of my doctoral dissertation. Dr. Krishnan has ensured that he provides every possible guidance and help during my doctoral research, even in his busiest schedule. I cannot forget our “telephonic meetings” at several occasions to provide immediate help. I also thank Dr. Kalyan K. Srinivasan for co-advising my research. I have received some very practical suggestions from him on academic (and other) issues. I thank Dr. David L. Monts for his exemplary role as a teacher and as a graduate advisor. I thank Dr. Chuji Wang for readily accepting to serve as a committee member.

I thank to our group member Ms. Fang-Yu Yueh for her indispensable help and assistance at numerous occasions during my doctoral research. I appreciate the support offered by my former and current colleagues, Dr. Vidhu Tiwari, Dr. Kemal Eseller (Efe), Mr. Tracy Miller, Mr. Krishna Kanth Ayyalasomayajula, Mr. Pavan Srungaram, Mr. Charles Ghany, among others. I thank to the staff of the Energy Institute’s engineering shop for their assistance during various projects. I especially thank Mr. John Cambre for making several custom-instruments for my experiments. I thank Ms. Linda Schubert,

Ms. Mary Ann Richardson, Mr. Andrew Fox, Ms. Paula Jordan, and Ms. Connie Vaughn for their administrative assistance.

I acknowledge the financial support provided for my research by the Sustainable Energy Research Center (SERC) at Mississippi State University, NASA Stennis Space Center–Small Business Technology Transfer (SSC-STTR) program. I also thank our Department of Physics and Astronomy for providing me teaching assistant position for partial part of my doctoral program.

I thank the Bagley College of Engineering writing tutors Ms. Courtney Baroni, Ms. Courtney Tucker, and Mr. Joshua Bryant for the careful proofreading of this dissertation.

I am indebted to my family and friends for their love, support and encouragement during this long journey. Above all, I owe all my accomplishments, academic and otherwise, to my parents Smt. (Late) Girija and Shri Yogendra Mani Tripathi. The sacrifices made by them have taken me this far in my life. Also, I record my sincere gratitude to my extended family whose contribution cannot be ignored. I thank all my friends for being part of my life. How can I forget the better half of my life, my wife, Alka; who came in my life in the last (but not the least) part of this endeavor. From thereon, she has been the continuous source of encouragement and inspiration.

Finally, I thank God for blessing me with the strength, courage and determination, without which, I would have never reached here... HAR HAR MAHADEV!

TABLE OF CONTENTS

DEDICATION	ii
ACKNOWLEDGEMENTS	iii
LIST OF TABLES	viii
LIST OF FIGURES	ix
CHAPTER	
I. INTRODUCTION	1
Theoretical Background	4
Near-Infrared Spectroscopy	4
Laser-Induced Fluorescence Spectroscopy	7
Laser-Induced Breakdown Spectroscopy	9
Flame Chemiluminescence Spectroscopy	13
Multivariate Data Analysis	16
Principal Component Regression	18
Partial Least Squares Regression	20
Multiplicative Scattering Correction	20
Research Motivation and Specific Objectives	21
Organization of the Dissertation	23
References	26
II. REFLECTION–ABSORPTION-BASED NEAR INFRARED SPECTROSCOPY FOR PREDICTING WATER CONTENT IN BIO-OIL *	28
Abstract	28
Introduction	29
Experimental	31
Pre-Design NIR Experiments	31
Fiber Optic System Configuration	33
Bio-Oil Preparation	35
Bio-Oil Characterization	35

Testing Samples	36
Multivariate Data Analysis	37
Results and Discussions	38
Principal Component Regression (PCR) Model	42
Partial Least Squares (PLS) Model	44
Conclusion	46
Acknowledgement	47
References	48
III. A STUDY OF THE EFFECT OF ULTRAVIOLET EXPOSURE ON BIO-OIL BY LASER-INDUCED FLUORESCENCE SPECTROSCOPY*	50
Abstract	50
Introduction	51
Experimental	52
Bio-Oil Sample Preparation	52
Experimental Setup	55
Synthetic Bio-Oil	57
Results and Discussion	58
Conclusion	66
Acknowledgement	66
References	67
IV. AN OPTICAL SENSOR FOR MULTI-SPECIES IMPURITY MONITORING IN HYDROGEN FUEL*	69
Abstract	69
Introduction	70
Experimental	72
Optical System Design	74
Sensor Control & Operation Software	75
Results and Discussion	77
Sample Cell Pressure	81
Sensor Calibration	82
Sensor Operation	83
Conclusion	86
Acknowledgements	87
References	88
V. CHEMILUMINESCENCE-BASED MULTIVARIATE SENSING OF LOCAL EQUIVALENCE RATIOS IN PREMIXED ATMOSPHERIC METHANE-AIR FLAMES*	89

Abstract.....	89
Introduction.....	90
Specific Objectives	93
Experimental Setup.....	93
Data Analysis	96
Results and Discussion	98
Intensity Ratio Calibration.....	102
Multivariate Calibration.....	105
Prediction of Equivalence Ratios from Unknown Spectral Data Set	111
Discussion of the Practical Implications of the Present Work.....	114
Conclusions.....	116
Acknowledgments.....	118
References.....	119
VI. A COMPARISON OF MULTIVARIATE LIBS AND CHEMILUMINESCENCE BASED LOCAL EQUIVALENCE RATIO MEASUREMENTS IN METHANE-AIR PREMIXED FLAMES*	121
Abstract.....	121
Introduction.....	122
Specific Objectives	125
Experimental Setup.....	125
Data Analysis	128
Results and Discussion	130
Performance Comparison of Notch Filter and Polarizer for Ungated LIBS Detection	130
Univariate Calibration of LIBS Spectra.....	132
Multivariate Calibration of LIBS spectra	138
Comparison of the Predictive Power of LIBS Intensity Ratio Calibration, Multivariate LIBS Calibration, and Multivariate Chemiluminescence Calibration	144
Conclusions.....	146
Acknowledgments.....	148
References.....	150
VII. SUMMARY AND RECOMMENDATIONS FOR FUTURE RESEARCH	152
Research Summary	152
Recommendations for Future Research	156

LIST OF TABLES

1.1	Common chemiluminescence emission spectra observed in flames	15
2.1	Physical properties and molecular weight of raw pine lumber (bio-) oil	36
2.2	Water content (%) in testing samples measured with Karl Fisher titration.....	37
2.3	PCR model results for prediction of water concentration in bio-oil with Full Cross Validation and Test Set Validation	43
2.4	PLS model results for prediction of water concentration in bio-oil with Full Cross Validation and Test Set Validation	44
3.1	Main characteristics of biomass feed stocks.....	53
3.2	Yields of the studied bio-oil.....	54
3.3	Physical and chemical properties for the bio-oil produced from four studied feed stocks	54
3.4	Chemical composition of synthetic bio-oil.....	61
4.1	Atomic spectral lines of various impurities	77
5.1	List of equivalence ratios considered in the development of both the intensity ratio and the multivariate calibration models.....	99
6.1	Equivalence ratios considered in the LIBS experiments and the corresponding uncertainties	133

LIST OF FIGURES

1.1	Comparison of three vibrational spectroscopic techniques with energy level diagram.....	6
1.2	Jablonski energy diagram	8
1.3	Laser-sample interaction.....	11
1.4	Pictorial description of laser-induced breakdown spectroscopy.....	13
1.5	X variables in NIR absorption spectra collected from different bio-oil samples.....	17
1.6	Principal components for three-dimensional data.....	19
1.7	Pictorial representation of principal component regression.....	19
1.8	Pictorial representation of partial least squares regression.....	20
2.1	Comparison of NIR intensity spectra of bio-oil from diffuse reflection and reflection absorption setups.....	32
2.2	Schematic of fiber optic (near infrared) NIR system. Its components are (1) NIR broad-band source, (2) NIR detector, (3) Y-shaped optical fiber reflection probe, (4) glass slides, (5) metallic ring, (6) metallic strips, (7) illumination fibers, (8) read fiber, (9) probe end, and (10) note book computer	34
2.3	Plot of reflection-absorption NIR spectrum from bio-oil with different water content.....	40
2.4	Variation of spectral peak intensity with water concentration at 1446.14 and 1935.45 nm spectral peaks	41
2.5	Plot of multiple scattering corrected (MSC) reflection-absorption NIR spectrum from bio-oil with different water concentrations	42

2.6	PLS regression model for predicting water content in bio-oil in the 1300–2000 nm spectral range using multiple scattering correction (MSC) and test validation set	46
3.1	Schematic of the Mississippi State University small-scale auger reactor system	55
3.2	Experimental setup for bio-oil study.....	56
3.3	LIF spectrums of Pine Lumber Oil with (a) 532 laser excitation (b) 442 laser excitation	58
3.4	LIF spectra of bio-oil samples on excitation with 325 nm laser.....	60
3.5	Variation in intensity of synthetic bio-oil after exciting it with 325 nm laser (a) Fisk <i>et al.</i> composition (b) Composition used in the present study (Given in Table 3.4).....	63
3.6	Variation of LIF peak intensity with time in studied bio-oils.....	64
3.7	LIF spectra of individual ingredients of synthetic bio-oil	65
4.1	4.1a Schematic diagram of LIBS optical sensor; 4.1b Inner view of LIBS optical sensor box.....	73
4.2	Graphical user interface of optical sensor controlling software	76
4.3	LIBS spectra of hydrogen sample (with nitrogen 10000 ppm, argon 5000 ppm, oxygen 400 ppm, and helium 5000 ppm) in 764 nm spectral region.....	78
4.4	LIBS spectra of hydrogen sample (with nitrogen 10000 ppm, argon 5000 ppm, oxygen 400 ppm, and helium 5000 ppm) in 577 nm spectral region.....	79
4.5	LIBS spectra recorded with and without notch filter.....	80
4.6	Effect of leaking hydrogen spectral line on helium spectral line at different pressure in sample cell	81
4.7	Optical sensor calibration with LIBS spectra (a) for nitrogen concentration measurement, (b) for argon concentration measurement, (c) for oxygen concentration measurement, and (d) for helium concentration measurement.....	83
4.8	Flow chart describing operation of the optical sensor	84
5.1	Schematic diagram of the experimental setup	94

5.2	Chemiluminescence spectra of premixed atmospheric methane-air flames at different measured equivalence ratios	100
5.3	Variation of chemiluminescence peak intensities for OH [*] , CH [*] , and C ₂ [*] with measured equivalence ratio	102
5.4	Correlation of background-corrected OH [*] /CH [*] intensity ratio with measured equivalence ratio	104
5.5	Residual validation Y-variance vs. number of principal components (PCs) used in the development of the PLS-R based multivariate calibration model	105
5.6	Comparison of equivalence ratios predicted with PLS-R based multivariate calibration model (using the calibration data set) and measured equivalence ratios	106
5.7	One-vector loading-weight plots along the three PCs for the developed PLS-R based multivariate calibration model	109
5.8	Comparison of equivalence ratios predicted using intensity ratio model (exponential decay curve from Equation 5.3) and measured equivalence ratios for an unknown data set	113
5.9	Comparison of equivalence ratios predicted using PLS-R-based multivariate calibration model and measured equivalence ratios for an unknown data set	114
6.1	Schematic diagram of the experimental setup for LIBS based equivalence ratio measurements	128
6.2	Comparison of LIBS spectra collected from methane-air premixed flame with a notch filter and a polarizer	132
6.3	Variation of spectral peak intensities of hydrogen (H _{656 nm}), nitrogen (N ⁺ _{500 nm}), and oxygen (O _{777 nm}) with measured equivalence ratio in LIBS spectra	135
6.4	Correlation of H _{656 nm} /N ⁺ _{500 nm} and H _{656 nm} /O _{777 nm} intensity ratios with measured equivalence ratio	138
6.5	Residual validation Y-variance vs. number of principal components (PCs) used in the development of the PLS-R based multivariate calibration on LIBS spectra	141

6.6	PLS-R based prediction of equivalence ratios while validating the developed multivariate calibration model with LOOCV (using the calibration data set)	142
6.7	One-vector loading-weight plots for the developed PLS-R based multivariate calibration model on LIBS spectra	144
6.8	Prediction results from $H_{656 \text{ nm}}/N_{500 \text{ nm}}^+$ intensity ratio calibration, $H_{656 \text{ nm}}/O_{777 \text{ nm}}$ intensity ratio calibration, PLS-R based multivariate calibration, and Chemiluminescence based multivariate calibration	149

CHAPTER I

INTRODUCTION

Optical spectroscopy is a branch of science that studies the radiative emission from a physical phenomenon or object in order to extract qualitative/quantitative information about its properties. This radiative emission could be from a chemical reaction (chemiluminescence), plasma formation (optical emission), or interaction of radiation with an object or a phenomenon. The spectroscopy based on the interaction of radiation with an object or a phenomenon can be further classified into two categories: scattering of radiation and absorption (or emission) of radiation. The spectroscopy based on scattering of the radiation includes Raman scattering, Rayleigh scattering, and Mie scattering. The spectroscopy based on absorption of radiation includes ultraviolet/visible/infrared absorption spectroscopy, cavity ringdown spectroscopy (CRDS), Mössbauer absorption spectroscopy, etc. Emission spectroscopy methods (depending on the interaction of radiation with an object or a phenomenon) include laser-induced fluorescence (LIF) spectroscopy, laser-induced breakdown spectroscopy (LIBS), and laser induced incandescence (LII) spectroscopy, amongst others [1].

Optical spectroscopy is widely employed as a diagnostic or sensing tool for a variety of applications. When applied to fuels and combustion processes, it can be classified into two categories: optical sensing of the fuel and optical diagnostics of the

fuel combustion process. Several optical-sensing methodologies have been employed on various fuels to provide information about fuel quality and impurity contamination [2]. For instance, ultraviolet–visible light absorption and fluorescence spectroscopy were recently employed by Commodo *et al.* to study the thermal oxidative stability of jet fuel [3]. Thermal oxidative stability of jet fuel is an important parameter due to jet fuel's (unburned jet fuel's) additional role as a heat sink to remove waste heat apart from its conventional role as an energy source in modern aircrafts. Cramer *et al.* used near-infrared spectroscopy in association with partial least-squares regression to predict the content of Fischer–Tropsch (FT) synthetic fuels and biofuels in blends with petroleum-derived fuels [4]. The bulk properties of the blend can be easily characterized from information about the concentrations of FT synthetic fuel and biofuel. Fourier transform mid-infrared spectroscopy and Fourier transform near-infrared spectroscopy have been explored to evaluate the quality of ethanol fuel in the form of hydrated ethyl alcohol (AEHC, AEHC acronym is obtained from Spanish, specifically Alcool Etilico Hidratado Combustivel) and to detect the adulteration of AEHC with methanol [5]. This technique can provide a fast and precise measurement of low price (but highly toxic) methanol which is difficult to detect (due to the fact that methanol has physical and chemical properties that are very similar to ethanol). Flecher *et al.* have reported the application of fiber optic Raman spectroscopy for the determination of octane number in commercial gasoline [6]. The octane number is an important parameter that quantifies the anti-knock properties of gasoline. Spectrophotometry, in association with chemometrics, has been employed to determine the ASTM (American Society for Testing and Materials) color of automotive diesel fuel [7]. The ASTM color is an important parameter that can be

analyzed to determine the quality of diesel fuel. A change in color may be indicative of contamination, degradation, or adulteration or other problems during fuel production.

Spectroscopy has long been employed for combustion diagnostics [8]. Typically, this involves the spectroscopic study of intermediate species (such as OH^* , CH^* , C_2^* , CO_2^* , etc.) formed in the flame to characterize the combustion process and to measure important variables such as: flame temperature, fuel concentration, fuel composition, equivalence ratio (which is defined as the mass-ratio of air-to-fuel required for complete combustion of the fuel divided by actual mass-ratio of air-to-fuel present in the combustion environment), and exhaust gas composition. Cheskis *et al.* [9] have shown the application of cavity ringdown spectroscopy to the measurement of OH radical in low pressure methane-air flames. Spectroscopic investigations of chemiluminescence emissions in flames have also been performed for combustion diagnostics. For example, Nori *et al.* performed CH^* chemiluminescence modeling of methane-air premixed flames [10]. They discussed the possibility of sensing the equivalence ratio and heat release rate with CH^* chemiluminescence. Laser-induced breakdown spectroscopy has also been employed for sensing the equivalence ratio in premixed flames [11]. Spectroscopic combustion diagnostics have also been explored for monitoring the health of the combustors. Recently, Scherewe *et al.* have employed planar laser-induced fluorescence (PLIF) spectroscopy to investigate the role of thermal boundary layers on homogeneous charge compression ignition (HCCI) combustion [12]. The PLIF was used to measure the spatial profile of formaldehyde concentrations near the engine cylinder walls. This measurement can provide information on the influence of thermal boundary layers on HCCI combustion process.

The research work presented in this dissertation primarily employed four optical spectroscopic techniques: NIR absorption spectroscopy, LIF spectroscopy, LIBS spectroscopy, and flame chemiluminescence spectroscopy. In the next section, a brief theoretical background of each technique is discussed.

Theoretical Background

Near-Infrared Spectroscopy

Infrared spectroscopy is a vibrational spectroscopic technique that provides qualitative, and/or quantitative information about the sample system by utilizing vibrational properties of the constituent molecules. Molecular vibrations can be described in a very simplified (yet approximate) way by taking a diatomic molecule harmonic oscillator model [13]. With the harmonic oscillator approximation, the vibrational frequency (ν) can be correlated with the molecular parameters as:

$$\nu = \frac{1}{2\pi} \sqrt{\frac{f}{\mu}} \quad (1.1)$$

where, f is the force constant that reflects the strength of the bond between atomic nuclei of masses m and M . The reduced mass μ is given by

$$\mu = \frac{mM}{m + M} \quad (1.2)$$

Raman spectroscopy (4000-50 cm^{-1}), mid-infrared spectroscopy (4000-400 cm^{-1}), and near-infrared spectroscopy (12500-4000 cm^{-1}) are the three major vibrational spectroscopic techniques amongst others. A comparison of all three vibrational spectroscopic techniques is presented in Figure 1.1 using an energy level diagram. This

figure shows the potential energy curves of the electronic ground state. Various vibrational levels are shown by their vibrational quantum number $v = 0, 1, 2, 3$, etc. In Raman spectroscopy, the radiation interacts with the molecular vibrations and drives the molecules into a virtual excited energy state (see Figure 1.1a). Thereafter, the molecule returns to the ground electronic state, but to a different vibrational energy level and a shift in the radiation energy (known as the Raman shift) is observed depending on the vibrational mode. Mid-infrared spectroscopy utilizes the fundamental frequency of the molecular vibrations. The molecule absorbs mid-infrared radiation (of wavelength 2500-25000 nm) and is driven from the lowest vibrational state (v_0) to the second vibrational state (v_1) as shown in the Figure 1.1b. In near-infrared spectroscopy, the molecule absorbs near-infrared radiation and occupies vibrational states that correspond to vibrational overtones (see Figure 1.1c). The vibrational overtones of an energy level with fundamental frequency ν_0 will be the vibration states with frequencies $2\nu_0, 3\nu_0$, etc. Near-infrared absorption can also occur at combination of several vibrational modes. A combination of vibrational modes with frequencies ν_0 , and ν_1 could be a vibrational level with frequency $\nu_0 + \nu_1, 2\nu_0 + \nu_1, \nu_0 + 2\nu_1$, etc.

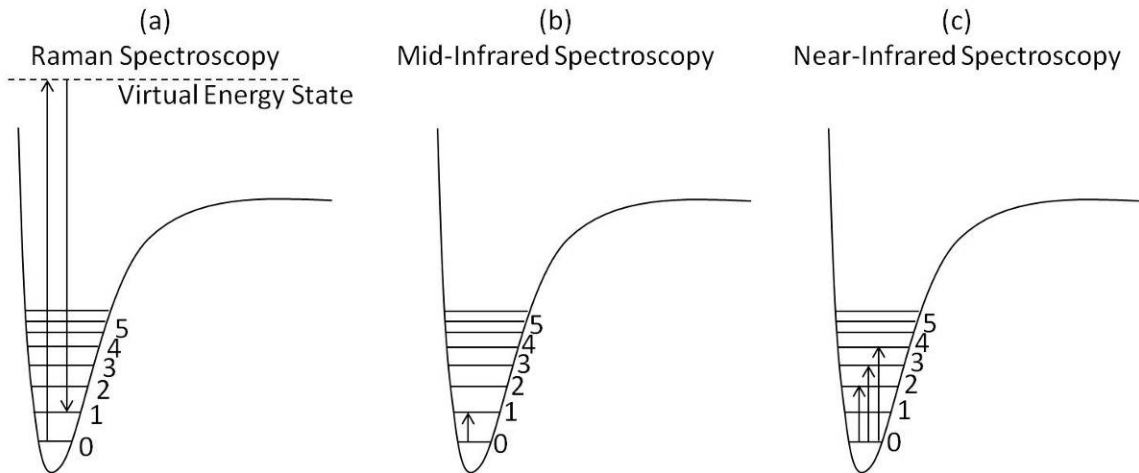


Figure 1.1

Comparison of three vibrational spectroscopic techniques with energy level diagram

Some of the advantages of the near-infrared spectroscopy are as follows:

- It is a non-destructive, contact-free technique that can perform real time analysis with cost-effective instrumentation.
- It requires minimal or no sample preparation, which is a big advantage over mid-infrared spectroscopy (other vibrational spectroscopic technique) that requires individual sample preparation steps before data acquisition.
- It can penetrate deeper in comparison to mid-infrared spectroscopy due to shorter wavelength; which makes it an ideal tool for probing bulk materials.
- Near-infrared spectroscopy coupled with multivariate data analysis can perform multi-component analysis in a sample and it can analyze complex samples as well.

Laser-Induced Fluorescence Spectroscopy

Luminescence is the emission of light from a substance after absorption of light. It can be further divided into two categories – fluorescence and phosphorescence – depending on the electronic states involved in the transition. The process of absorption and emission of light can be explained with the help of a Jablonski diagram (Figure 1.2) which was named after Professor Alexander Jablonski, who is regarded as the father of fluorescence spectroscopy [14].

In Figure 1.2, four different electronic states of a molecule are shown: singlet ground state (S_0), first singlet excited state (S_1), second singlet excited state (S_2), and first triplet excited state (T_1). A triplet state consist three quantum states differentiated by their spin orientation. In each electronic state, different vibrational states are shown by the vibrational quantum numbers 0, 1, 2, 3, etc. Various transitions are shown by vertical lines. Once a molecule absorbs light of the appropriate wavelength, it goes into some vibrational level of one of the excited states. For instance, Figure 1.2 shows that the molecule can absorb radiation A_1 and enters the vibrational state 3 of electronic state S_1 , or the vibrational state 2 of electronic state S_2 with absorption of radiation A_2 . In most of the cases, the molecule stays in this excited state for a very short period of time ($\sim 10^{-12}$ second), and it rapidly returns to the lowest vibrational state of S_1 through a process called internal conversion. From S_1 , the molecule returns to one of the vibrational states of the ground state via radiative emission (F_1 and F_2), which is called fluorescence. Typical life time of fluorescence is of the order 10^{-8} second. If a laser is used as an excitation source, then the fluorescence is called laser-induced fluorescence.

The molecule from S_1 can also go to the triplet state T_1 (if it has a similar energy as S_1). This phenomenon is known as inter-system crossing. If the molecule transfers from T_1 to S_0 via radiative transition, then this emission is called phosphorescence (P_1 , P_2). Generally, phosphorescence occurs at higher wavelengths (lower energy) compared to fluorescence. Phosphorescence has a higher lifetime (up to several seconds) due to forbidden transition between T_1 and S_0 . The higher lifetimes associated with the forbidden transitions are due to the lower probability of its occurrence (as these transitions are not allowed by normal selection rules of quantum mechanics).

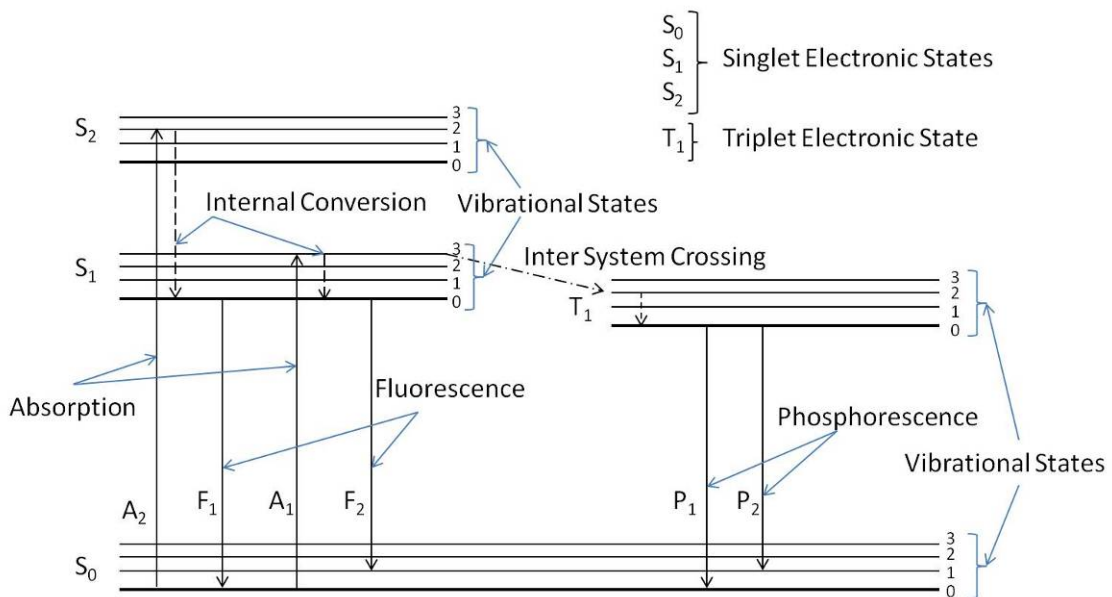


Figure 1.2

Jablonski energy diagram

Typically, the information obtained from LIF can also be obtained from absorption spectroscopy. However, there are some advantages of laser-induced fluorescence spectroscopy as listed below:

- It has very high selectivity in comparison to broadband absorption spectroscopy due to single wavelength excitation.
- It has a high signal-to-noise ratio as emission occurs at a wavelength that is different from the excitation wavelength.
- It is highly linear in a wide wavelength range so can be used to perform quantitative measurements.
- It is a non-invasive technique that can be performed real time.

Laser-Induced Breakdown Spectroscopy

When a high power laser pulse of irradiance 10^9 - 10^{11} W/cm² interacts with air or any other gaseous pure component or mixture; a spark is produced due to photoelectric breakdown in the gases from the electric field associated with the laser pulse. The typical threshold of the electric field required for breakdown to occur is of the order of 10^6 - 10^7 V/cm. This spark generation will be followed by charged particle production, laser light absorption, and re-radiation of the light from the spark. This phenomenon is called laser-induced breakdown in analogy with an electrical breakdown. In the case of solids, the breakdown mechanism is a little different since a plasma plume is produced due to rapid melting and/or vaporization of the sample due to its interaction with high-power laser pulse. X-ray emissions can also be observed at the point of breakdown if the temperature of the plasma is high enough at that location. The phenomenon of the breakdown can be

understood as a two-step process: first, the production of the initial ionization and second, the subsequent cascade by which the ionization grows, resulting in the breakdown. Multi-photon ionization is considered to be a plausible mechanism for the initial ionization, where simultaneous absorption of many quanta by an atom produces an ion-electron pair. The absorption of a photon by an atom may be visualized in two equivalent ways: (1) it can be considered as an inverse Bremsstrahlung process in which a single light quantum is absorbed by an electron in the field of an atom or ion. (2) Also, it can be considered as analogous to microwave-generated breakdown, in which the electron oscillates in the electric field of the incident radiation. Figure 1.3 shows the process of laser interaction with matter.

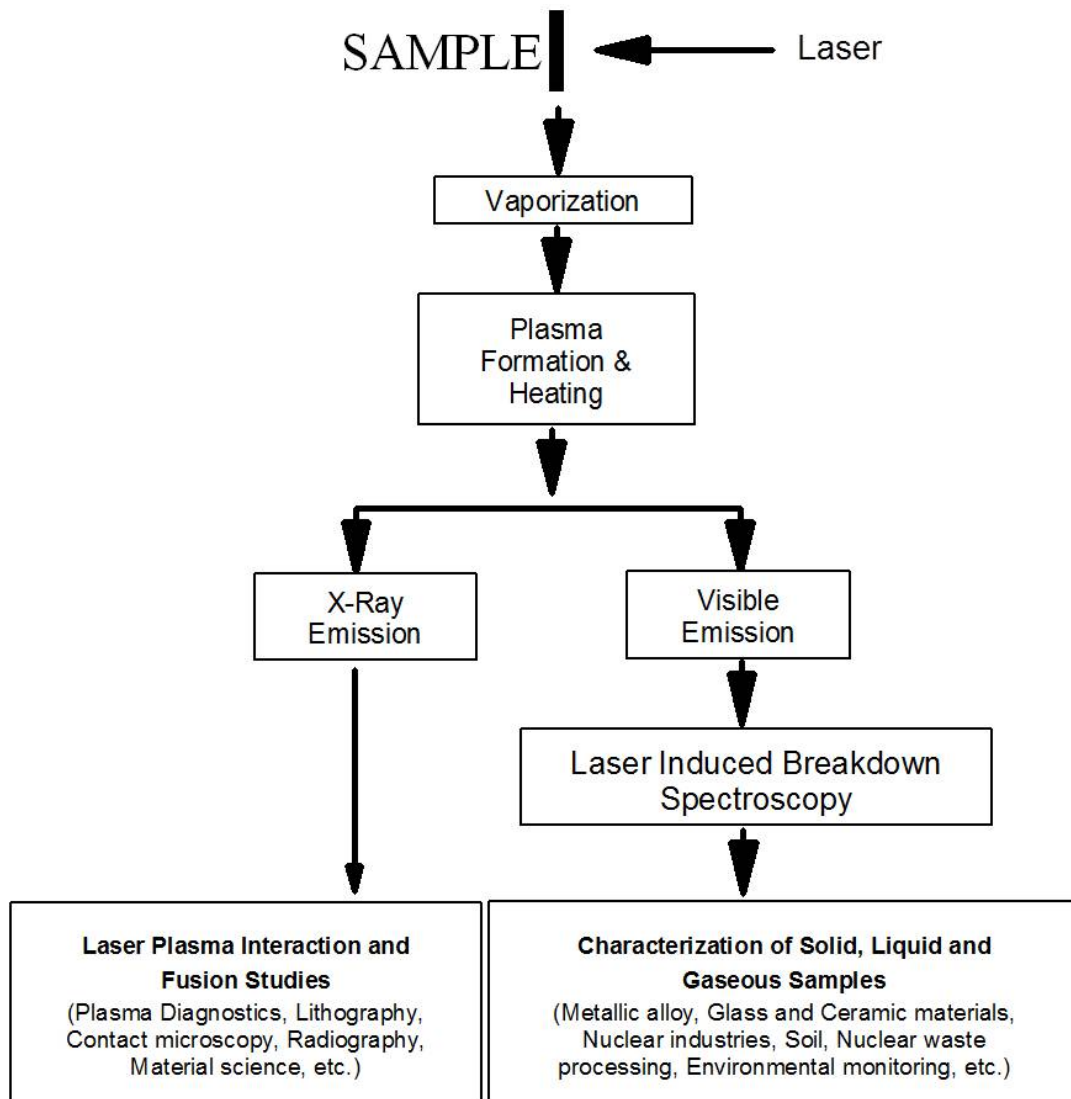


Figure 1.3

Laser-sample interaction

Optical spectroscopy of laser-induced plasmas shows both continuum and line emissions. The emission of the continuum radiation (in the spectral range of 2 nm to 600 nm) originates near the sample surface. The line spectrum shows the presence of highly ionized atoms as well as neutral atoms. The most highly ionized species are present near the plasma center, while lines of lower ionization and neutral species are observed near

the outer regions of the plasma plume. The spectra of neutral atoms are found to originate in a larger spatial region, indicating that neutral atom emission dominates after the plasma has expanded and cooled. The time variation of spectral line intensities indicates that the highest ionized states are present fairly early and that lower ionized states appear later [15].

The entire process of laser-induced breakdown spectroscopy in a sample can be summarized as follows:

- High energy laser pulse is tightly focused in a small control volume of micron order.
- The high irradiance imposed by laser pulse creates breakdown in the sample resulting into the formation of micro-plasma.
- The excited atoms/ions present in the plasma emit light at their characteristic wavelengths.
- Spectral analysis of the emission spectrum from the plasma is used to infer the elemental composition of the sample.

A pictorial description of LIBS is shown in Figure 1.4. Some of the advantages of laser-induced breakdown spectroscopy (LIBS) are as follows:

- The LIBS is experimentally simple. Hence, it can be useful in hazardous and/or otherwise inaccessible situations
- It has a very fast response and the results are available immediately.
- It requires almost no sample preparation.
- A single-ended transmitter/receiver can make the LIBS system compact enough for field applications.

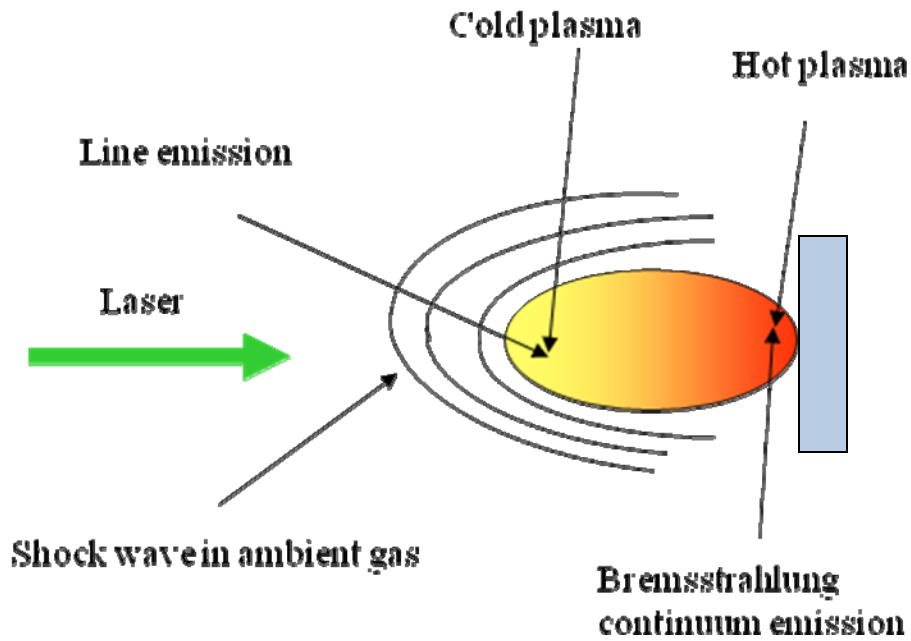


Figure 1.4

Pictorial description of laser-induced breakdown spectroscopy

Flame Chemiluminescence Spectroscopy

Chemiluminescence is defined as emission of radiation due to specific chemical species generated in the chemical reactions. For instance, in combustion processes, a visible flame occurs due to several chemical reactions [16]. An example of a chemical reaction responsible for most of the visible radiation in the flame is the combustion of CO in the presence of oxygen -



Study of flame chemiluminescence can provide important details about the combustion process. For example, it can help in understanding the chemical kinetics associated with the combustion process. High resolution chemiluminescence spectra can

also provide indirect measurements of flame temperature in some flames where the flame temperature is equal to the rotational and vibrational temperature corresponding to the spectral emission from a specific species. For instance, it has been observed [17] that OH^* in H_2 -air premixed flames and CH^* in CH_4 -air premixed flames can provide good estimates of flame temperature [18]. However, flame temperature measurements based on chemiluminescence emission should be performed carefully as they may involve substantial errors under certain conditions. For instance, it has been observed that the OH^* spectra over predicts flame temperature in the case of CH_4 -air premixed flames [19]. In addition to flame temperature measurements, it has also been observed [20] that in some flames (specifically premixed hydrocarbon flames), the spectral intensities of chemiluminescence peaks are dependent on the fuel-air equivalence ratio of the burning mixture. So, chemiluminescence spectra can be employed to measure the local equivalence ratios in the burning mixture. Some of the most common chemiluminescence spectra observed in flames are listed in Table 1.1 [16, 21]. The bold font in “Spectral Wavelength” column in the table represents wavelength of the highest intensity in the spectral band.

Table 1.1

Common chemiluminescence emission spectra observed in flames

Species	Transition (Lower – Higher)	Band	Spectral Wavelength (nm)
OH*	${}^2\Sigma-{}^2\Pi$	(2-0)	260.9
		(1-0)	281.1
		(0-0)	306.4
		(0-1)	342.8
CH*	${}^2\Delta-{}^2\Pi$	(0-0)	431.5
		(0-1)	494.1
	${}^2\Sigma-{}^2\Pi$	(1-0)	362.8
		(0-0)	387.2
C ₂ *	${}^3\Pi-{}^3\Pi$	(2-0)	438.3
		(1-0)	473.7
		(0-0)	516.5
		(0-1)	563.6
		(0-2)	619.1
CN*	${}^2\Sigma-{}^2\Sigma$	(1-0)	359.0
		(0-0)	388.3
		(0-1)	421.6

Table 1.1 (Continue)

NH*	$^3\Pi-^3\Sigma$	(1-0) R Branch	302.3
		(1-0) Q Branch	305.1
		(0-0)	336.0
		(0-1) Q Branch	375.2
		(0-1) P Branch	380.4
HCO*		A ₀ Progression	329.8
		A ₁ Progression	337.6
		A ₂ Progression	353.9
H ₂ O*		Band Heads	616.6, 645.8, 691.9, 716.5, 809.7, 891.6, 927.7, 966.9
CO ₂ *		Continuum emission	340–650

Multivariate Data Analysis

Multivariate data analysis is defined as a data analysis technique where several variables are simultaneously observed and analyzed to establish a quantitative relationship between variables and one or more properties of interest [22]. For instance, Figure 1.5 shows NIR absorption spectra collected from bio-oil samples with different water concentrations. Bio-oil consists of ~300-400 chemical compounds. The increase in water concentration increases the inhomogeneity in the species distribution in the sample. Hence, in order to establish a quantitative relationship between NIR absorption and bio-oil concentration, simultaneous observation and analysis of the entire spectral

range (X-variable) should be performed. The objective of the multivariate analysis is to decompose the spectral data in to two parts: the data structure part that shows variations in the property of interest and the noise part that shows random variations with change in the property of interest.

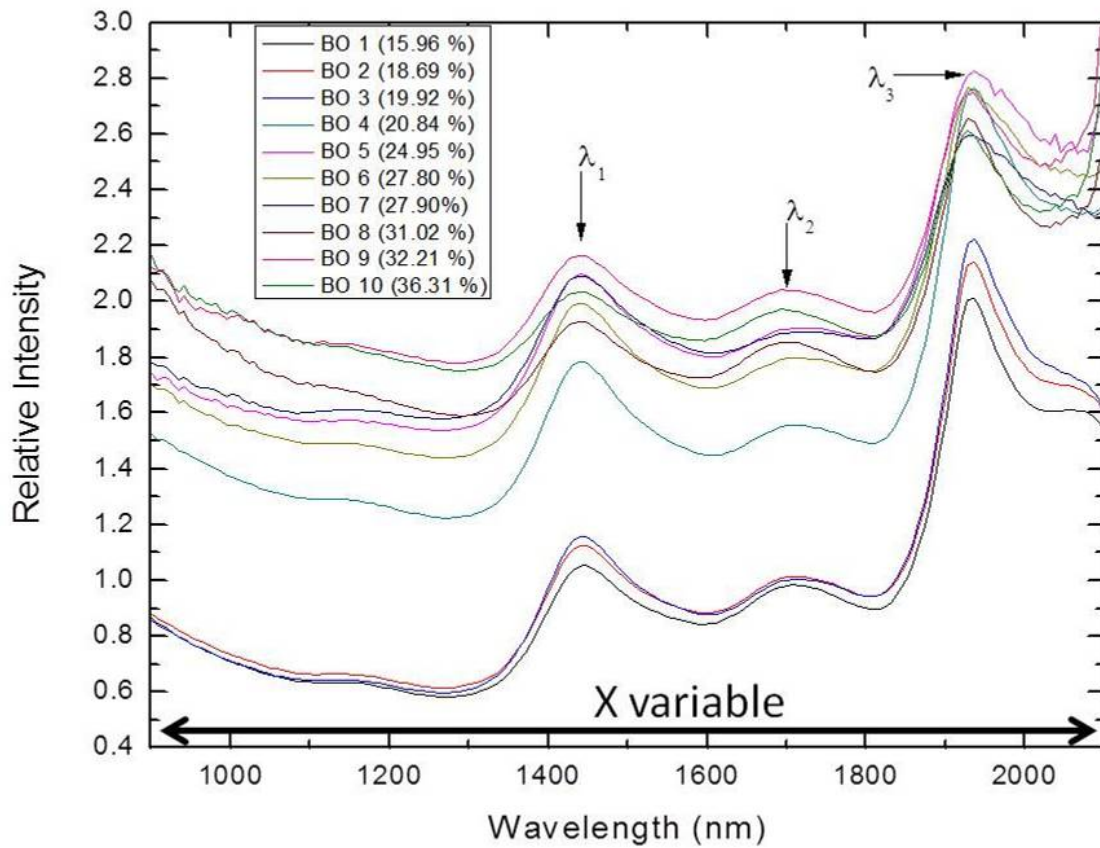


Figure 1.5

X variables in NIR absorption spectra collected from different bio-oil samples

In Chapters 2, 5, and 6 multivariate data analysis has been employed to analyze spectral data. A detailed description of the problems in context to the specific application is provided in the respective chapters. In particular, principal component regression and

partial least-square regression were employed in Chapter 2. Partial least-square regression was also employed in Chapter 5 and Chapter 6. In the following sections, a brief description of each technique is provided. Finally, multiplicative scattering correction (a data preprocessing technique), which was employed in Chapter 2, is also discussed.

Principal Component Regression

Principal component regression is a multivariate regression analysis, in which initially a mathematical transformation is performed on the spectral data to obtain a set of orthogonal latent vectors (also known as principal components) that show maximum variation in the spectral data. Once the principal components are obtained, the spectral data are linearly regressed with respect to the analytical data (in the direction of principal components) to develop a calibration model. Figure 1.6 shows an illustration of principal components (PC1 and PC2) in three-dimensional data. A pictorial representation of principal component regression is given in Figure 1.7.

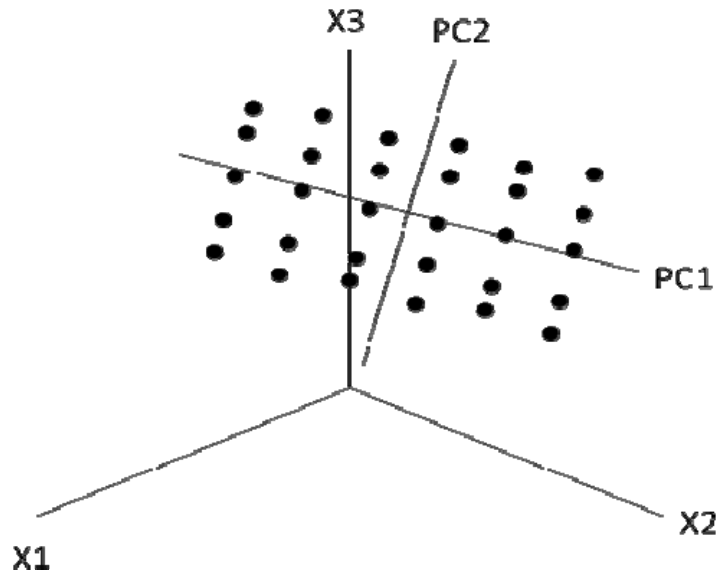


Figure 1.6

Principal components for three-dimensional data

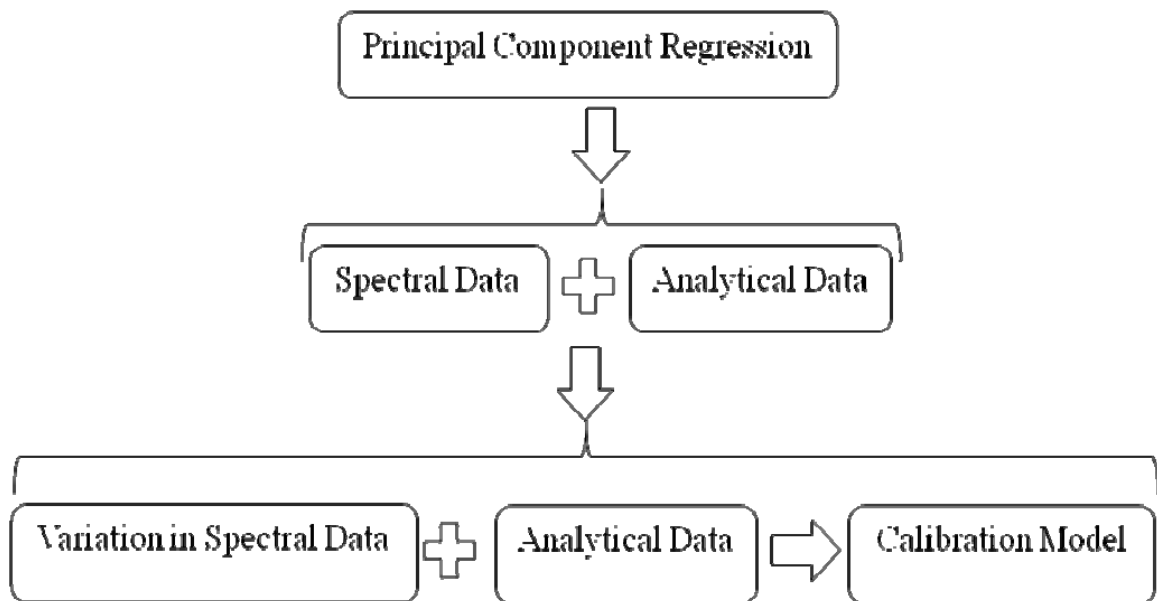


Figure 1.7

Pictorial representation of principal component regression

Partial Least Squares Regression

In partial least squares regression, the principal components are defined as the directions of maximum variation in spectral data as well as analytical data. This is obtained by projecting the spectral data and the analytical data into a new space. Once, new principal components are obtained, linear regression is performed in a manner that is very similar to principal component regression to develop a calibration model. Figure 1.7 is a pictorial illustration of the partial least squares regression.

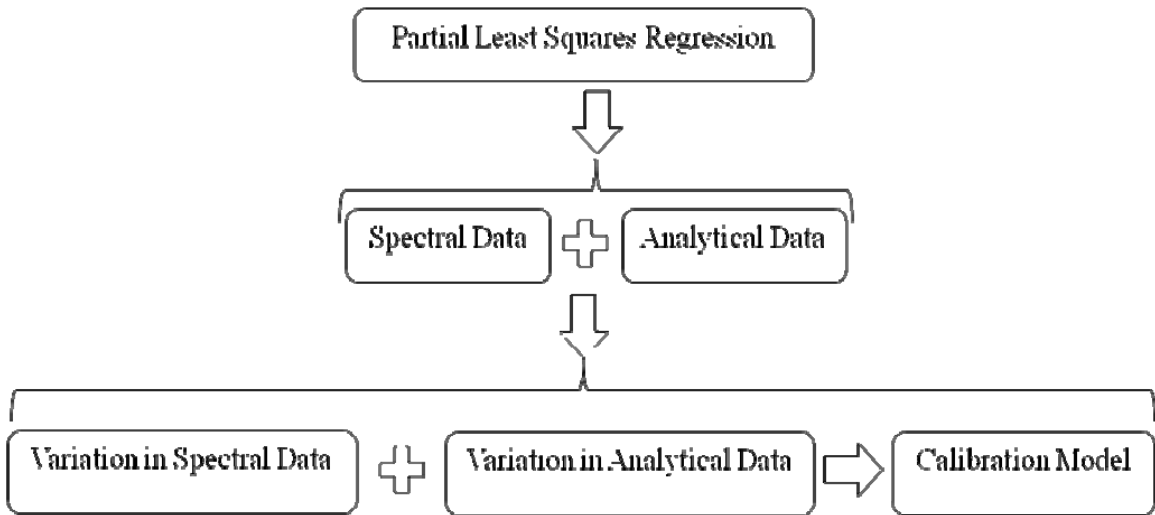


Figure 1.8

Pictorial representation of partial least squares regression

Multiplicative Scattering Correction

In some instances, the absorption spectra obtained from a sample may include contributions from the scattering of the incident light as well. Particularly in NIR absorption spectra from bio-samples; this phenomenon is fairly common. To reduce the contribution of light scattering in the absorption spectra, a data preprocessing technique is

employed to improve the calibration (especially for multivariate calibration). The formulation of the multiplicative scattering correction (MSC) involves the following assumptions:

- The scattered Light's wavelength dependence is different from that of chemical-based absorption.
- Using data at various wavelengths, the difference between absorption and light scattering can be established.
- Scattering for each sample is calculated relative to an "ideal" sample; and each sample's spectrum is corrected so that it has the same scattering level as the "ideal."

In order to perform MSC, an ideal spectrum (X_{ideal}) is obtained by taking the average of the entire spectra in the calibration set. Now for each spectrum X , a relationship with X_{ideal} is obtained as:

$$X = a + bX_{ideal} + e \quad (1.4)$$

where a and b are obtained by least-squares regression between X and X_{ideal} over the entire wavelength range in the spectrum.

Now, the corrected spectrum, X_{MSC} will be given by,

$$X_{MSC}(i) = \frac{X(i) - a}{b} \quad (1.5)$$

where, " i " represents various wavelengths in the spectral range.

Research Motivation and Specific Objectives

The continuing need for greater energy security and energy independence has motivated researchers to develop new energy technologies for better energy resource

management and efficient energy usage. The focus of this dissertation was the development of optical (spectroscopic) sensing methodologies for various fuels, energy-related devices, and applications. The specific objectives of the current work are as follows:

1. To develop a sensing methodology to measure the water content in raw bio-oil produced from the fast pyrolysis of biomass.
2. To study the effect of ultraviolet exposure on the chemical stability of bio-oil.
3. To design and develop a prototype sensor for multi-elemental impurity monitoring in hydrogen fuel.
4. To develop a chemiluminescence-based spectroscopic diagnostic to measure equivalence ratios in methane-air premixed flames that can be translated to practical combustion system in the future.
5. To develop a LIBS-based spectroscopic diagnostics to measure the equivalence ratios in methane-air premixed flames and compare its performance with chemiluminescence-based diagnostics technique.

To achieve these objectives, several optical sensing methodologies were employed. Water shows strong absorption in the near-infrared region. Hence, a near-infrared absorption-based vibrational spectroscopy was employed for the measurement of the water content of bio-oil. Laser-induced fluorescence (LIF) spectroscopy is a molecular spectroscopic technique that is based on radiative emission after electronic excitation (via absorption of laser light). This was used to study the effect of ultraviolet exposure on the chemical stability of bio-oil. Multi-elemental analysis can be easily performed in laser-induced plasma utilizing laser-induced breakdown spectroscopy

(LIBS). This methodology was used in the development of an optical sensor for multi-species impurity monitoring in hydrogen fuel. Variation of spectral peak intensities associated with various chemical species (i.e., OH^* , CH^* , C_2^* , and CO_2^*) in flame chemiluminescence emission depends on the fuel-air equivalence ratio of the burning mixture. Hence, chemiluminescence-based multivariate sensing was employed to monitor the equivalence ratios in methane-air premixed flames. The LIBS can provide elemental information from a very small control volume by tightly focusing the laser to a spot size of micron order. Hence, LIBS was employed to measure local equivalence ratios in methane-air premixed flames.

Organization of the Dissertation

This dissertation deals with the development of different optical sensing methodologies for the various objectives discussed in the last section. Each subsequent chapter (except Chapter 4 and Chapter 6 that is under peer-review process to appear in *Sensors and Actuators B: Chemical* and *Fuel* journals, respectively) is a peer-reviewed published journal article, and therefore, is structured as a self-contained entity. Chapter 2, which was published in *Sensors and Actuators B: Chemical*, is on the application of near-infrared (NIR) spectroscopy for predicting water content in bio-oil. A reflection-absorption-based fiber optic NIR system was designed to overcome sampling limitations due to the dark color and viscous nature of bio-oil. The results suggest that a calibration model based on NIR spectroscopy in association with multivariate data analysis can be developed to predict water content in bio-oil. The effect of ultraviolet (UV) exposure on the chemical stability of bio-oil is studied in Chapter 3. A 325-nm He-Cd laser was

employed as an excitation source and laser-induced fluorescence in the backwards direction was monitored to study the chemical instability. It was concluded that the phenolic compounds present in bio-oil show chemical instability when exposed to UV light, and therefore, the quality of bio-oil may degrade after prolonged exposure to UV light. This work was published in the *Energy and Fuels* journal. Chapter 4 focuses on the development of a prototype optical sensor for multi-species impurity monitoring in hydrogen fuel. This sensor employs laser-induced breakdown spectroscopy as its sensing methodology. A prototype optical sensor was designed, developed, and tested for simultaneously monitoring four trace level elemental impurities (i.e., nitrogen, oxygen, argon, and helium) in hydrogen. Chapter 5 describes the chemiluminescence-based multivariate sensing of the local fuel-air equivalence ratios in premixed atmospheric methane-air flames which was published in the *Fuel* journal. Traditionally, the intensity ratios of OH^* , CH^* , and C_2^* (i.e., OH^*/CH^* , C_2^*/CH^* , C_2^*/OH^*) have been correlated with the equivalence ratios in premixed flames. In this study, it is shown that a multivariate calibration (that simultaneously uses the OH^* , CH^* , and C_2^* chemiluminescence information along with continuum emission from CO_2^*) will provide a more robust calibration with better equivalence ratio prediction capabilities compared to intensity ratio calibration. A simple, robust, and cost effective LIBS based diagnostic technique (employing ungated signal detection) for local equivalence ratio measurement in premixed methane-air flames is presented in Chapter 6. In the chapter, the prediction capabilities of LIBS based calibration model is compared with previously developed chemiluminescence based calibration model. It is concluded that LIBS based calibration model provides better prediction results when compared with chemiluminescence - based

prediction results. Finally, Chapter 7 contains the summary of the research work conducted in this dissertation and future recommendations for the prospective researchers.

References

- [1] G. Gauglitz, and T. V. Dinh, Handbook of Spectroscopy, WILEY-VCH Verlag GmbH & Co. KGaA, Weinheim, Germany (2003).
- [2] W. S. Lyon, Analytical Spectroscopy in Energy Technology: 26th: Conference Proceedings (Analytical Chemistry Symposia Series), Elsevier Science Ltd (1984).
- [3] M. Commodo, O. Wong, I. Fabris, Clinton P. T. Groth, and Omer L. Gulder, Spectroscopic Study of Aviation Jet Fuel Thermal Oxidative Stability, Energy & Fuels 2010 24 (12), 6437-6441.
- [4] J. A. Cramer, R. E. Morris, B. Giordano, and S. L. Rose-Pehrsson, Partial Least-Squares Predictions of Nonpetroleum-Derived Fuel Content and Resultant Properties When Blended with Petroleum-Derived Fuels, Energy & Fuels 2009, 23(2), 894-902.
- [5] H. S. P. Carneiro, A. R. B. Medeiros, F. C. C. Oliveira, G. H. M. Aguiar, J. C. Rubim, and P. A. Z. Suarez, Determination of Ethanol Fuel Adulteration by Methanol Using Partial Least-Squares Models Based on Fourier Transform Techniques, Energy & Fuels 2008, 22(4), 2767-2770.
- [6] P. E. Flecher, W. T. Welch, S. Albin, and J. B. Cooper, Determination of octane numbers and Reid vapor pressure in commercial gasoline using dispersive fiber-optic Raman spectroscopy, Spectrochimica Acta Part A: Molecular and Biomolecular Spectroscopy 1997, 53 (2), 199-206.
- [7] C. N. C. Corgozinho, M. M. O. Carvalho, and P. J. S. Barbeira, Spectrophotometric and Chemometric Determination of the ASTM Color of Automotive Diesel, Energy & Fuels 2009, 23(4), 2136-2142.
- [8] M. L. Parsons, B. W. Smith, and G. E. Bentley, Handbook of Flame Spectroscopy, Plenum Press, New York, USA (1975).
- [9] S. Cheskis, I. Derzy, V.A. Lozovsky, A. Kachanov, and D. Romanini, Cavity ring-down spectroscopy of OH radicals in low pressure flame, Applied Physics B: Lasers and Optics 1998, 66 (3), 377-381.
- [10] V. N. Nori, and J. M. Seitzman, CH* chemiluminescence modeling for combustion diagnostics, Proceedings of the Combustion Institute 2009, 32 (1), 895-903.
- [11] P. Stavropoulos, A. Michalakou, G. Skevis, and S. Couris, Laser-induced breakdown spectroscopy as an analytical tool for equivalence ratio measurement in methane-air premixed flames, Spectrochimica Acta Part B: Atomic Spectroscopy 2005, 60 (7-8), 1092-1097.

- [12] M.R. Schrewe, and J.B. Gandhi, Near-wall formaldehyde planar laser-induced fluorescence measurements during HCCI combustion, Proceedings of the Combustion Institute 2007, 31 (2), 2871-2878.
- [13] H. W. Siesler, Y. Ozaki, S. Kawata, and H. M. Heise, Near-Infrared Spectroscopy: Principles, Instruments, Applications, WILEY-VCH Verlag GmbH, Weinheim, Germany (2002).
- [14] J. R. Lakowicz, Principles of Fluorescence Spectroscopy, Springer Science+Business Media, LLC, New York, USA (2006).
- [15] J.P. Singh, and S.N. Thakur, Laser-Induced Breakdown Spectroscopy, Elsevier Science B. V., Amsterdam, The Netherlands (2007).
- [16] A. G. Gaydon, The Spectroscopy of Flames, John Wiley & Sons Inc., New York, USA (1957).
- [17] S. A. Ciatti, B. Bihari, and T. Wallner, Establishing combustion temperature in a hydrogen-fuelled engine using spectroscopic measurements, Proceedings of the Institution of Mechanical Engineers, Part D: Journal of Automobile Engineering 2007, 221(6), 699-712
- [18] J. S. Kim, and M. A. Cappelli, Temperature measurements in low-pressure, diamond-forming, premixed flames, Journal of Applied Physics 1998, 84(8), 4595-4603.
- [19] H. P. Broida, Effects of Self-Absorption on Rotational "Temperatures" of OH in Flames, The Journal of Chemical Physics 1953, 21(7), 1165-1169.
- [20] Y. Hardalupas, M. Orain, C. S. Panoutsos, A.M.K.P. Taylor, J. Olofsson, H. Seyfried, M. Richter, J. Hult, M. Aldén, F. Hermann, J. Klingmann, Chemiluminescence sensor for local equivalence ratio of reacting mixtures of fuel and air (FLAMESEEK), Applied Thermal Engineering 2004, 24(11–12), 1619-1632
- [21] R.W.B. Pearse, A.G. Gaydon, The Identification of Molecular Spectra, 4th Edition,, John Wiley & Sons Inc., New York, USA (1976).
- [22] K. H. Esbensen, Multivariate Data Analysis – In Practice, 5th Edition, Camo Inc. (2004).

CHAPTER II
REFLECTION–ABSORPTION-BASED NEAR INFRARED SPECTROSCOPY FOR
PREDICTING WATER CONTENT IN BIO-OIL *

Abstract

A novel fiber-optic NIR system based on reflection–absorption phenomenon for predicting water content in bio-oil was developed. The system successfully overcomes the sampling limitations posed by the dark and sticky nature of bio-oil. Spectral information in the near-infrared (NIR) region (900–2100 nm) was obtained for bio-oils with varied levels of water content. The feasibility of designing an NIR system for estimating the water content in bio-oil was tested by applying multivariate analysis to the spectral data. Two important techniques of multivariate data analysis, principal component regression (PCR) and partial least squares (PLS), were independently applied to experimental results to construct theoretical models. The calibration results demonstrated that spectral information can successfully predict the bio-oil water content (from 16% to 36%) with less than 1% of error and with a high coefficient of

* Note: Most of the content of this chapter has been adapted from Sensors and Actuators B: Chemical, Volume 136, Issue 1, Markandey M. Tripathi, El Barbary M. Hassan, Fang-Yu Yueh, Jagdish P. Singh, Philip H. Steele, and Leonard L. Ingram Jr., [Reflection–absorption-based near infrared spectroscopy for predicting water content in bio-oil](#), Pages 20-25, Copyright (2008), with permission from Elsevier.

determination ($R^2 = 0.98$). The reliability of a fiber-optic NIR system for predicting the bio-oil water content indicates that there is potential for utilization of NIR spectroscopy in monitoring bio-oil quality during production.

Introduction

Near-infrared (NIR) spectroscopy is widely acknowledged as a powerful diagnostic tool for characterizing various chemical species. Some of the features of the NIR technique, giving it an edge over other optical methods, include simplicity, high detection sensitivity, and versatility in probing a broad range of chemicals. Apart from these qualities, NIR spectroscopy is nondestructive and can provide real-time information about various bio-chemical processes under study. When interfaced with multivariate data analysis, NIR spectroscopy provides both qualitative and quantitative measurements. In recent years, application of NIR spectroscopy has been reported in food [1], medical [2], environmental [3], wood science [4], biological [5], and petrochemical industries [6] amongst others.

Conventional sources of energy including coal and petroleum are limited and bound to be depleted in due course of time. Apart from the sustainability issue, usage of such types of conventional energy sources release toxic species, e.g. carbon monoxide which is detrimental to the concept of healthy and clean environment. Therefore, emphasis is on exploring alternative sources of energy such as bio-oils [7]. Biomass is the most abundant renewable source of feed stock for production of energy and chemicals. All biomass can be converted to various forms of energy through several thermo-chemical conversion processes [8]. One of the promising conversion processes

for liquid fuel production is the fast pyrolysis technique. This involves the rapid heating of biomass at a high temperature (450–600 °C) in the absence of oxygen to produce organic vapors, pyrolysis gases and char. The vapor is then rapidly cooled and condensed to a liquid product termed pyrolysis oil or bio-oil [9, 10]. The non-condensable gases and the solid char produced during fast pyrolysis are valuable byproducts which are available as energy sources.

Bio-oil typically consists of a complex mixture of organic compounds and water. The ratio of these compounds varies depending upon the feed stock, pyrolysis process, and variables applied. Bio-oil has a number of potential uses, including: fuel for electricity generation; transportation fuels; a source of value-added chemical compounds, adhesives and wood preservation chemicals [10]. To date, most attention has been focused on bio-oil as a potential liquid fuel. However, bio-oil utilization for liquid fuel applications has been limited by the combined effects of high oxygen (up to 45%) and water contents (20–30%). The combined result of the presence of highly oxygenated compounds and significant water content is a reduced energy content that is equivalent to about one-half of that of no. 2 fuel oil [11]. Many researchers are engaged in developing technology to upgrade bio-oil quality for use as a liquid fuel. These upgrading techniques often require reduction of the bio-oil water content. Determination of bio-oil water content is relatively time consuming. No method is available to make this determination in real time during bio-oil production. A rapid water content determination in real time by on-line procedures would benefit the development of bio-oil upgrading technologies.

Infrared spectroscopy has been shown to effectively monitor biodiesel water content [12]. The combination and overtone absorption band of the O–H bond in water, which is very strong in the NIR region [13], makes NIR spectroscopy an ideal candidate for quantifying water content in applications of this type.

In the present work, a new simple reflection–absorption-based NIR system has been developed for predicting water content of bio-oil. The dark brown color of bio-oil poses serious limitations on employing conventional methods for studying the NIR-based absorption signal. This study aimed to overcome these limitations by developing novel methods to capture NIR absorption spectra from dark and viscous bio-oils.

Experimental

Pre-Design NIR Experiments

Prior to designing a fiber-optic NIR system, preliminary tests were performed to determine a spectral sampling method effective for NIR bio-oil analysis. The dark brown color and sticky nature of bio-oil severely restricted the transmittance of NIR radiation through the sample. This posed a limitation on application of conventional transmission and reflection spectroscopy methods. The optical probe used by Felizardo *et al.* [12] based on diffuse transflection phenomenon, worked well on translucent and non-sticky biodiesel. This probe was not used in the present work because it is highly sensitive to a non-clean external surface. Initially, the diffuse reflection technique was tested involving use of a glass slide with a glued metallic center ring. The metallic ring held the sample and a reflection probe was directed toward the slide bottom. This approach resulted in a

weak NIR signal. Inconsistency in replicated spectral data was also high due to varying optical path length in the diffuse signal. To overcome these problems, two metallic strips were incorporated diagonally opposite to the central ring. The thickness of the metallic ring and strips were optimized. A second glass slide was placed on the top, and parallel to the first to obtain the optical reflection. This modified configuration ensured an identical optical path length for successive bio-oil sample measurements. It also enhanced the NIR absorption signal by reducing the diffuse transmittance from bio-oil. Comparative spectra from both setups are shown Figure 2.1.

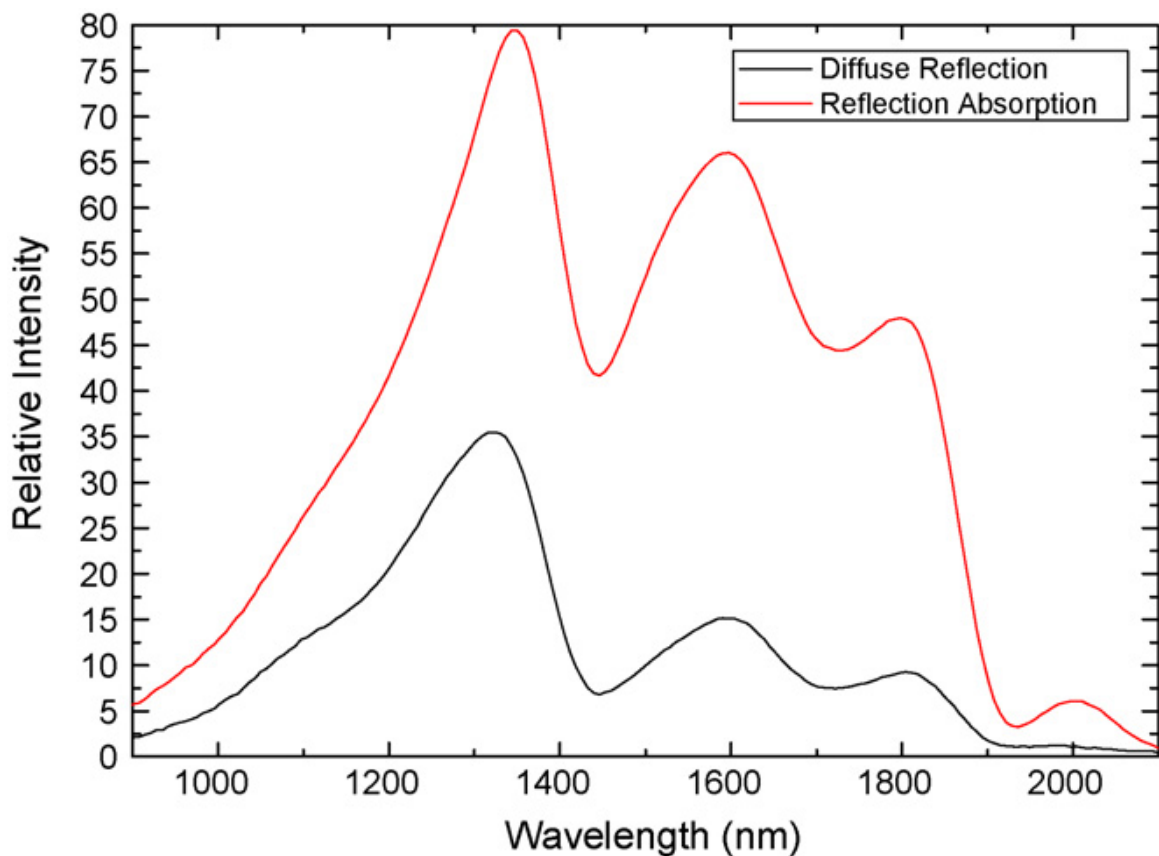


Figure 2.1

Comparison of NIR intensity spectra of bio-oil from diffuse reflection and reflection absorption setups

Fiber Optic System Configuration

A schematic diagram of the configured fiber optic NIR system is shown in Figure 2.2. For NIR absorption, the system employed a halogen lamp (Mikropack, HL-2000-HP) as the excitation light source. A reflection/back-scattering Y-shaped probe (Ocean Optics, R600-7-VIS/125F) guided the excitation beam to the sample and collected the reflected signal. The probe consisted of seven optical fibers, each of $600 \pm 10 \mu\text{m}$ core diameter and of 0.22 ± 0.02 numerical aperture with 6 illumination fibers around one read (signal collection) fiber. The use of multiple illumination fibers provided a better absorption signal.

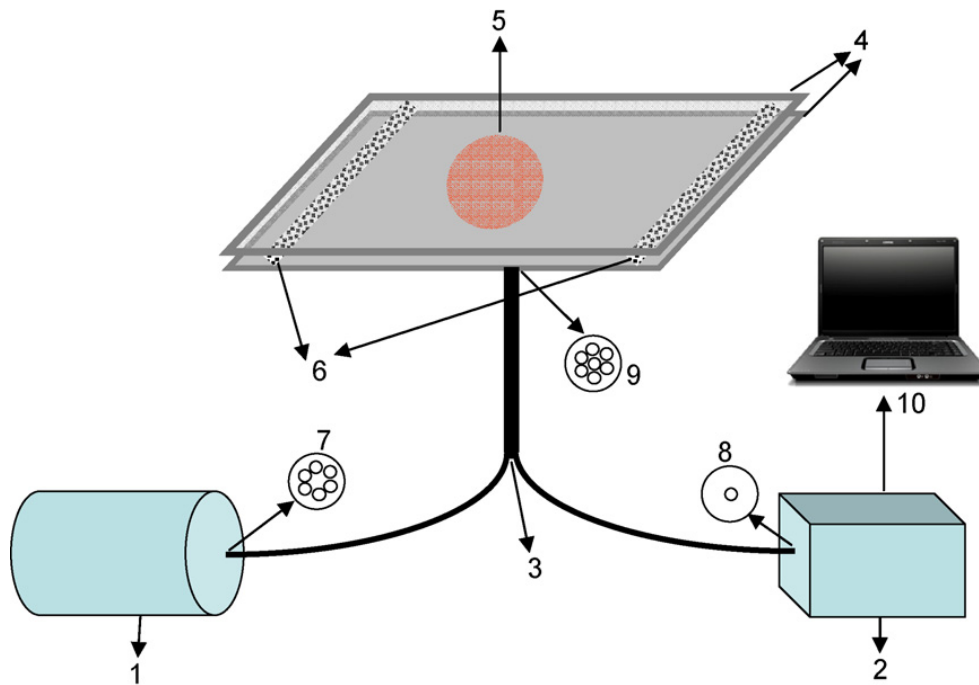


Figure 2.2

Schematic of fiber optic (near infrared) NIR system. Its components are (1) NIR broadband source, (2) NIR detector, (3) Y-shaped optical fiber reflection probe, (4) glass slides, (5) metallic ring, (6) metallic strips, (7) illumination fibers, (8) read fiber, (9) probe end, and (10) note book computer

As previously described, the reflection absorption apparatus consisted of two glass slides held parallel to each other. The bottom glass slide had one metallic ring at the center surrounded by two metallic strips. The thickness of ring and metallic strips were optimized at 0.75 mm. A portion of the NIR radiation was transmitted by the bottom glass slide through the sample. The beam reflected from the top glass slide was collected by the read fiber. The excitation beam passed through the sample twice, which increased the interaction length of the beam with the sample, thereby enriching the spectral information associated with the collected signal. The read fiber transmitted the signal to a 265-element InGaAs linear-array NIR detector (Ocean Optics, NIR 256-2.1).

The NIR detector was interfaced with a notebook computer via a USB port. Ocean Optics data acquisition software collected the NIR reflection–absorption spectrum. Each spectrum was collected over an integration time of 1 ms, and averaged over 1000 spectra. The software further smoothed the collected spectra by averaging five consecutive data points in the entire spectral range.

Bio-Oil Preparation

The study bio-oil was produced from clear pine lumber feedstock chipped to a particle size of 1–2 mm. The pyrolysis reactor was a stainless steel auger reactor with a ~1 kg/h feed rate and an auger speed of 13 rpm. Auger pyrolysis temperature was 450 °C. The condensed bio-oil was collected directly in air-tight bottles and refrigerated immediately at 4 °C to prevent aging.

Bio-Oil Characterization

The bio-oils were characterized physically and chemically. Water content was determined by ASTM Method D-1744. Viscosity was measured using Stony Brook viscometer (PDVa-100). Acid values were obtained by dissolving 1 g of bio-oil in an iso-propanol/water mixture and titrating to pH 8.5 with 0.1 N NaOH. The pH was determined indirectly by adding 1 g of bio-oil to 50 ml of water, stirring, and measuring with a pH meter (Orion Inc., EA920). Bio-oil density was ascertained at a temperature of 20 °C. The percent filterable solids were determined by dissolving 5 g of bio-oil in 100 ml of methanol and filtering through a 25µm glass filter. The filter was dried at 105 °C before and after collection of the particulate material. The increase in weight after

filtration allowed calculation of the percent solids. Average molecular weight was measured by a Waters HPLC system, consisting of a Waters 600E System Controller and a Waters 410 Differential Refractometer. The physical and chemical characterizations of the bio-oils are presented in Table 2.1.

Table 2.1

Physical properties and molecular weight of raw pine lumber (bio-) oil

Characteristics	Value
Water concentration (wt %)	15.96
Acid value	80.56
Density (g/cc)	1.19
Viscosity at 50 °C (cST)	29.95
pH	3.2
Average molecular weight (g/mole)	410

Testing Samples

To test the reliability of the system, samples were prepared by the method used by Blanco *et al.* [14]. Raw bio-oil (produced from the above-described method) with known, relatively low moisture content was used for this research investigation. The bio-oil was then separated further into nine more specimens of equal volume and measured amounts of distilled water were added to each specimen to develop a total of ten specimens with water contents ascending in value from the initial known bio-oil water content. The measured water content values (with Karl Fisher titration) for the ten bio-oil specimens prepared are in Table 2.2.

Table 2.2

Water content (%) in testing samples measured with Karl Fisher titration

Bio-oil No.	Water content %
BO 1	15.96
BO 2	18.69
BO 3	19.92
BO 4	20.84
BO 5	24.95
BO 6	27.80
BO 7	27.90
BO 8	31.02
BO 9	32.21
BO 10	36.31

Multivariate Data Analysis

The feasibility of employing NIR spectral data for the development of a calibration model was investigated by performing multivariate data analysis [15]. Unscrambler® version 9.7 (CAMO, Corvallis, OR, USA) performed the multivariate data analysis. Principal component regression (PCR) and partial least squares (PLS) models were constructed from the spectral and analytical data. Multivariate regression is relevant for a two-dimensional (X, Y variable) data set, where the response Y-variable (analytical data) depends on more than one explanatory X-variable (spectral wavelength). During the formulation of calibration model, linear combinations of only those explanatory X-variables are considered that are related to the response Y-variable. In this study, bio-oil water content and NIR spectral data were the response and the explanatory variables, respectively. In PCR analysis, the explanatory X-variable is linearly regressed on principal components (PCs) to determine maximum variation without inclusion of the

information from the response Y-variable. However, PLS uses variation in the data from the response Y-variable and the explanatory X-variable. This provides new latent, or PCs for the regression which are more related to the variation in response Y-variable. Prior to PCR or PLS regression, NIR spectral data were normalized by means of multiplicative scattering correction (MSC) to correct the variability of baseline data due to the scattering phenomenon. The reliability of calibration models in terms of predicting power were tested with full cross-validation (FCV) and test set validation (TSV) along with uncertainty tests.

Results and Discussions

Water gives strong and complex absorption in infrared region due to vibrational overtones and combinations with librations. Particularly in the NIR region ($\lambda \sim 900\text{--}2000\text{ nm}$), these absorptions give broad spectral band, which makes it significant for rapid non-destructive water measurement [16]. Reflection-absorption NIR spectra of study bio-oils are shown in Figure 2.3. These spectra show three significant spectral peaks centered at $\lambda_1 \sim 1446\text{ nm}$, $\lambda_2 \sim 1707\text{ nm}$ and $\lambda_3 \sim 1935\text{ nm}$, respectively. Among these three peaks, λ_1 and λ_3 may have spectral contribution from NIR absorption in water [17]. λ_1 ($\sim 1446\text{ nm}$) may correspond to second overtone of symmetric stretch while λ_3 ($\sim 1935\text{ nm}$) to the combination of first overtones from symmetric stretch and bending in water molecule [18].

Figure 2.4 shows the variation in spectral peak intensity of NIR signal with an increase in the water concentration. The spectral peaks correspond to wavelengths at 1446.14 and 1935.45 nm, respectively. A lack of correlation between spectral intensity

and water concentration can be observed in Figure 2.4. This may be attributed to the fact that the homogeneity level of bio-oil samples decreases with an increase in the water concentration. As a result, bio-oil sample exhibits a pronounced increase in the multiplicative scattering, thereby affecting the reflection–absorption signal. This posed a serious limitation on the accurate measurement of NIR spectral peak intensity which was reflective of water content in the bio-oil samples. Therefore, to measure the actual contribution of water in estimating the NIR peak intensity and also to eliminate the effect of scattering, multivariate analysis was performed on the NIR spectra. Prior to performing multivariate analysis, multiplicative scattering correction (MSC) has been performed on NIR spectrum. MSC corrected NIR spectra are shown in Figure 2.5.

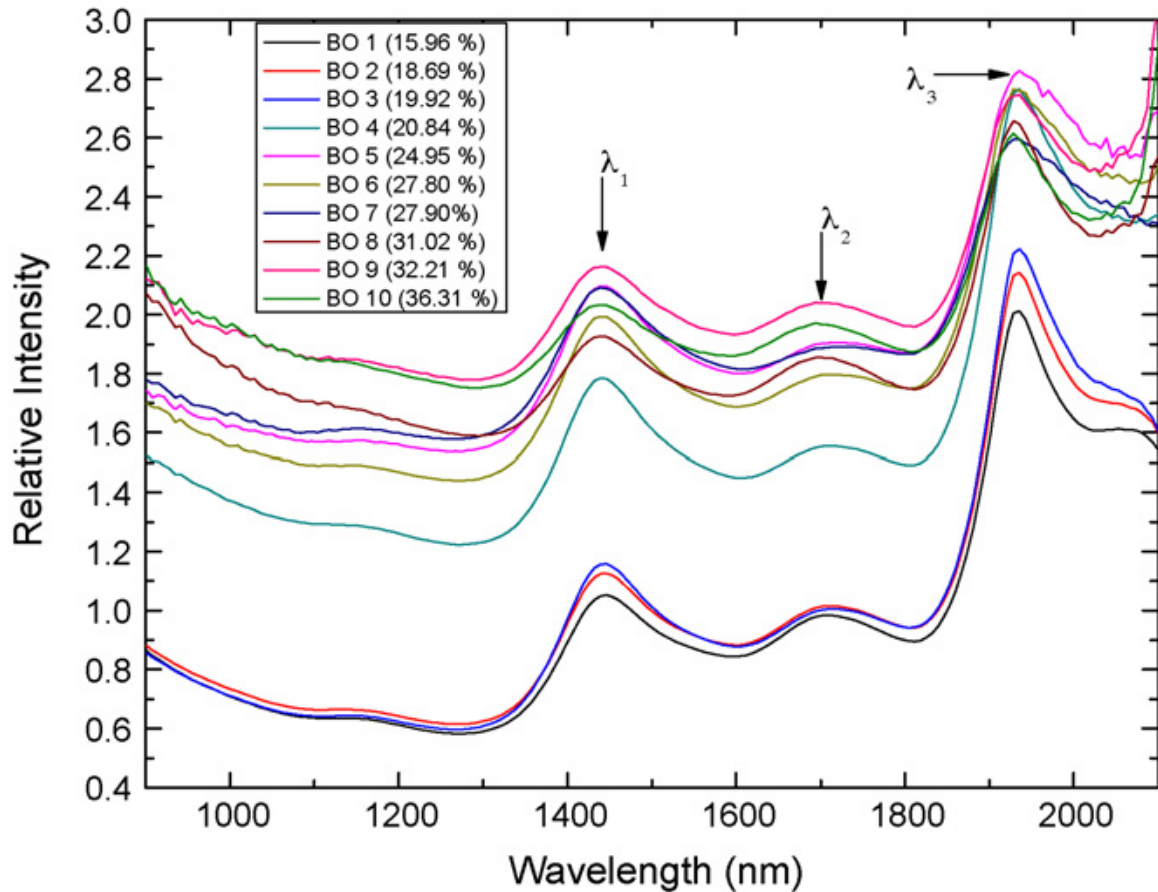


Figure 2.3

Plot of reflection-absorption NIR spectrum from bio-oil with different water content

Calibration model was developed with nine spectra from each bio-oil. These spectra were collected on three different days with three spectra at a time to measure the consistency in the spectral response of NIR system with time. Prior to the development of the calibration model, principal component analysis (PCA) was applied to the NIR spectral data. PCA cluster analysis assisted in differentiating outliers in replicated spectral data. Based on examination of the residual X-variance with leverage, two out of ninety spectra were considered to be outliers and were eliminated from the analysis.

While validating the model, leave-one-out method was chosen for full cross validation. In test set validation, thirty five random spectra were taken as a validation set by the software.

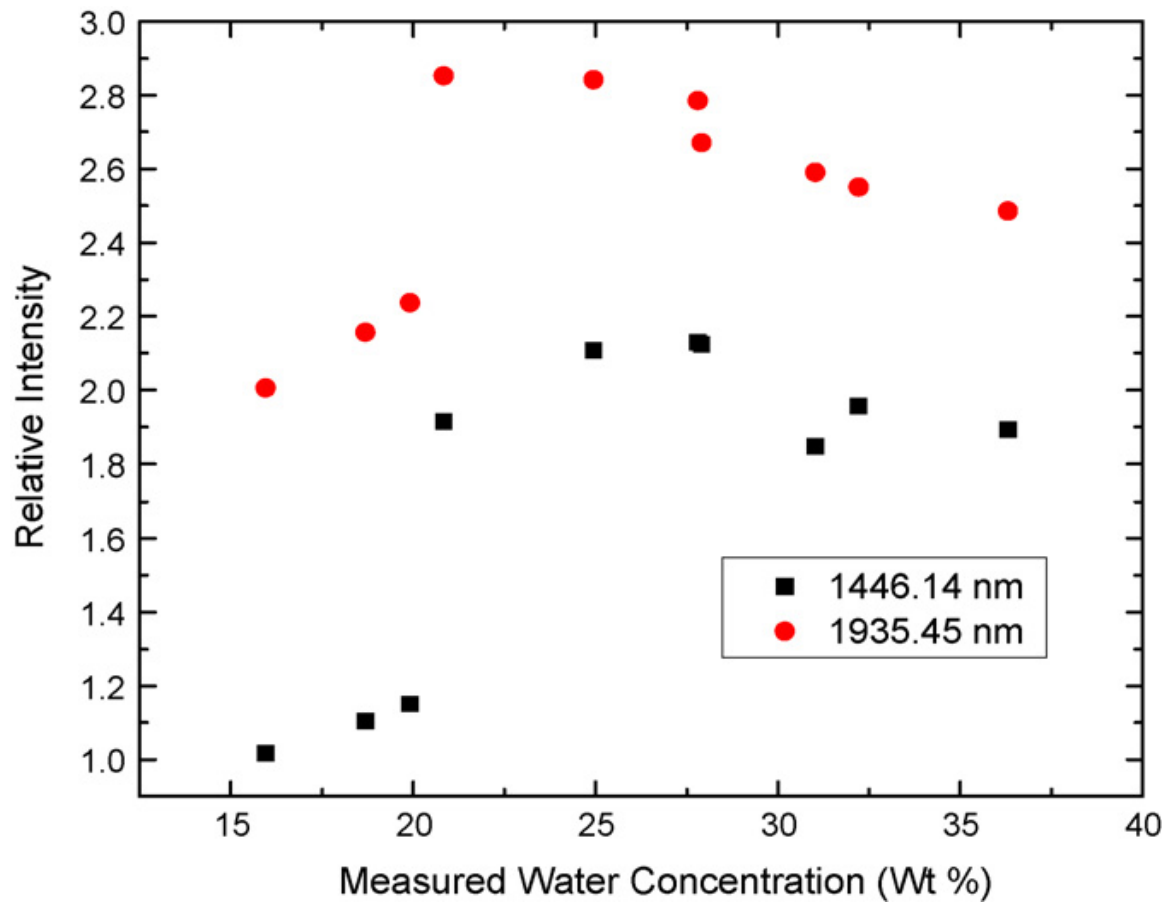


Figure 2.4

Variation of spectral peak intensity with water concentration at 1446.14 and 1935.45 nm spectral peaks

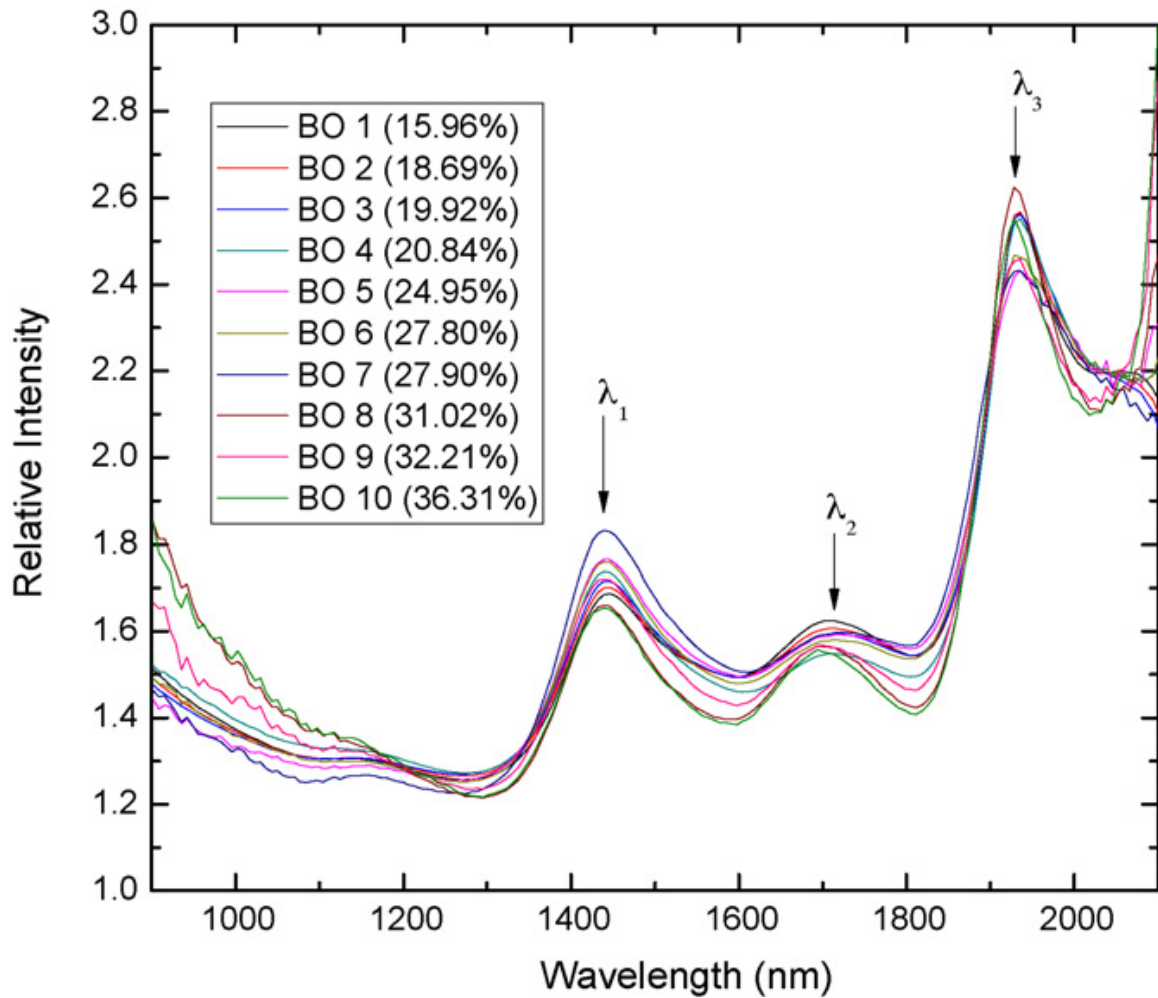


Figure 2.5

Plot of multiple scattering corrected (MSC) reflection-absorption NIR spectrum from bio-oil with different water concentrations

Principal Component Regression (PCR) Model

The results of PCR calibration model on reflection-absorption NIR spectra for predicting water content in bio-oils is given in Table 2.3. The coefficient of determination (R^2) increased from 0.84 for the unprocessed data to 0.92 for the MSC with test set validation. The MSC preprocessing also resulted in a low root mean square error of calibration (RMSEC). A similar reduction trend in root mean square error of

prediction (RMSEP) from 1.81 to 1.61 wt% with test set validation was also observed. However, the number of PCs increased from 2 to 8 for FCV and from 2 to 7 for TSV.

Table 2.3

PCR model results for prediction of water concentration in bio-oil with Full Cross Validation and Test Set Validation

	Full Cross Validation (FCV)					Test Set Validation (TSV)				
	PCs	R ² Cal.	RMSEC	R ² Val.	RMSEP	PCs	R ² Cal.	RMSEC	R ² Val.	RMSEP
900 nm – 2100 nm										
No Pre-processing	2	0.871	2.27	0.864	2.36	2	0.846	2.55	0.910	1.81
MSC	8	0.940	1.54	0.930	1.70	7	0.922	1.85	0.923	1.61
1300 nm – 2000 nm										
No Pre-processing	7	0.958	1.29	0.951	1.41	4	0.855	2.48	0.934	1.55
MSC	8	0.965	1.19	0.955	1.34	3	0.895	2.15	0.899	1.85

PCR calibration model was also developed for a reduced spectral range ($\lambda \sim 1300\text{--}2000$ nm) which included all significant peaks in the NIR spectra. These results (shown in Table 2.3) indicate that both RMSEC and RMSEP decreased for unprocessed data. On the contrary, MSC leads to high validation and prediction errors on application of TSV. In all cases (except for TSV on MSC), the R² improved. Based on Table 2.3 results, it was concluded that in the spectral range $\lambda \sim 900\text{--}2100$ nm, MSC data gives a better PCR calibration model than unprocessed data; however, in the range of $\lambda \sim 1300\text{--}2000$ nm unprocessed data is better correlated with bio-oil water content values.

Partial Least Squares (PLS) Model

Table 2.4 shows the result of PLS calibration model on NIR spectral data. In the spectral range of $\lambda \sim 900\text{--}2100$ nm, MSC pre-processing with FCV did not improve the results in terms of R^2 or RMSEC. However, with the TSV, MSC improved R^2 from 0.925 to 0.956 with low calibration error. Comparison of the calibration model on unprocessed data with FCV and MSC with TSV data gave similar results but MSC explained the spectral data variance with a lower number of PCs. In the $\lambda \sim 1300\text{--}2000$ nm spectral range MSC with TSV resulted in the highest R^2 and provided both low RMSEC and RMSEP. Hence, it can be concluded from Table 2.4 that with 6 PCs, MSC provided the best bio-oil water content prediction in the $\lambda \sim 1300\text{--}2000$ nm range.

Table 2.4

PLS model results for prediction of water concentration in bio-oil with Full Cross Validation and Test Set Validation

	Full Cross Validation (FCV)					Test Set Validation (TSV)				
	PCs	R ² Cal.	RMSEC	R ² Val.	RMSEP	PCs	R ² Cal.	RMSEC	R ² Val.	RMSEP
900 nm – 2100 nm										
No Pre-processing	6	0.956	1.33	0.940	1.56	4	0.925	1.82	0.949	1.31
MSC	5	0.947	1.46	0.933	1.67	5	0.956	1.40	0.932	1.52
1300 nm – 2000 nm										
No Pre-processing	6	0.969	1.11	0.957	1.30	5	0.961	1.31	0.953	1.26
MSC	6	0.971	1.08	0.963	1.23	6	0.978	0.99	0.963	1.12

Comparison of Tables 2.3 and 2.4 results indicate that the spectral range $\lambda \sim 1300\text{--}2000$ nm provided the highest variance for predicting bio-oil water content. Among both regression methods, PLS regression provided the better calibration model. This finding supports the fact that PLS regression is more efficient in extracting the information from an explanatory X -variable that is strongly correlated with a response Y -variable. For validation of the PLS model, it was concluded that the TSV gives the lowest RMSEP value, thereby ensuring the prediction performance of the calibration model and avoidance of over or under fitting. Figure 2.6 compares the reflection absorption NIR-predicted bio-oil water content values with measured Karl Fisher titration values. These predictions were based on the PLS calibration model within $\lambda \sim 1300\text{--}2000$ nm spectral range. Spectra were corrected for multiplicative scattering and the model was validated with TSV.

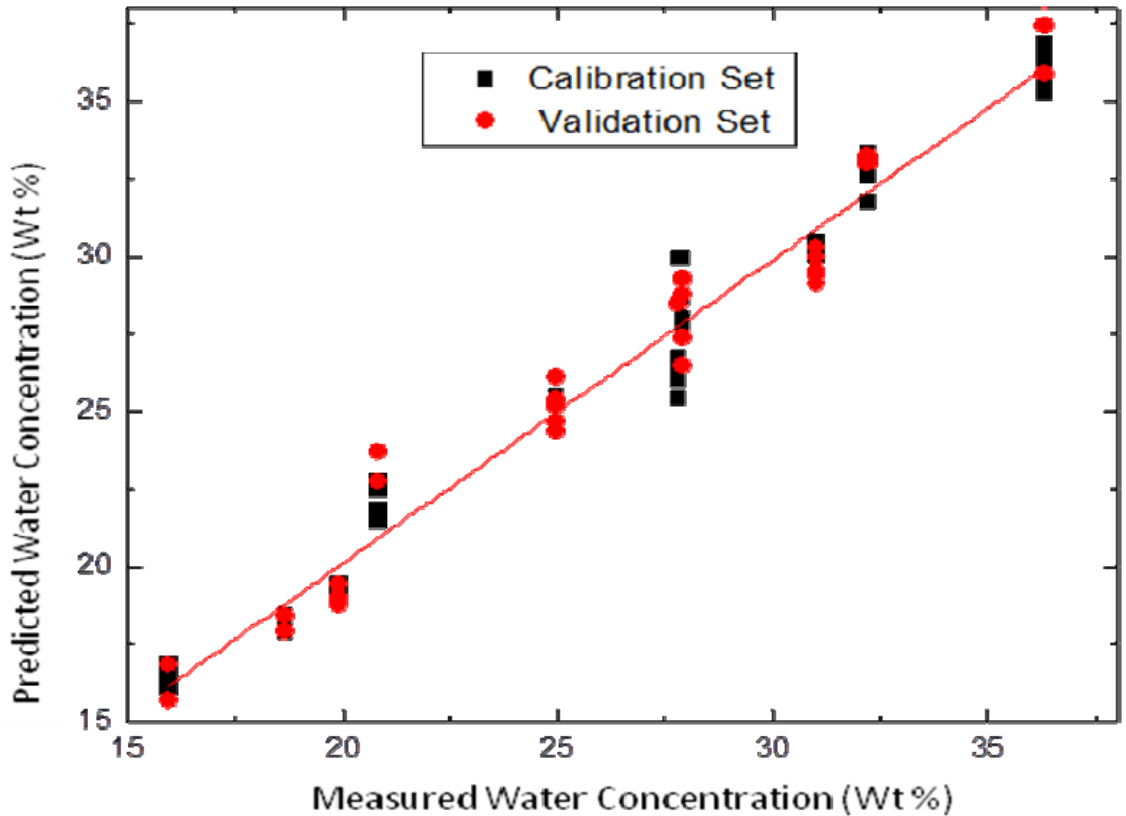


Figure 2.6.

PLS regression model for predicting water content in bio-oil in the 1300–2000 nm spectral range using multiple scattering correction (MSC) and test validation set

Conclusion

A reflection-absorption-based NIR system was developed and its functioning was demonstrated for estimating the water content of bio-oils. The developed system successfully overcomes the restraint involved in dealing with difficult liquid (i.e. dark, sticky, viscous), such as bio-oil. This system enhances the diffuse reflected light caused by bio-oil opacity by introducing a second parallel glass slide to provide a reduced optical path length. Two important techniques of multivariate data analysis – PCR and PLS –

were independently applied to the experimental data for constructing calibration models. The PLS-based model provided better estimates of water content than that given by PCR analysis. The future work will focus on developing a general calibration model for predicting water content in bio-oil. The formulation of such type of a comprehensive model would involve rigorous experiments to be carried on bio-oils procured from various feed stocks.

Acknowledgement

This effort was funded by Mississippi State University's Sustainable Energy Research Center (SERC) through Grant no. DE-FG36-06-G086025. Authors would like to thank Dr. David L. Monts for critical reading of manuscript and Dr. Vidhu S. Tiwari for his support in laboratory measurements.

References

- [1] A. Bello, F. Bianchi, M. Careri, M. Giannetto, G. Mori and M. Musci, *Anal. Chim. Acta* 603 (2007), pp. 8 -12.
- [2] A. Sakudo, Y. Suganuma, T. Kobayashi, T. Onodera and K. Ikuta, *Biochem. Biophys. Res. Commun.* 341 (2006), pp. 279 -284.
- [3] E. Dabakk, M. Nilsson, P. Geladi, S. Wold and I. Renberg, *Water Res.* 34 (2000), pp. 1666 -1672.
- [4] S. S. Kelly, T. G. Rials, R. Snell, L. H. Groom and A. Sluiter, *Wood Sci. Tech.* 38 (2004), pp. 257 - 276.
- [5] S. Kasemsumran, Y. P. Du, K. Murayama, M. Huehne and Y. Ozaki, *Anal. Chim. Acta*, 512 (2004), pp. 223 - 230.
- [6] A. R. Caneca, M. F. Pimentel, R. K. H. Galvão, C. Eliane da Matta, F. Rodrigues de Carvalho, I. M. Raimundo, Jr., C. Pasquini and J. J.R. Rohwedder, *Talanta* 70 (2006), pp. 344 - 352.
- [7] D. Mohan, C. U. Pittman, Jr. and P. H. Steele, *Energy and Fuels* 20 (2006), pp. 848 - 889.
- [8] J. Yanik, C. Kornmayer, M. Saglam and M. Yüksel, *Fuel Processing Technology* 88 (2007), pp. 942 - 947.
- [9] Adisak Pattiya, James O. Titiloye and Anthony V. Bridgwater. The 2nd Joint International Conference on “Sustainable Energy and Environment (SEE 2006)” Bangkok, Thailand, Nov. 21-23, 2006.
- [10] A.V. Brigwater, A.J. Toft, J.G. Brammer, *Renewable and Sustainable Energy Reviews* 6 (2002), pp. 181 - 246.
- [11] G.W. Huber, S. Iborra, A. Corma, *Chem. Rev.* 106 (2006), pp. 4044 - 4098.
- [12] P. Felizardo, P. Baptista, J. C. Menezes and M. J. N. Correia, *Anal. Chim. Acta*, 595 (2007), pp. 107 - 113.
- [13] D. Eisenberg and W. Kauzmann, *The Structure and Properties of Water*, Oxford University Press, London, 1969.
- [14] M. Blanco, J. Coello, H. Iturriaga, S. Maspoch and R. Gonzalez, *Mikrochim. Acta*, 128 (1998), pp. 235 - 239.
- [15] K. H. Esbensen, *Multivariate Data Analysis in Practice*, 5th edition, Camo Inc., 2004.

- [16] H. Büning-Pfaue, Food Chem. 82 (2003), pp. 107 - 115.
- [17] George Socrates, Infrared and Raman Characteristics Group Frequencies, Third Edition, John Wiley & Sons Ltd., 2004 p. 256.
- [18] B. Czarnik-Matusiewicz and S. Pilorz, Vib. Spectrosc., 40 (2006), pp. 235 - 245.

CHAPTER III
A STUDY OF THE EFFECT OF ULTRAVIOLET EXPOSURE ON BIO-OIL BY
LASER-INDUCED FLUORESCENCE SPECTROSCOPY*

Abstract

Laser-induced fluorescence (LIF) was used to simulate and monitor the effect of ultraviolet (UV) exposure on the chemical stability of bio-oil. Bio-oil obtained from fast pyrolysis of biomass has the potential for replacing fossil fuel in the future as liquid fuels. Pyrolysis-derived bio-oil contains up to 400 chemical compounds and tends to be very unstable, both physically and chemically. Bio-oil produced from four different sources (Pine Lumber, Pine Bark, Oak Bark, and Oak Wood) was used in this study. Synthetic bio-oil composed of ten chemicals but having similar weight percentage (wt%) of compound groups and having similar spectroscopic property as bio-oil, was prepared. Synthetic bio-oil simplifies the limitation in the study posed by complex chemical composition in bio-oil. It was concluded that phenols present in the bio-oil show chemical instability by giving time-dependent fluorescence intensity.

* Note: Most of the content of this chapter has been adapted from Energy & Fuels, Volume 24, Issue 11, Markandey M. Tripathi, El Barbary M. Hassan, Fang-Yu Yueh, Jagdish P. Singh, and Philip H. Steele, [Study of the Effect of Ultraviolet Exposure on Bio-oil by Laser-Induced Fluorescence Spectroscopy](#), Pages 6187–6192, Copyright (2010), with permission from American Chemical Society.

Introduction

The limited stock of fossil fuel and increased environmental awareness has produced a growing interest in new, renewable energy sources. Bio-oil obtained from fast pyrolysis of biomass is widely getting attention as a potential candidate for the future liquid fuels [1-3]. However, the pyrolysis-derived bio-oil tends to be very unstable, both physically and chemically. A typical pyrolysis-derived bio-oil can contain up to 400 chemical compounds [4]. It consists of several reactive organic chemical species, including alkenes, aldehydes, ketones, and carboxylic acids (up to 45%). These highly oxygenated compounds have a strong tendency toward condensation reactions, leading to the formation of complex molecules. These reactions can easily catalyze by various parameters while in the shipment and storage, which leads to the degradation in the quality of bio-oil for fuel application. Hence, an understanding of the physical and chemical aging mechanism is important for the quality improvement of bio-oil. Literature shows evidence of a comprehensive study on the effect of various parameters on physical and chemical stability of bio-oil. Czernik *et al.* have studied the effects of storage conditions on the physical and chemical properties of bio-oil [5]. The effect of temperature on bio-oil stability has been studied by Chaala *et al.* [6], and some recent bio-oil stability studies include [7-9].

Despite considerable study on the stability issue of bio-oil, no literature on the effects of solar radiation on bio-oil's chemical stability has been found by authors. During production, transportation, and storage, bio-oil can be exposed to the sun. The ultraviolet (UV) radiation coming from the sun typically contains 3.0eV to 5.0eV energy per photon. This radiation can easily stimulate photo-chemical conversion. Many groups

have studied the effect of UV on the chemical stability of various samples. For instance, Sheng *et al.* have shown the compositional changes in hydrotreated naphthenic oil under UV radiation [10]. D'Auria *et al.* have studied the effect of UV irradiation on crude oil [11]. Other recent studies on UV-induced aging include [12-14].

In the present work, the effect of UV exposure on the chemical stability of bio-oil was studied. The UV radiation coming to earth contains ~98% UV-A (315-400 nm); therefore, this part of the radiation was considered in this study. To simulate the condition, a laser in the UV region (325 nm) was employed for bio-oil excitation. Laser-induced fluorescence spectroscopy (LIFS) is a powerful technique for monitoring chemical changes [15]. Since, most of the bio molecules fluoresce on the absorption of ultraviolet radiation; therefore, LIFS was taken as a finger print of any chemical change catalyzed by UV radiation.

Experimental

Bio-Oil Sample Preparation

Four different bio-oils produced by pyrolysis of pine lumber, pine bark, oak wood, and oak bark were used in this study. Main characteristics of the used bio-mass feed stocks are summarized in Table 3.1. In Table 3.1, the oxygen content in the feed stocks was calculated by taking difference from the measurements of the other constituents during “Ultimate analysis (%)”. The pyrolysis was conducted using a stainless steel auger reactor. The auger reactor does not use any carrier gas or heat carrier. Hence, it can be operated continuously. The schematic of the Mississippi State

University small-scale auger reactor system is shown in Figure 3.1. A detailed method of bio-oil preparation is reported elsewhere [16]; however, a brief description is given as follows. The ground samples were fed into a cylindrical reactor (3-inches in diameter, 40-inches in length) at the rate~1 kg/h. The rate of movement of wood through the heated zones was controlled by controlling the auger's speed, which was set at 12 rpm. The pyrolysis temperature was set at 450°C using multiple band heaters that are employed along the reactor length. Pyrolysis breaks feed stock into three fractions: vapor, gas and char. The produced vapor and gases left the reactor and passed through a composite cooling and separation unit.

Table 3.1

Main characteristics of biomass feed stocks

<i>Characteristics</i>	<i>Pine Lumber</i>	<i>Pine bark</i>	<i>Oak wood</i>	<i>Oak Bark</i>
Ultimate analysis (%)				
Sulfur	0.019	0.035	0.022	0.028
Carbon	52.64	53.99	47.19	45.47
Hydrogen	6.09	4.40	2.50	3.26
Nitrogen	0.09	0.37	0.12	0.32
Oxygen	27.96	17.68	31.88	25.44
Proximate analysis (%)				
Moisture	13.0	23.1	18.1	25.4
Ash	0.197	0.428	0.184	0.080
Volatile matter	71.54	61.16	66.09	67.45
Fixed carbon	15.26	15.31	15.63	7.07
Heating Value (MJ/kg)	18.0	24.4	18.7	19.0

Table 3.2

Yields of the studied bio-oil

<i>Yield (%)</i>	<i>Pine Lumber</i>	<i>Pine bark</i>	<i>Oak wood</i>	<i>Oak Bark</i>
Bio-oil (wt %)	60.1	48.2	58.6	46.8
Char (wt %)	19.1	34.7	18.7	25.3
Gas (wt %)	20.8	17.1	22.7	27.9

Table 3.3

Physical and chemical properties for the bio-oil produced from four studied feed stocks

<i>Physical property</i>	<i>Pine Lumber</i>	<i>Pine bark</i>	<i>Oak wood</i>	<i>Oak Bark</i>
Water (%)	16.1	25.9	18.0	25.0
Acid value	80.6	81.1	110	120
pH	3.1	3.4	3.2	3.3
Density (g/cc)	1.20	1.15	1.21	1.23
Viscosity cSt at 50 °C	30.0	137.9	41.6	122.3
Average molecular Weight (g/mole)	400	470	390	450

Bio-oil was derived from the condensed vapor that is a mixture of aerosol, mist, steam and condensable organics. The yields of the studied bio-oil are summarized in Table 3.2. In Table 3.2, the gas yield of the studied bio-oil was calculated by taking difference from the measured bio-oil and char yield. After preparation, all samples were characterized both physically and chemically. All analytical determinations were determined in duplicate and the average value was reported in the tables 3.2 and 3.3. The characteristics of bio-oil from pine bark and pine lumber feed stock were reported earlier [17]. Table 3.3 summarizes the physical and chemical properties of all the four bio-oils.

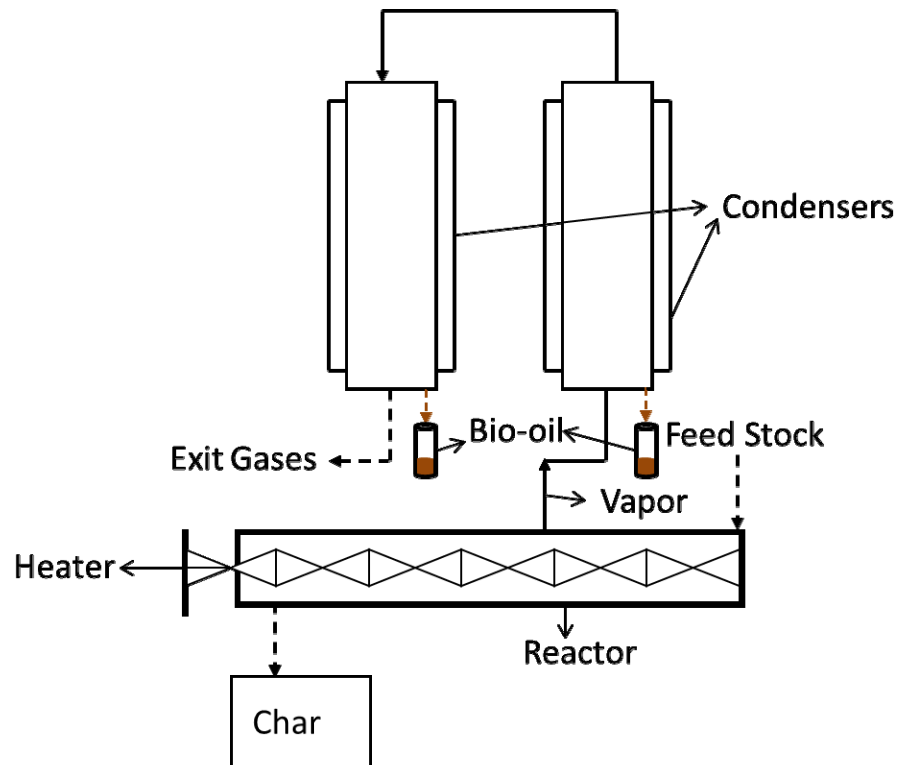


Figure 3.1

Schematic of the Mississippi State University small-scale auger reactor system

Experimental Setup

The experiment with 532 nm excitation was carried out with a Diode pumped solid state laser module (RGB LLC, FB-532-450). A dual output He-Cd CW laser (Melles Griot, Series 56) was used for the 325 nm and 442 nm sample excitation. The ND (neutral density) filters were used to adjust the laser intensity for the sample excitation. An Ocean Optics Reflection/Backscattering Y-shaped probe (R200-REF) was used for both exciting and collecting LIF signals. This probe consists of seven optical fibers, each having a core diameter of 200 μm with a single launching fiber surrounded by six collecting fibers (as shown in Figure 3.2). The excitation light source was coupled

to the excitation arm of the Y-shaped reflection probe through a plano-convex lens (f: 5cm). Typical laser energy coupled to the fiber was 2mW. The diverging output beam from the fiber provided nearly uniform illumination on the sample. Each sample was excited continuously for an hour.

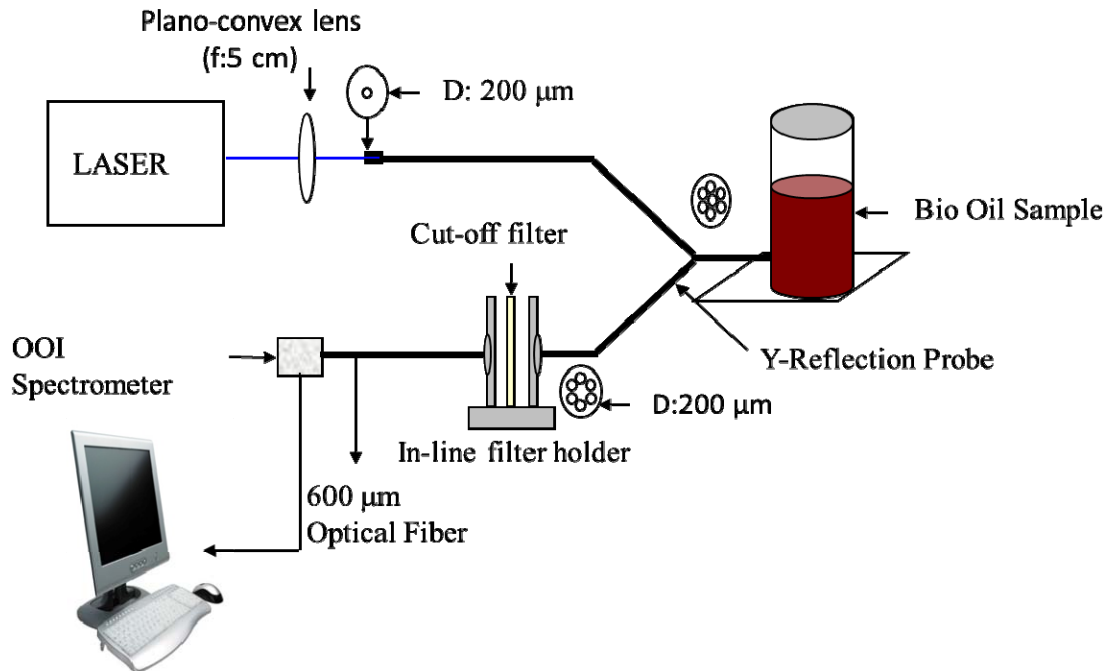


Figure 3.2

Experimental setup for bio-oil study

The fluorescence signal in the backward direction (180° collection geometry) was collected by a ring of six optical fibers mentioned earlier. The collected LIF signal was transmitted through an online filter module. A long pass cut-off filter was used in the line to filter the back-scattered laser beam (375nm, 475 nm and 570 nm long pass filter for 325 nm, 442 nm and 532 nm respectively). After suppressing the excitation light, the

signal was further transmitted through a 600 μm core diameter, UV-grade, fused-silica, auxiliary fiber. The LIF signal was recorded using a miniature spectrometer (Ocean Optics, Inc. USB2000) with 600 lines/1 mm grating. The OOI spectrometer was interfaced with a personal computer via USB port. The LIF spectra of samples were taken every five minutes using OOIBase32 data acquisition software. The spectrometer was exposed for 10 ms to get a spectrum, and each collected spectra was an average of five spectrums.

Synthetic Bio-Oil

A synthetic bio-oil was prepared to overcome the serious limitation posed by the complex nature of pyrolysis bio-oil, in studying the photo-induced reactions. In literature, Fisk *et al.* have reported synthetic bio-oil with a simple composition that they used for studying the catalytic upgrading of bio-oil [18]. Synthetic bio-oil is composed of compounds that represent the most reactive functional groups and similar wt% of compound classes (i.e. water, sugar, aldehyde, carboxylic acid, ketone, and phenol) that are present in bio-oil. The following method was used for the preparation of synthetic bio-oil. Initially, glucose and vanillin were mixed in water and put on a magnetic stirrer for three hours so that both solids would homogeneously mix with water. Later, methanol, acetic acid, glyoxal, acetol, furfural, and guaiacol were added. Finally, acetaldehyde was added (due to a low boiling point of $\sim 20.2^\circ\text{C}$), and the homogeneous mixture was stored in a cool, and dry place.

Results and Discussion

In initial study, the effect of higher wavelengths of the solar spectrum was explored. All four bio-oils were excited for one hour with 532 nm and 442 nm lasers, respectively. To monitor the chemical change, the LIF spectrum was recorded every five minutes. No change in shape or intensity was observed. The study of the LIF spectrum clearly shows that there is no effect of visible radiation on the chemical stability of bio-oil. Figure 3.3 shows the LIF spectrum of pine lumber oil excited with 532 and 442 nm wavelengths.

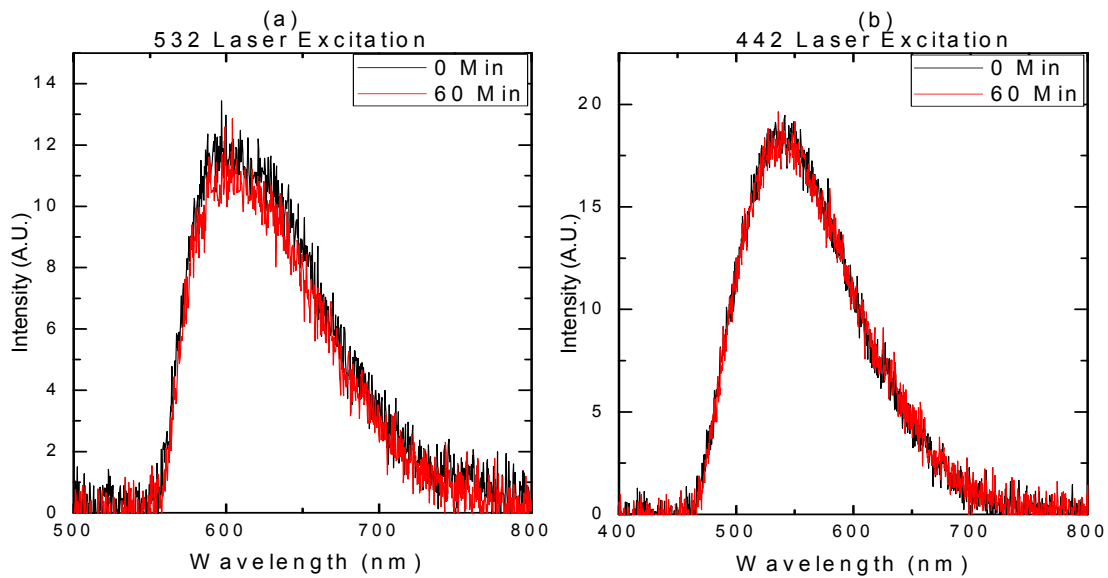


Figure 3.3

LIF spectra of Pine Lumber Oil with (a) 532 laser excitation (b) 442 laser excitation

In order to see the effect of UV radiation, the 325 nm laser was used. All bio-oil samples were excited for one hour, and the LIF signal was recorded every five minutes. The observation of the LIF spectrum shows that the peak intensity increased with time.

Under stable conditions, the fluorescence intensity emitted by a fluorophore does not change with time. The increment in the LIF peak intensity shows that the number density of electronic transitions involved in the photon emission at central wavelength (in collective fluorescence from all the constituents of the bio-oil) is increasing. It signifies the presence of photo-induced conversion on the exposure of a 325 nm laser. It is worth mentioning that a longer exposure with a high power laser could cause a photo chemical destruction of the fluorophore that can be observed in the form of decrease in fluorescence intensity or “photobleaching” [19]. Since the author’s interest was to simulate the effect of solar radiation, a relatively low intensity excitation was used. A plot of variation in LIF peak intensity with time for pine lumber oil is shown in Figure 3.4(a). The time behavior of the normalized LIF spectrum from bio-oil samples was also studied. Figure 3.4(b) shows the initial shape of all bio-oil samples, as started exciting with laser energy. The shape of the LIF spectrum from all bio-oil samples was different, which shows that the concentration of various fluorophore (in collective fluorescence) was different in all samples. This variance may be related to the difference in the chemical compositions of the four feedstocks. After one hour of excitation, the shape of the bio-oil samples was again recorded. The recorded spectrum shown in Figure 3.4(c), shows that all four bio-oil samples have similar shapes. It indicates the fact that the photo-induced reaction in all bio-oils is driving them towards a chemical change that results in similar fluorescence. This was an unusual result, so a detailed study was performed to understand the mechanism involved in this conversion.

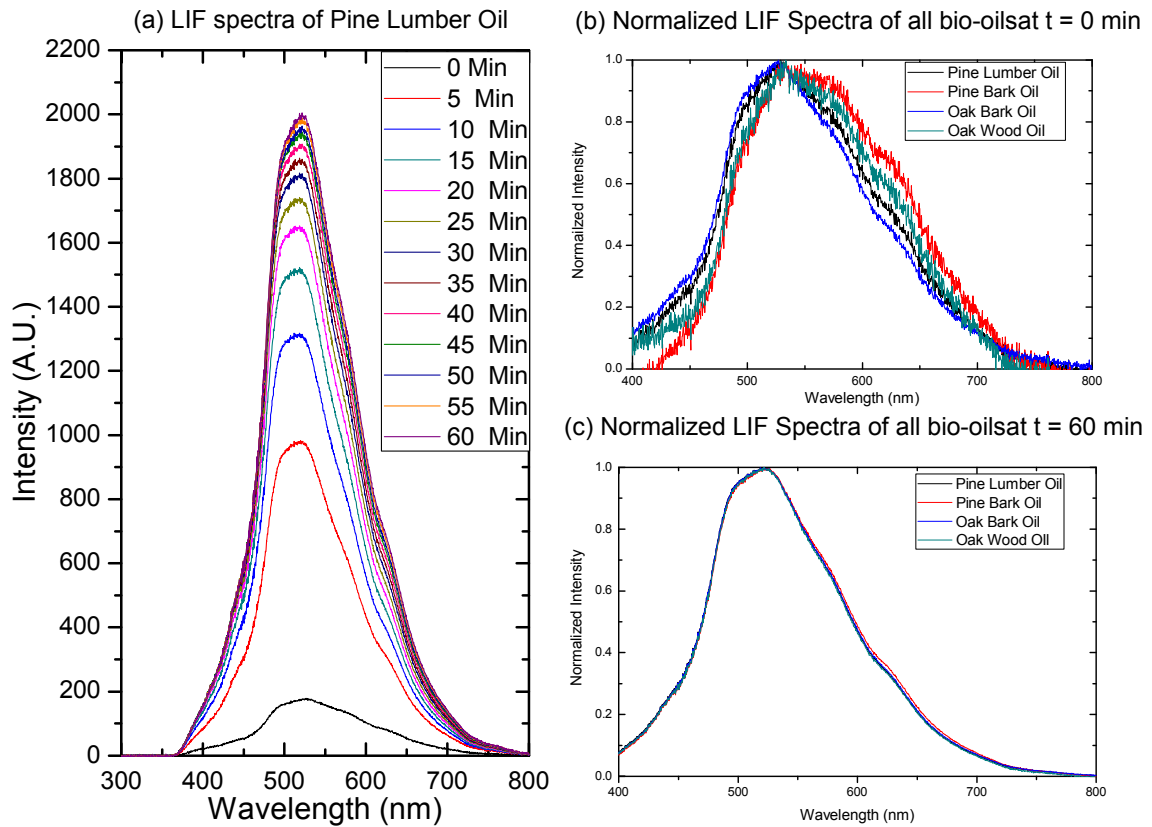


Figure 3.4

LIF spectra of bio-oil samples on excitation with 325 nm laser

The higher complexity of raw bio-oil that consists of more than 400 chemical compounds creates a difficulty in understanding and explaining the chemical changes that occur in bio-oil. Therefore, the experiments were repeated in less complex, synthetic bio-oil. Synthetic bio-oil simplifies the system in terms of chemical composition without losing the complexity in terms of its physical and chemical characteristics. Initially, the synthetic bio-oil was prepared with composition used by Fisk *et al.* [18]. The LIF spectrum obtained for the (synthetic) bio-oil is shown in Figure 3.5(a). The figure illustrates that the (synthetic) bio-oil was showing similar results as the increase in LIF

peak with time, however, the shape of the LIF spectrum did not resemble with the LIF spectrum obtained from raw bio-oil samples. Also, the LIF spectrum in Figure 3.5(a) shows a fast dynamic behavior in the first five minutes, after that, it was saturated. In order to seek a similar optical behavior as shown by raw bio-oil, several compositions of synthetic bio-oil from the same individual ingredients were tried, without changing the wt% of the compound classes present in bio-oil. The final composition was decided by observing the LIF spectrum obtained after sample excitation. The composition of the synthetic bio-oil that shows the best resemblance of LIF with the studied bio-oil is given in Table 3.4.

Table 3.4

Chemical composition of synthetic bio-oil

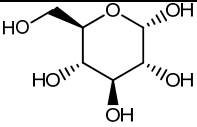
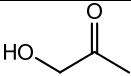
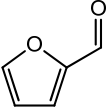
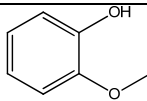
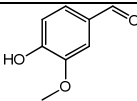
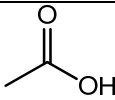
<i>Chemical Composition</i>	<i>Molecular Structure</i>	<i>Wt % ($\pm 0.1\%$)</i>
Water	H ₂ O	20
Glucose		8
Acetol		8
Furfural		4
Guaiacol		10

Table 3.4 (Continue)

Acetaldehyde		12
Vanillin		15
Methanol		5
Acetic Acid		14
Glyoxal		4

The LIF spectrum of the synthetic bio-oil used in this study is shown in Figure 3.5(b). A comparison of variation in LIF peak intensity of all the studied bio-oils with synthetic bio-oil is shown in Figure 3.6. The following methods have been employed for the calculation of peak height: (1) A second order polynomial is fitted around peak to estimate the central wavelength at spectral peak. (2) A 9 point average of spectral peak intensity is taken around central wavelength. In order to account for time average, 10 spectra are processed each time. Experimental error is estimated by determining the standard deviation associated with the calculation. This figure demonstrates that the synthetic bio-oil was showing slow increments in the peak intensity variation in the first ten minutes. Afterward, it followed a similar trend as the other oils. The observed slow increment of peak intensity in the initial time duration could be associated with the

simplified composition of the synthetic bio-oil, as nature of florescence is also dependent on the interaction between fluorophore and its immediate environment.

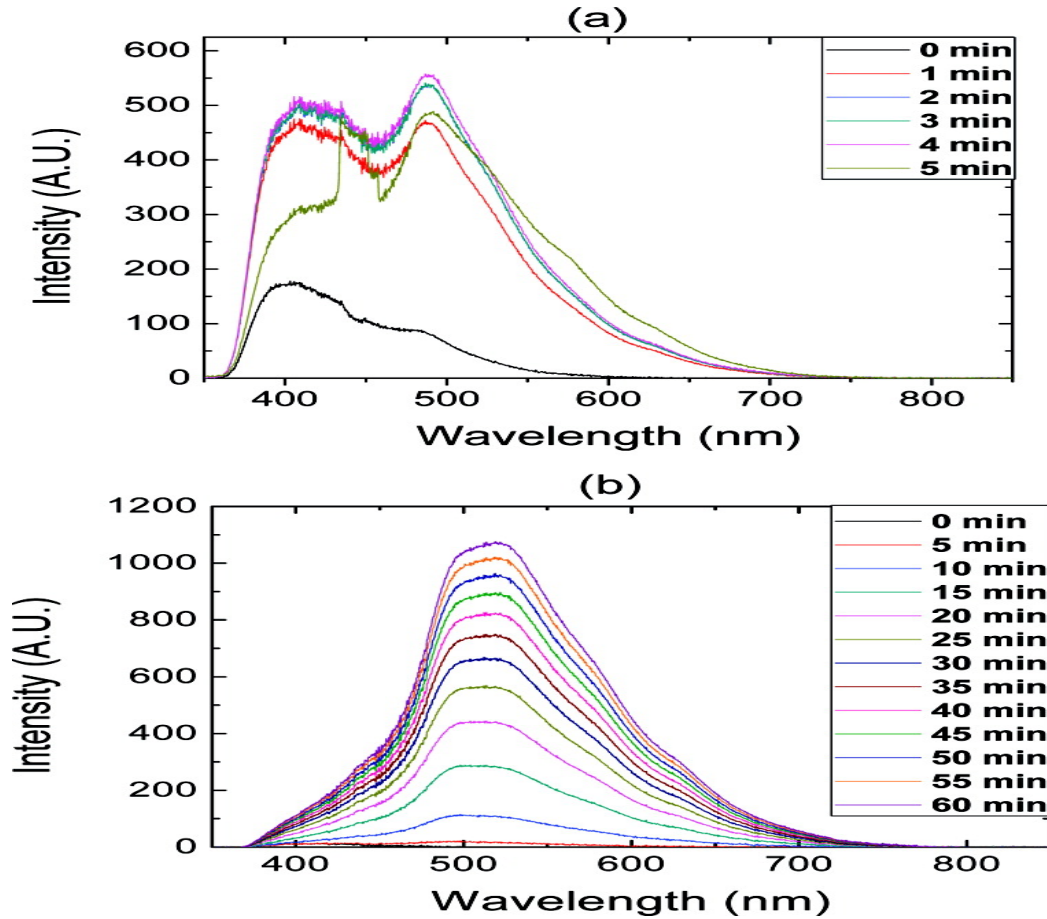


Figure 3.5

Variation in intensity of synthetic bio-oil after exciting it with 325 nm laser (a) Fisk *et al.* composition (b) Composition used in the present study (Given in Table 3.4)

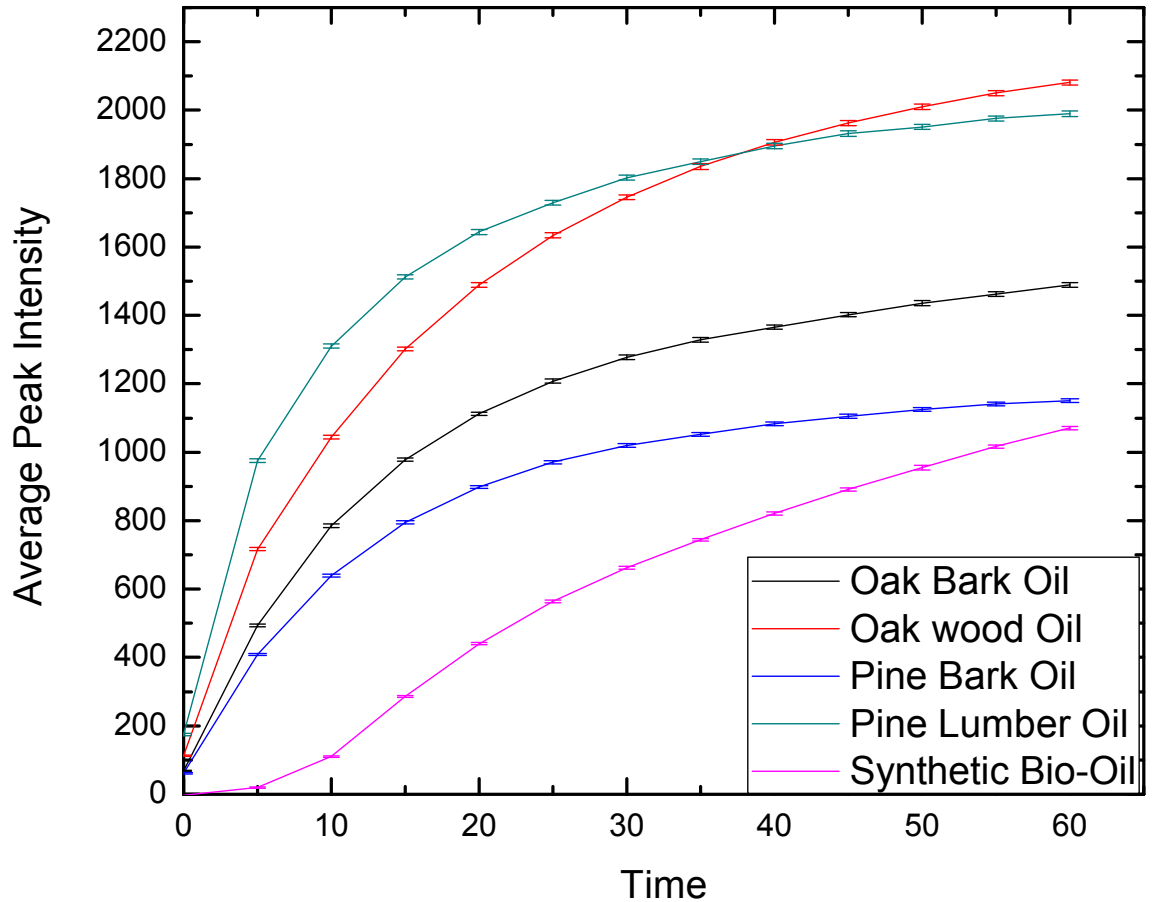


Figure 3.6

Variation of LIF peak intensity with time in studied bio-oils

After obtaining a simple-composition of synthetic bio-oil, further analysis was simple. Each constituent chemical compound was excited individually with a 325 nm laser. Glucose was dissolved 10 wt% in water for recording the LIF spectrum, and Vanillin was dissolved 10 wt% in dichloromethane. No fluorescence was observed from water, methanol, glucose, or acetic acid. Acetaldehyde, acetol, furfural, and glyoxal produced a time-independent LIF spectrum. The LIF spectrum of guaiacol and vanillin, two compounds added in the synthetic bio-oil to represent that the lignin degraded

phenolic compounds, were changing with time. The dynamic change in LIF intensity proves that the photo-induced reaction with the interaction of 325 nm radiation is related to the presence of phenolic compounds existing in the bio-oil. The LIF spectrum of synthetic bio-oil ingredients is shown in Figure 3.7. Figure 3.7(e) and 7(f) show the dynamics of LIF peak intensity in vanillin and guaiacol respectively.

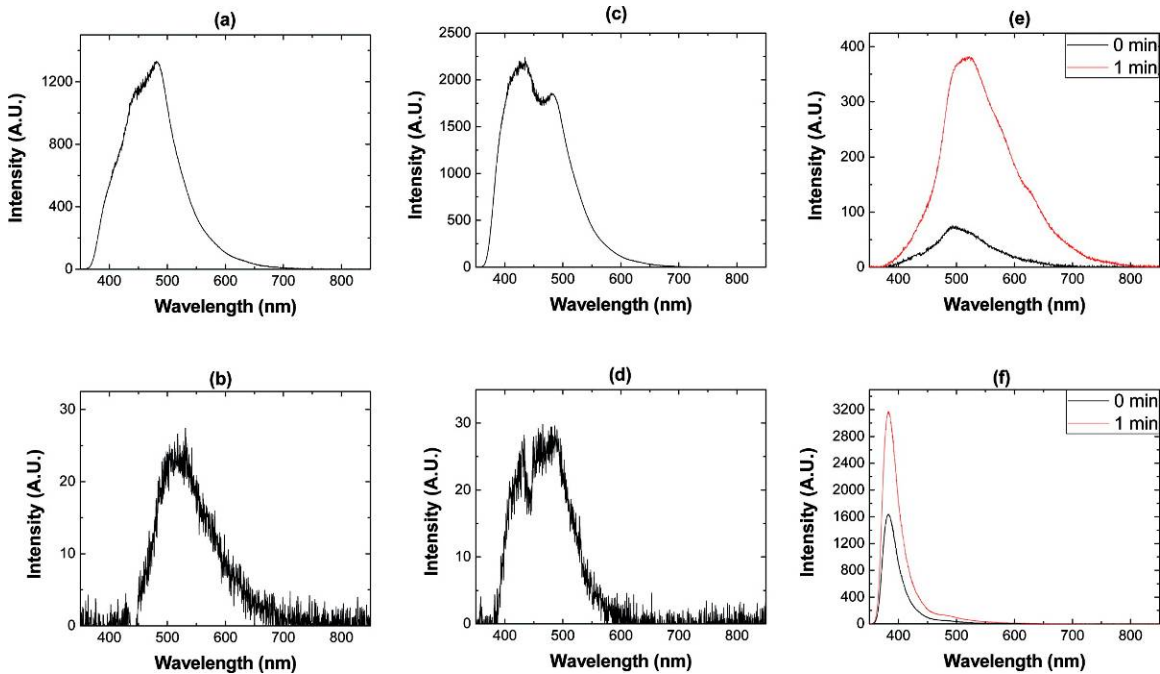


Figure 3.7

LIF spectra of individual ingredients of synthetic bio-oil

Photo-degradation of the phenol in the presence of ultraviolet (UV) is widely studied in literature [20-23]. Aromatic ring oxidation, ring cleavage, and carboxylic acid formation are a few important reactions that lead to degradation in the phenols in the presence of UV [20]. These reactions will degrade the phenolic compounds present in

the bio-oil. The reaction dynamics of the photo degradation will be dependent on the intensity of the UV and duration of exposure. Degradation of phenolic compounds will severely affect the quality of the produced bio-oil. Further work is needed to understand the details of the reaction dynamics of the bio-oil in the presence of UV light.

Conclusion

Bio-oil is one of the prominent candidates anticipated to replace crude oil. It is shown in the present paper that the exposure of UV will degrade the phenolic compounds present in bio-oil. Photo reactions involved in the degradation will be dependent on the intensity of UV and time period of exposure. A detailed study is required to understand the dependence of reaction dynamics on the intensity of UV and duration of exposure. Presently, bio-oils are produced at laboratory scale and are stored in containers that can absorb UV. This research finding would be more significant in future when big scale production of bio-oil will start in refineries. In that situation, bio-oil can get exposed to UV present in sunlight (while production, storage, and transportation), and a prolonged exposure to light would degrade the quality of the bio-oil for energy applications.

Acknowledgement

This effort was funded by Mississippi State University's Sustainable Energy Research Center (SERC) through Grant no. DE-FG36-06-G086025.

References

- [1] Bridgwater, A.V.; Toft, A.J.; Brammer, J.G. *Renew. Sust. Energ. Rev.* 2002, 6, 181 - 246.
- [2] Mohan, D.; Pittman Jr., C. U.; Steele, P. H. *Energ. Fuel* 2006, 20, 848 - 889.
- [3] Chiaramontia, D.; Oasmaa A.; Solantausta, Y. *Renew. Sust. Energ. Rev.* 2007, 11, 1056-1086.
- [4] Wang, S.; Gu, Y.; Liu, Q.; Yao, Y.; Guo, Z.; Luo, Z.; Cen, K. *Fuel Process. Technol.* 2009, 90, 738-745.
- [5] Czernik, S.; Johnson, D. K.; Black, S. *Biomass Bioenerg.* 1994, 7, 187-192.
- [6] Chaala, A.; Ba, T.; Garcia-Perez, M.; Roy, C. *Energ. Fuel* 2004, 18, 1535-1542.
- [7] Ji-lu, Z. *J. Anal. Appl. Pyrol.* 2007, 80, 30-35.
- [8] Lédé, J.; Broust, F.; Ndiaye, F.; Ferrer, M. *Fuels* 2007, 86, 1800-1810.
- [9] Zheng, J.; Yi, W.; Wang, N. *Energ. Convers. Manage.* 2008, 49, 1724-1730
- [10] Sheng, H.; Chao, Q.; Xingguo, C.; Shujie, M.; Tianhui, R. *Pet. Sci. Technol.* 2006, 24, 859-870.
- [11] D'Auria, M.; Emanuele, L.; Racioppi, R.; Velluzzi, V. *J. Photoch. Photobio. A* 2008, 198, 156–161.
- [12] Mouillet, V.; Farcas, F.; Besson, S. *Fuel* 2008, 87, 2408-2419.
- [13] Goga, N.O.; Demco, D.E.; Kolz, J.; Ferencz, R.; Haber, A.; Casanova, F.; Blümich, B. *J. Magn. Reson.* 2008, 192, 1-7.
- [14] Haywood, R.; Rogge, F.; Lee, M. *Free Radical Bio. Med.* 2008, 44, 990-1000.
- [15] Hayashi, D.; Hoeben, W.; Dooms, G.; Veldhuizen, E.; Rutgers, W.; Kroesen, G. *Appl. Optics* 2001, 40, 986-993.
- [16] Ingram, L.; Mohan D.; Bricka, M.; Steele, P.; Strobel, D.; Crocker, D.; Mitchell, B.; Mohammad, J.; Cantrell, K.; Pittman Jr., C.U. *Energ. Fuel* 2008, 22, 614 - 625.
- [17] Hassan, E.M.; Yu, F.; Ingram, L.; Steele, P. *Energ Source A* 2009, 31, 1829 – 1839.
- [18] Fisk, C.; Crofcheck, C.; Crocker, M.; Andrews, R.; Storey J.; Lewis Sr., S. *An ASABE Meeting Presentation, Paper No. 066035, Portland, Oregon 2006.*

- [19] Lakowicz, J. R. Principles of fluorescence spectroscopy (Third Edition); Springer 2006, 608.
- [20] Roig, B.; Gonzalez, C.; Thomas, O. Spectrochim. Acta. A 2003, 59, 203-207.
- [21] Mokrini, A.; Oussi, D.; Esplugas, S. Water Sci. Technol. 1997, 35, 95-102.
- [22] Scheck, C. K.; Frimmel, F. H. Water Res. 1995, 29, 2346-2352.
- [23] D'Auria, M.; Emanuele, L.; Racioppi, R.; Velluzzi, V. J. Hazard. Mater. 2009, 164, 32-38

CHAPTER IV
AN OPTICAL SENSOR FOR MULTI-SPECIES IMPURITY MONITORING IN
HYDROGEN FUEL*

Abstract

Hydrogen is the fuel used by the National Aeronautics and Space Administration (NASA) for the Space Shuttle Main Engine (SSME), among others. The purity of the hydrogen fuel is very important for the performance of hydrogen-fueled engines. In the present work, a state-of-the-art laser-induced breakdown spectroscopy (LIBS) based optical sensor to detect four important trace level impurities (i.e. nitrogen, argon, oxygen, and helium) in hydrogen is designed, developed, and tested. The sensor can simultaneously measure the concentrations of nitrogen, argon, oxygen, and helium in hydrogen fuel storage tanks and supply lines. LABVIEW[®] based software is also developed to control and operate the optical sensor. The software performs the data analysis and provides elemental concentrations (in ppm) of these impurities. The sensor

* Note: Most of the content of this chapter is based on an article written by author and co-workers, Markandey M. Tripathi, Kemal E. Eseller, Fang-Yu Yueh, and Jagdish P. Singh, An optical sensor for multi-species impurity monitoring in hydrogen fuel, which is currently under review to be published in Sensors and Actuators B: Chemical.

has estimated limits of detection of 80 ppm for nitrogen, 97 ppm for argon, 10 ppm for oxygen, and 25 ppm for helium. This prototype sensor is easy to deploy in the field.

Introduction

Hydrogen is the primary fuel used by the National Aeronautics and Space Administration (NASA) for the rocket engines employed in space shuttles [1]. Typically, the hydrogen is stored in large tanks before use. The stored hydrogen may become contaminated by one or more of several trace impurities such as nitrogen, argon, oxygen, and helium. These impurities may come from atmospheric air leaks, or may be introduced during the production of the hydrogen. The purity of the hydrogen fuel is very important for the performance of hydrogen-fueled engines. Hence, quality of the hydrogen is frequently checked in storage tanks and in feed lines. The time-consuming nature of laboratory based hydrogen quality analysis argues for the development of a sensor to perform online, near real time, and non-intrusive monitoring of hydrogen purity.

Optical spectroscopy based sensors for sensing gases, have been widely explored [2]. For instance, near-infrared absorption (NIR) spectroscopy for the natural gas detection [3], cavity ring-down spectroscopy (CRDS) for the methane detection [4], Raman spectroscopy for the H₂ detection [5], and laser induced fluorescence (LIF) spectroscopy for the aromatic hydrocarbon detection [6], are some of the recent published works on gas sensing using optical spectroscopy. Most of the aforementioned techniques can detect a single species at one time. Multi-species optical sensing requires the simultaneous study of spectroscopic transitions associated with all of the species of

interest. Recently, tunable diode lasers with photo acoustic spectroscopy [7], super continuum radiation sources with cavity enhanced absorption spectroscopy [8], and multimode diode lasers with correlation spectroscopy [9] were employed for simultaneous detection of multiple trace gases. However, these methodologies may not be the right choices in designing a portable and cost effective sensor for our application.

Laser-induced breakdown spectroscopy (LIBS) is one of the emission spectroscopy based techniques which can be used to probe gaseous mixtures [10]. Sturm *et al.* used LIBS for simultaneous measurement of C, H, O and N in a gaseous mixture of air, CO₂, N₂, and C₃H₈ [11]. Kiefer *et al.* quantified the elemental concentrations of H and O in synthetic, ambient and expiration air by employing LIBS [12]. McNaghten *et al.* have reported the detection of trace concentrations of helium and argon in ternary mixtures with nitrogen using LIBS [13]. In the previous work [14], the feasibility of applying LIBS for trace level detection of nitrogen, argon and oxygen in hydrogen was studied. A rigorous set of experiments were performed on a laboratory based setup to evaluate the LIBS parameters for sensor design. The results of this parametric study are presented in reference 14. A separate set of laboratory based experiments were conducted to study the feasibility of LIBS for helium detection [15].

In the present work, a state-of-the-art LIBS-based optical sensor to detect four vital trace level impurities (i.e. nitrogen, argon, oxygen, and helium) that are important when hydrogen is used as a fuel for rocket engines is designed, developed, and tested. The sensor can simultaneously measure the concentrations of nitrogen, argon, oxygen, and helium in hydrogen fuel storage tanks and supply lines. The LIBS-based system uses focused, high energy, pulsed laser light to produce a laser induced plasma in the

hydrogen sample. The designed system analyzes the characteristic radiation from plasma to identify the elements present in the sample and performs the data analysis based on previously acquired calibration data. The histograms of the concentrations of these impurities in parts-per-million (ppm) are displayed during the sensor monitoring period.

Experimental

The schematic diagram of the sensor system is shown in Figure 4.1a. The system includes a BigSky/Quantel CFR 400 10 SHG GRM WS2 (532 nm, 180 mJ, 9-mm beam diameter) Nd:YAG laser that provides a high energy laser pulse to produce breakdown in the analyte sample gas. The analyte gas was kept in a high pressure, compact, sturdy, and easy-to-interface sample cell (as shown in Figure 4.1a), which was designed and built for the sensor. Purging and filling the sample cell with hydrogen was maintained by Swagelok fittings and valves. A pressure gauge monitored the gas pressure inside the cell. A safety pop-off valve set at 200 psi was attached to the sample cell. The safety valve, pressure gauge, pressure transducer, vacuum pump and sample gas line were connected to the sample cell. The operation of the sample cell was evaluated by monitoring the leakage in the system. The laser beam enters in the sample cell via one of two opposing optical quartz windows attached to each side of the cell. The optical signal was collected in the backward direction through the same optical quartz window. The optical components along with the laser head were kept in the optical sensor box as shown in Figure 4.1b. An Andor Technology Shamrock SR-303I-A spectrometer with a DH720-25F-03 ICCD detector with 1024 x 256 pixels was employed as the detection system for the LIBS optical sensor. The SR 303I spectrometer has three different

gratings installed. The spectral lines of nitrogen, argon, oxygen and helium can be detected with the best resolution by using the 1200 line/mm grating.

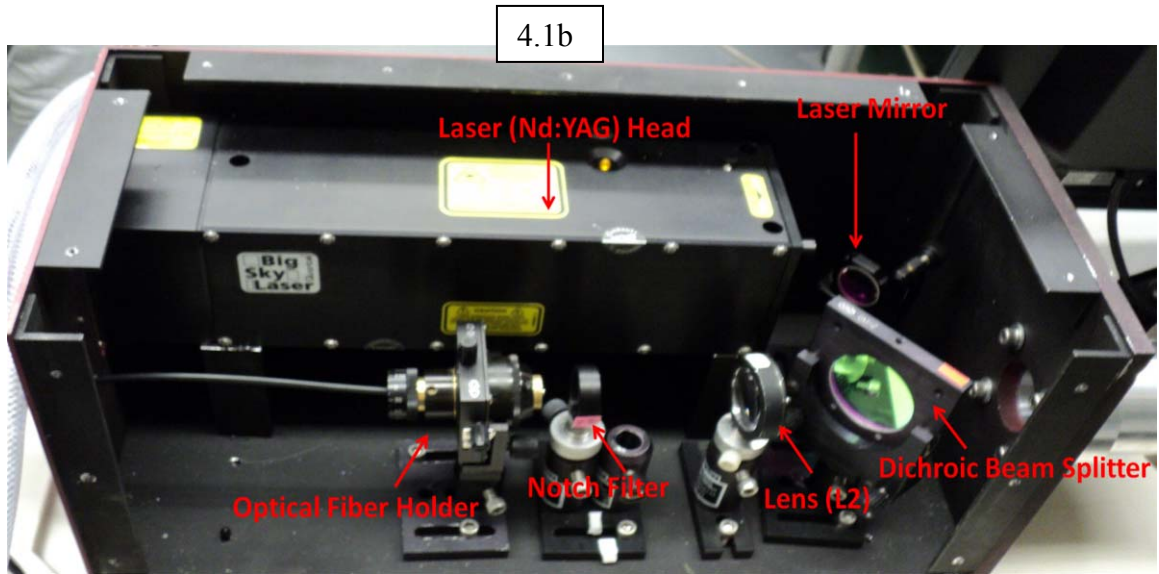
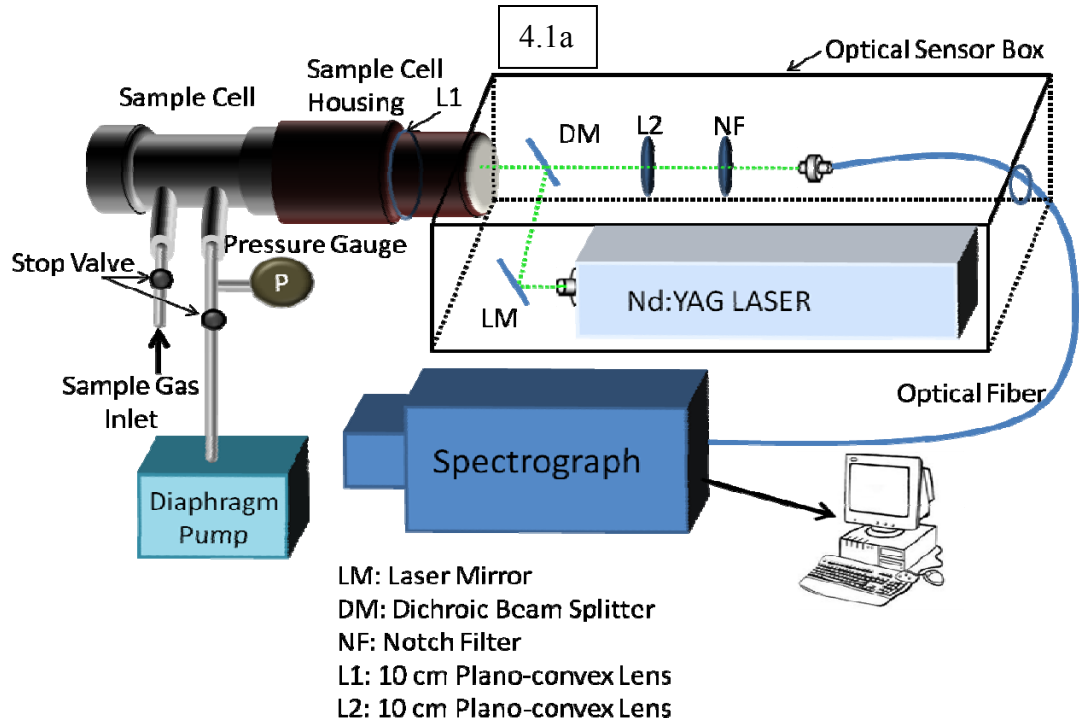


Figure 4.1

4.1a Schematic diagram of LIBS optical sensor; 4.1b Inner view of LIBS optical sensor box

The diaphragm pump (ILMVAC GmbH MPC 054Zp) was used for purging the sample cell and then filling the sample cell with a measured amount of the sample gas. A desktop computer loaded with the software written in LABVIEW[®] was used to control the operation of the laser and spectrometer as well as perform data analysis.

Optical System Design

The pulsed laser beam coming from the Nd:YAG laser with 110 mJ/pulse energy and 10 Hz pulse frequency was guided by a Nd:YAG laser line mirror (CVI Melles Griot, Y2-1037-45) on a 45° dichroic beam splitter (CVI Melles Griot, BSR-51-2037). The dichroic beam splitter reflects the 532 nm pulsed laser beam, which was then focused by a 10-cm focal length plano-convex lens (L1) into the stainless steel sample cell. This focused laser beam with a very high peak power (~14 MW) created breakdown in the sample gas. The plasma produced from the breakdown was investigated to probe the constituents of the sample gas. The dichroic beam splitter employed to guide the laser beam, reflects the 532 nm laser radiation while transmitting other wavelengths; hence, backward signal collection geometry was used to detect LIBS signal. The light emitted from the plasma was transmitted through the same lens (L1) and the dichroic mirror, in the backward direction opposite to the direction of the laser beam. The transmitted light (from the plasma) was further focused by the lens L2 onto the end of a 100- μ m optical fiber. A narrow band notch filter (17nm FWHM at 650 nm) was used in the signal collection optics to eliminate the background coming from the 656 nm hydrogen alpha line.

As the emitted signal emerges from the exit of the optical fiber, it passes into an Andor 303i Shamrock spectrometer. The LIBS signal was collected with a 3 millisecond exposure time, a 300 ns gate delay, and a 2 microsecond gate width. Each recorded LIBS spectrum was average of LIBS spectra obtained from 450 laser pulses. For the current sensor application, the spectrometer used the 1200 l/mm grating, which allowed simultaneous measurement of nitrogen, argon, and oxygen in a spectral region centered at 767 nm and helium detection in a spectral region centered at 578 nm.

Sensor Control & Operation Software

The software (developed in LABVIEW[®]) for controlling the sensor features an intuitive graphical user interface (GUI) as shown in Figure 4.2. This control software gives the user complete control on the laser output, spectrometer, data acquisition and analysis, and the display of results. The software is a user-customizable, advanced acquisition and display program that provides a real-time interface to a variety of signal-processing functions. It provides the user real-time analysis and display of impurity concentrations in ppm. Laser pulse energy and default measurement parameters for the spectrometer such as gate delay, gate width, exposure time, MCP gain, and slit width can be adjusted, and the system recalibrated. The calibration data can be saved in a file on the computer. The collected spectra for system calibration can also be saved in the computer. The saved spectra can be used for further analysis or for troubleshooting. After finishing the calibration, the user can proceed to measure an unknown sample. The real-time impurity concentrations will be displayed in a window and can be saved in a log file. The laser is connected to the computer via an RS-232 serial port, and the Andor

303i Shamrock spectrometer is connected to computer via a PCI controller card. A Software Development Kit (SDK) obtained from Andor Technology was used to write the part of the software which provides access and control of the Andor spectrometer and Intensified CCD camera.

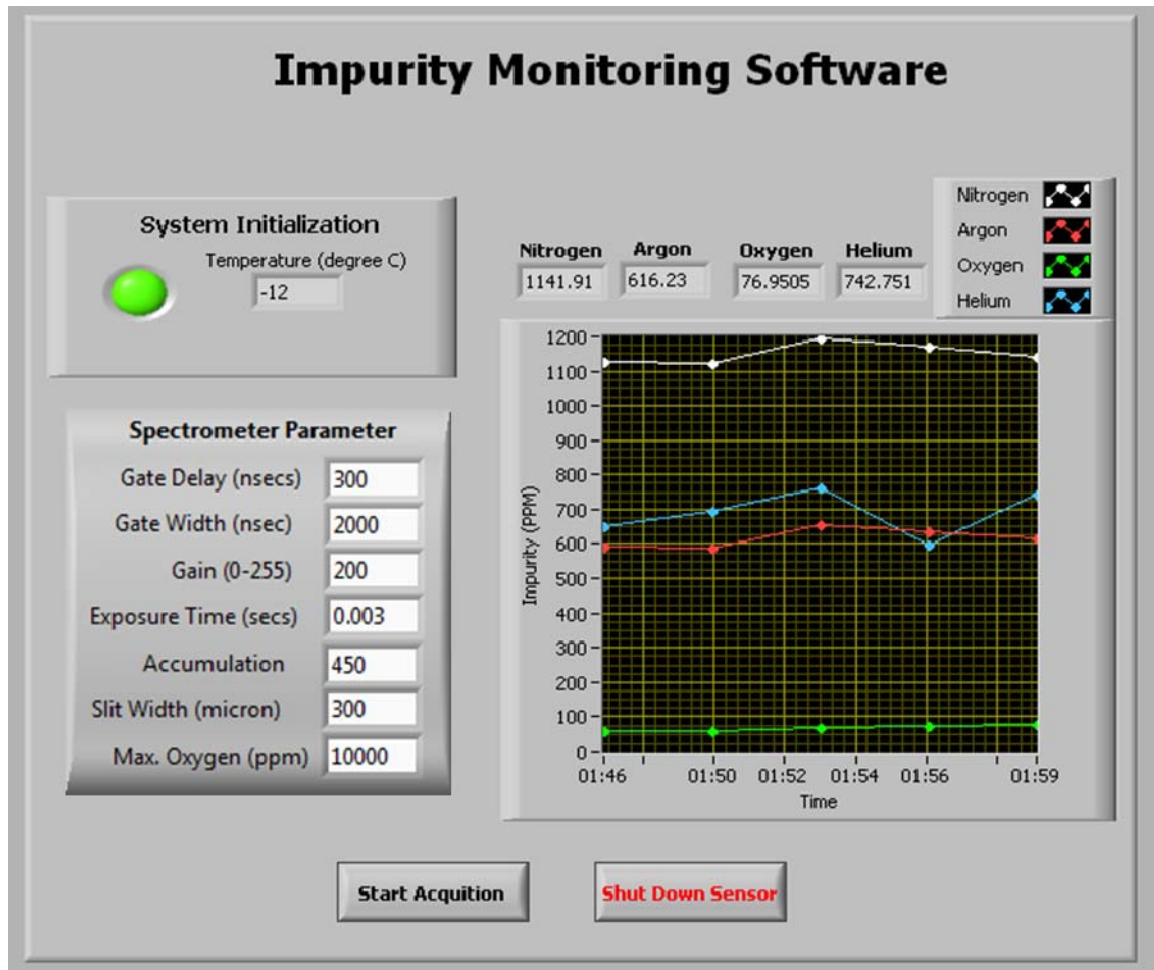


Figure 4.2

Graphical user interface of optical sensor controlling software

Results and Discussion

The impurity species of interest (i.e. nitrogen, argon, oxygen, and helium) have several signature atomic emission lines that can be used to measure their presence in a sample. Table 4.1 summarizes some of the most prominent spectral lines of the elemental impurities of interest. A broadband LIBS spectrum of the sample gas from our laboratory based setup was reported in reference 14.

Table 4.1

Atomic spectral lines of various impurities

Impurity Species	Atomic Spectral Lines (nm)
Nitrogen	575.25, 742.36, 744.23, 746.83
Argon	696.54, 706.72, 738.40, 750.39, 751.47, 763.51 , 772.38, 772.42, 794.82
Oxygen	615.68, 615.82, 700.22, 725.45, 777.19, 777.42, 777.54
Helium	388.87, 447.15, 587.56 , 706.52

The transitions shown in bold in Table 4.1 were the ones chosen for the concentration measurements in this study. This selection was based on their relative intensity in the spectra and interference with the atomic emissions from other species (i.e. hydrogen). The detection system (Andor Technology SR-303I spectrometer) had three gratings installed (300 lines/mm, 600 lines/mm, and 1200 lines/mm). The 300 line/mm grating gives the greatest spectral coverage and can simultaneously detect the spectral lines of all of the elements of interest: helium, nitrogen, argon and oxygen. However, its low spectral resolution makes it difficult to resolve some spectral lines. The 1200

line/mm grating gives the best resolution but it cannot simultaneously detect all impurities due to the narrow spectral range coverage. Hence, a two-step impurity detection scheme was employed in the development of the control and operation software. Initially, the sensor takes LIBS spectra with the grating centered at 764 nm to measure nitrogen (746.83 nm), argon (763.51 nm), and oxygen (777.35 nm). Subsequently, the grating moves to 577 nm for the measurement of helium (587.56 nm). These spectra are shown in Figure 4.3 and 4.4, respectively.

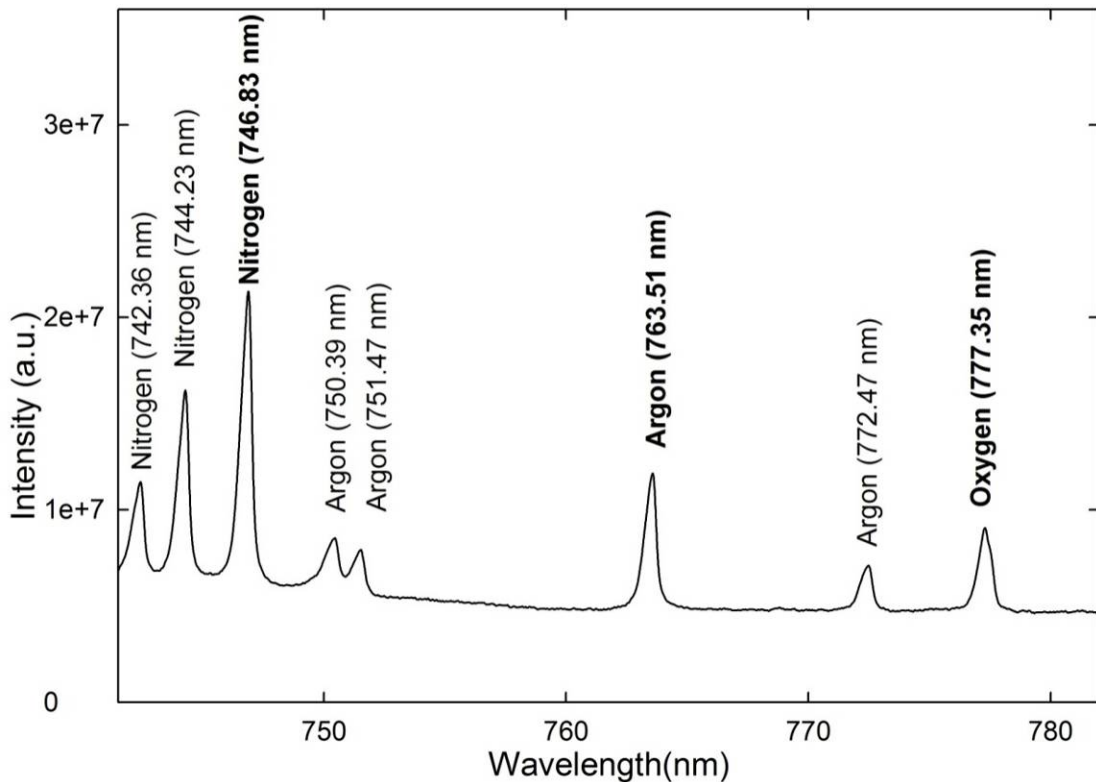


Figure 4.3

LIBS spectra of hydrogen sample (with nitrogen 10000 ppm, argon 5000 ppm, oxygen 400 ppm, and helium 5000 ppm) in 764 nm spectral region

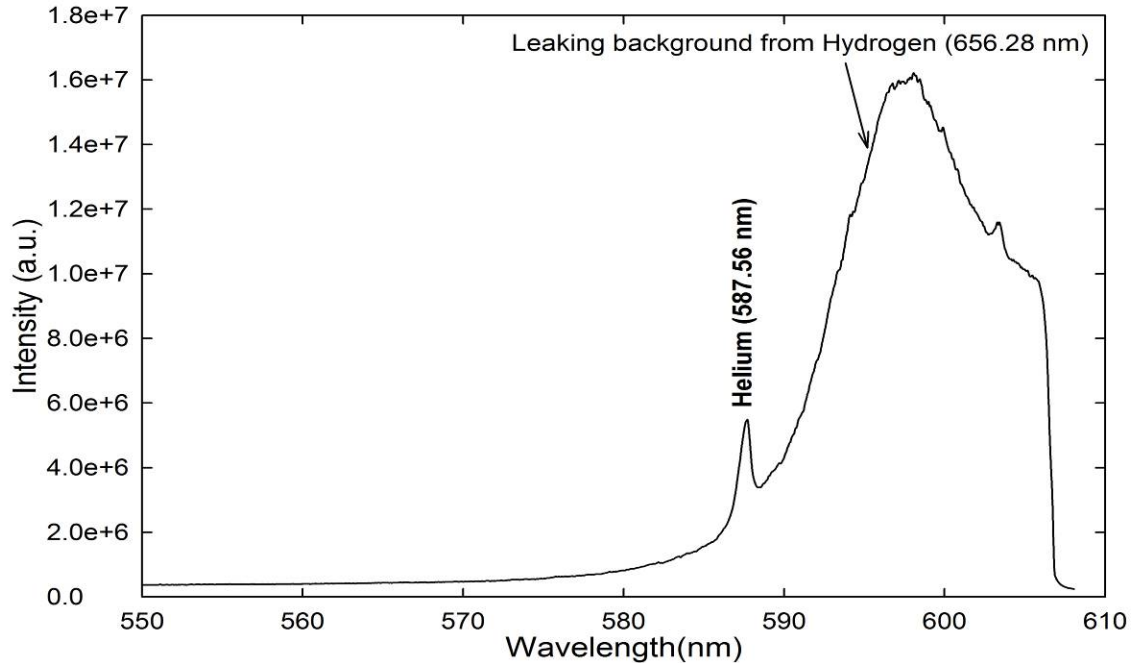


Figure 4.4

LIBS spectra of hydrogen sample (with nitrogen 10000 ppm, argon 5000 ppm, oxygen 400 ppm, and helium 5000 ppm) in 577 nm spectral region

The detection of helium at 587.56 nm was challenging due to the presence of a nearby hydrogen spectral line at 656.28 nm. The helium line was completely overwhelmed by the very high spectral background from the hydrogen line at 656.28 nm. The high intensity of 656.28 nm line was due to the high hydrogen concentration (> 95 %) in the sample along with high transition probability of the spectral line [16]. Several different filters were evaluated to reduce this strong hydrogen background and thus improve the signal to the background ratio. It was observed that a notch filter at 650 nm with a bandwidth of 17 nm FWHM (from Iridian Spectral Technologies) provided the best signal to background ratio. This filter was included in the final design of the optical sensor. Figure 4.5 shows LIBS spectra in the 764 nm spectral region, showing the effect

of the notch filter. Those spectra were both recorded with the 1200 l/mm grating blazed at 750nm. The high spectral background observed in the spectrum recorded without the notch filter is believed to be from the scattering of the stronger hydrogen atomic emission inside the spectrometer. The LIBS spectra in the 577 nm region was not recorded without the notch filter due to the detector saturation caused by light leakage and charge spill-over from the strong hydrogen signal center at 656.28 nm. The leaking background from this hydrogen spectral line can still be seen in the LIBS spectra acquired with the notch filter (see Figure 4.4).

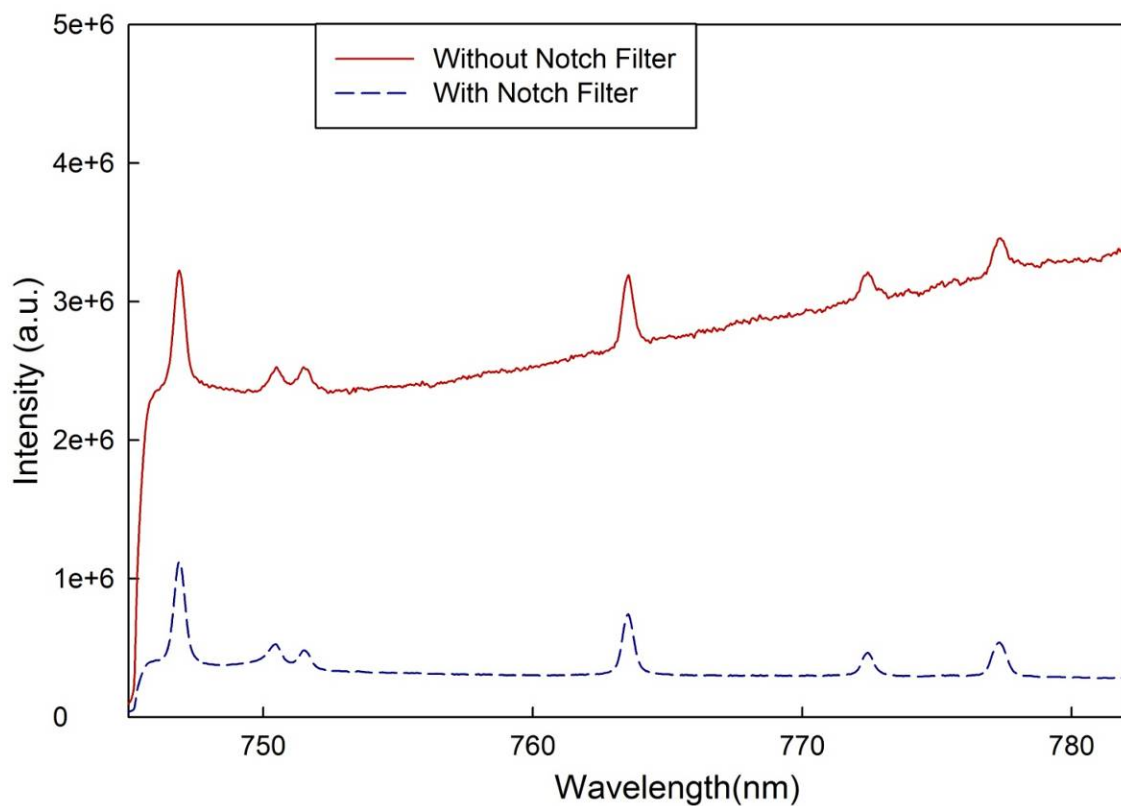


Figure 4.5

LIBS spectra recorded with and without notch filter

Sample Cell Pressure

The operational pressure of the sample cell was optimized for detection sensitivity. It was found that an increase in the sample cell pressure increased the LIBS signal of the analyte lines of nitrogen, argon, and oxygen [14]. However, a reverse effect was observed with the helium analyte line (see Figure 4.6). The significant background hydrogen signal increases as the sample pressure increases, and the effect of this background signal degrades the helium signal as the sample cell pressure increases. The possibility of lowering the sample cell pressure below atmospheric pressure was considered but rejected, due to the possibility of sample contamination by air leaks. Hence, the sample cell operational pressure was chosen to be 800 torr, a little above the atmospheric pressure.

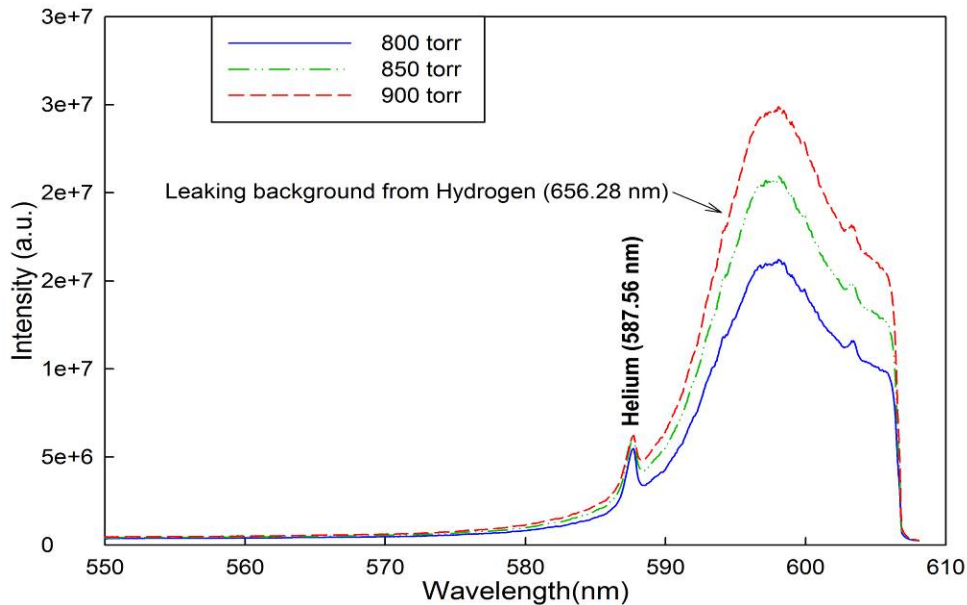


Figure 4.6

Effect of leaking hydrogen spectral line on helium spectral line at different pressure in sample cell

Sensor Calibration

For impurity measurement with LIBS, various calibration methods were tested, which includes the spectral peak intensity, the area under the spectral peak, and the area under the spectral peak normalized with the background plasma emission. It was observed that area under the spectral peak normalized with background plasma emission provided the best calibration. The data analysis part of the sensor control and operation software was coded accordingly. The area under each spectral peak was calculated by employing numerical integration by the trapezoidal rule. The background plasma emissions for nitrogen, argon, and oxygen were calculated by averaging the spectral intensity from 780.29 nm to 781.72 nm. For helium spectral peak area normalization, the average spectral intensity from 566.50 nm to 569.50 nm was used as the plasma background intensity. After repeating the aforementioned process for the entire calibration range (for each impurity), the sensor control and operation software employs linear regression on the calibration data to obtain equations for the best fit straight line for each impurity. Figure 4.7 shows the typical calibration curves obtained from four gas samples of known composition for all four impurities of interest. Figure 4.7 shows that the calibration data are all linearly correlated with the concentration of impurities with a very high regression coefficient (>0.97). The parameters of these fitted calibration lines can then be used to predict impurity concentrations in unknown hydrogen samples.

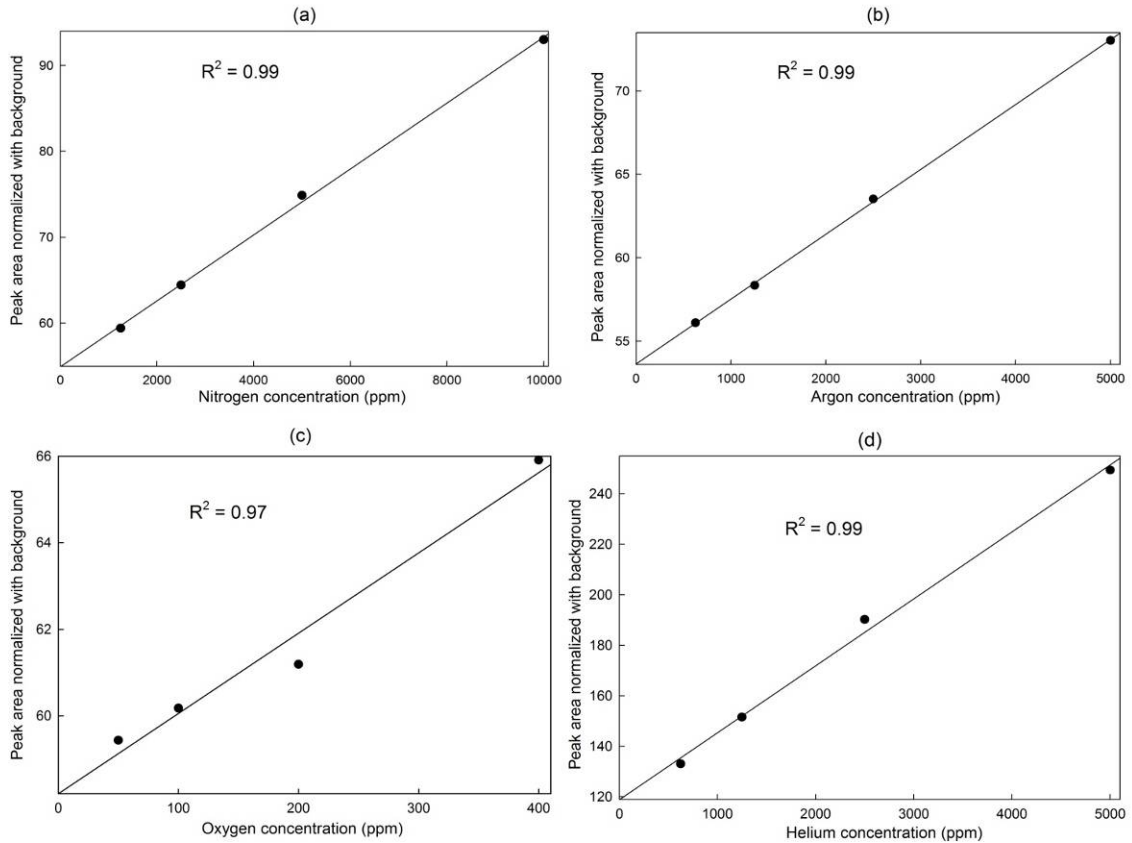


Figure 4.7

Optical sensor calibration with LIBS spectra (a) for nitrogen concentration measurement, (b) for argon concentration measurement, (c) for oxygen concentration measurement, and (d) for helium concentration measurement

Sensor Operation

Figure 4.8 shows the flow chart for the complete operation of the optical sensor. After turning on the power for the laser and spectrometer, the user will start the sensor control and operation software. The software first asks if the user wants to change the laser energy. This provision was added since the flash lamp energy may decrease after prolonged use for several years of the laser and the user may have to change the Q switch delay setting to compensate. After setting the laser power, the spectrometer initializes

itself. During initialization, a red light on the front panel of the GUI will be on. The light will turn green after initialization is complete.

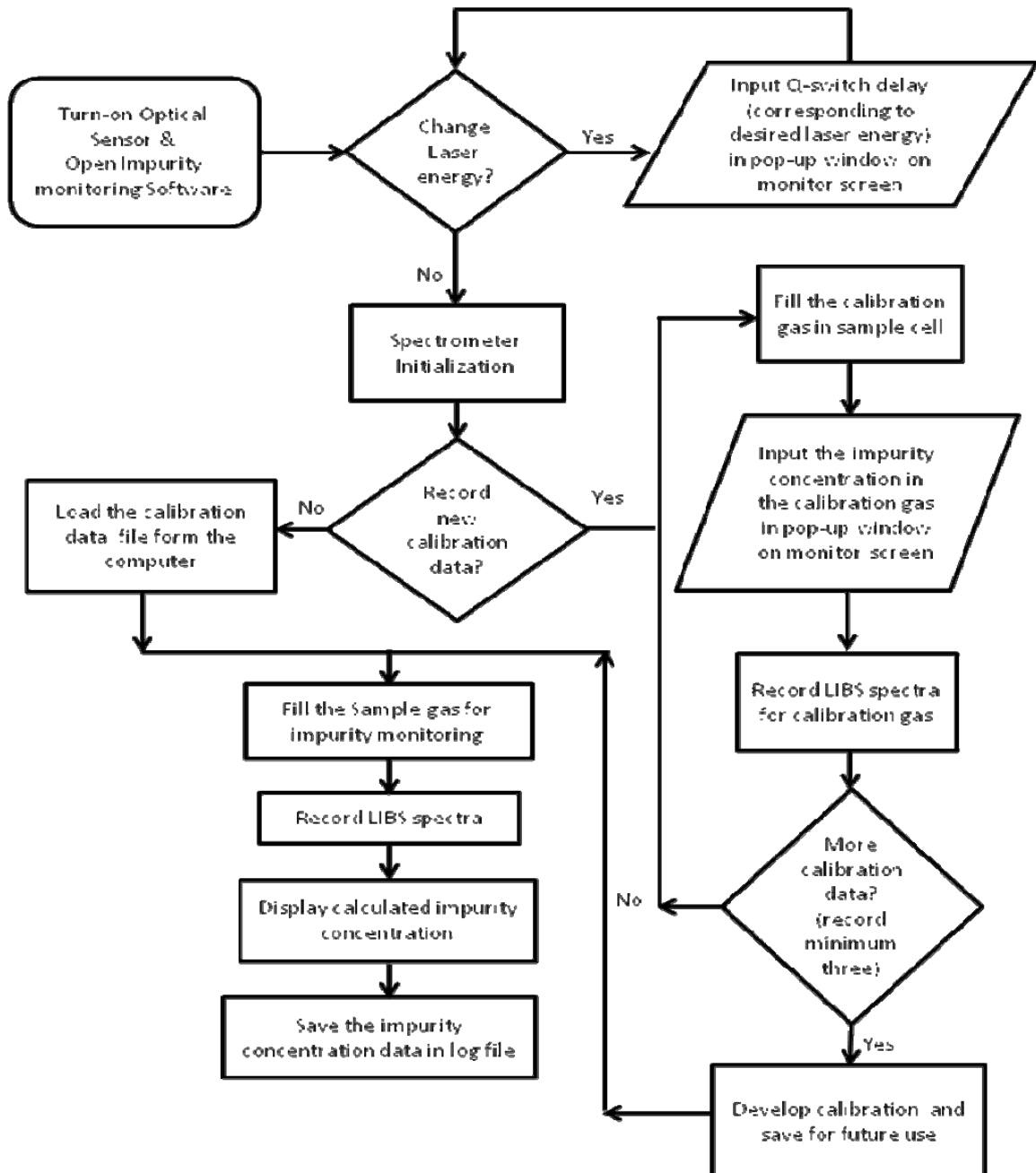


Figure 4.8

Flow chart describing operation of the optical sensor

Before analyzing an unknown sample, calibration data for the element of interest is needed. The user has the option of using previously acquired calibration data, or recording a new set of calibration data before analyzing the unknown sample. The intuitive graphical user interface of the sensor control and operation software guides the user through the calibration procedure. After completing a new calibration, the GUI asks the user to save the calibration data for future use. It is recommended to use a minimum of three calibration samples that cover the concentration ranges of interest. To measure an unknown sample, the user first fills the sample cell with the sample gas to the desired pressure then presses the “Start Acquisition” button on the GUI front panel. This begins the data acquisition and analysis process. After data processing is complete, the measured impurity concentration(s) will be displayed on the GUI front panel. This process is repeated until the user presses the “Shut Down Sensor” button. Before the software terminates, the GUI will give the user the option of saving the logged data.

The presence of oxidizer (i.e. oxygen) in fuel (i.e. hydrogen) may pose a safety hazard. Hence, the sensor was designed to measure very low concentrations of oxygen (up to 10 ppm) in hydrogen. The sensor has an emergency shutdown provision if the oxygen content rises above a preset level. The flammability limit of hydrogen in oxygen (at atmospheric pressure and 25 °C temperature) is 4% to 95% [17].

The performance of the optical sensor was evaluated for impurity concentration measurement in a hydrogen fuel sample. The spectrometer detector was cooled to -12 °C during system initialization to minimize fluctuations due to thermal noise. Figure 4.2 shows a screen shot of the graphical user interface while a test run was performed. In this test run the sample cell was filled with the hydrogen fuel sample and ran the sensor for a

prolonged period of time to evaluate the repeatability and stability of the measurement. The calibration data shown in Figure 4.7 was employed in this sensor performance test. The results of the test (see Figure 4.2) show that the concentrations of the impurities measured by this sensor are consistent throughout the test run. The helium concentration shows relatively more fluctuation than the other species. This could be due to the relative weakness of the helium spectral line in combination with the background from a nearby strong hydrogen spectral line.

Conclusion

A laser-induced breakdown spectroscopy based prototype optical sensor was developed to measure trace impurities in hydrogen used by NASA in their rocket engines. This sensor can detect four major impurities of interest (nitrogen, argon, oxygen, and helium) in the hydrogen sample. Spectral peaks at 746.83 nm, 763.51 nm, 777.35 nm, and 587.56 nm in the LIBS emission spectra were employed for the detection of nitrogen, argon, oxygen, and helium, respectively. A notch filter at 650 nm with notch width of 17 nm FWHM was employed in the detection system to filter out a strong background signal from the hydrogen emission line at 656.28 nm. This enabled the detection of the helium spectral line at 587.56 nm, which would be completely overwhelmed by the background hydrogen signal without using the notch filter. The sensor was controlled and operated by LABVIEW based software, which was developed specifically for this application. The sensor has estimated limits of detection of 80 ppm for nitrogen, 97 ppm for argon, 10 ppm for oxygen, and 25 ppm for helium. This portable prototype sensor is field

deployable. This sensor currently monitors only nitrogen, argon, oxygen, and helium in hydrogen but it can be easily modified to monitor other impurities as well.

Acknowledgements

This project was funded by the NASA Stennis Space Center–Small Business Technology Transfer (SSC-STTR) contract NNX09CB75C through Mississippi Ethanol, LLC. The authors would also like to thank Dr. Perry Norton for the critical reading of the manuscript and fruitful discussion during the project.

References

- [1] http://www.nasa.gov/topics/technology/hydrogen/hydrogen_2009.html
- [2] P.T. Mosely, J.O.W. Norris and D.E. Williams, Techniques and Mechanisms in Gas Sensing, The Adam Hilger Series on Sensors, Bristol, 1991.
- [3] X. Gao, H. Fan, T. Huang, X. Wang, J. Bao, X. Li, W. Huang, W. Zhang, Spectrochim. Acta A 65(2006), 133-138.
- [4] L. Dong, W. Yin, W. Ma, L. Zhang, Sensor. Actuat. B-Chem. 127(2007), 350-357.
- [5] Y. Oki, N. Kawada, Y. Abe, M. Maeda, Opt. Commun. 161(1999), 57-62.
- [6] R.Sun, N. Zobel, Y. Neubauer, C. Cardenas Chavez, F. Behrendt, Opt. Laser Eng. 48(2010), 1231-1237.
- [7] D.Weidmann, A. A. Kosterev, F. K. Tittel, N. Ryan, and D. McDonald, Opt. Lett. 29(2004), 1837-1839.
- [8] J. M. Langridge, T. Laurila, R. S. Watt, R. L. Jones, C. F. Kaminski, and J. Hult, Opt. Express 16(2008), 10178-10188.
- [9] X. T. Lou, G. Somesfalean, B. Chen, Y. G. Zhang, H. S. Wang, Z. G. Zhang, S. H. Wu, and Y. K. Qin, Opt. Lett. 35(2010), 1749-1751.
- [10] A. H. Schwebel, A. M. Ronn, Chem. Phys. Lett. 100(1983), 178-182.
- [11] V. Sturm and R. Noll, Appl. Optics 42(2003), 6221-6225.
- [12] J. Kiefer, J. W. Tröger, T. Seeger, A. Leipertz, B. Li, Z. S. Li and M. Aldén, Meas. Sci. Technol. 21(2010), 065303 (7pp).
- [13] E.D. McNaghten, A.M. Parkes, B.C. Griffiths, A.I. Whitehouse, S. Palanco, Spectrochim. Acta B 64(2009), 1111-1118.
- [14] K. E. Eseller, F.-Y. Yueh and J. P. Singh, Appl. Phys. B-Lasers O. 102(2011) 963-969.
- [15] K. E. Eseller, F.-Y. Yueh, J. P. Singh, and N. Melikechi, Appl. Optics 51(2012), B171-B175.
- [16] http://www.physics.nist.gov/PhysRefData/ASD/lines_form.html
- [17] M. G. Zabetakis, Flammability characteristics of combustible gases and vapors, Bulletin 627, US Bureau of Mines, Washington D.C., 1965.

CHAPTER V
CHEMILUMINESCENCE-BASED MULTIVARIATE SENSING OF LOCAL
EQUIVALENCE RATIOS IN PREMIXED ATMOSPHERIC
METHANE-AIR FLAMES*

Abstract

Chemiluminescence emissions from OH^* , CH^* , C_2^* , and CO_2^* formed within the reaction zone of premixed flames depend upon the fuel-air equivalence ratio in the burning mixture. In the present paper, a new partial least square regression (PLS-R) based multivariate sensing methodology is investigated and compared with an OH^*/CH^* intensity ratio-based calibration model for sensing the equivalence ratio in atmospheric methane-air premixed flames. Five replications of spectral data at nine different equivalence ratios ranging from 0.73 to 1.48 were used in the calibration of both models. During model development, the PLS-R model was initially validated with the calibration data set using the leave-one-out cross validation technique. Since the PLS-R model used the raw spectral intensities, it did not need the nonlinear background subtraction of CO_2^*

* Note: Most of the content of this chapter has been adapted from Fuel, Volume 93, Markandey M. Tripathi, Sundar R. Krishnan, Kalyan K. Srinivasan, Fang-Yu Yueh, and Jagdish P. Singh, [Chemiluminescence-based multivariate sensing of local equivalence ratios in premixed atmospheric methane-air flames](#), Pages 684-691, Copyright (2011), with permission from Elsevier.

emission that is required for typical OH^*/CH^* intensity ratio calibrations. An unbiased spectral data set (not used in the PLS-R model development), for 28 different equivalence ratio conditions ranging from 0.71 to 1.67, was used to predict equivalence ratios using the PLS-R and the intensity ratio calibration models. It was found that the equivalence ratios predicted with the PLS-R based multivariate calibration model matched the experimentally measured equivalence ratios within 7 percent; whereas, the OH^*/CH^* intensity ratio calibration grossly under-predicted equivalence ratios in comparison to measured equivalence ratios, especially under rich conditions ($\phi > 1.2$). The practical implications of the chemiluminescence-based multivariate equivalence ratio sensing methodology are also discussed.

Introduction

Real time measurement of local and global fuel-air equivalence ratios (ϕ) is essential for monitoring and closed-loop control of premixed combustion systems. Pollutant emissions such as oxides of nitrogen (NO_x), carbon monoxide (CO), unburned hydrocarbons (HC), and particulate matter (PM) can be reduced by controlling fuel-air equivalence ratios [1-3]. Precise control of the equivalence ratio can also help in preventing serious accidents in gas turbines such as blow-off, flashback due to pressure waves, or damage to the combustor due to combustion oscillations as these turbines operate close to the lean limit [3-4]. In internal combustion (IC) engines, advanced combustion strategies such as homogeneous charge compression ignition (HCCI) [5], low temperature combustion [6], and direct injection spark ignition [7] utilize premixed or partially premixed combustion modes to simultaneously improve engine efficiencies and

reduce pollutant emissions. To achieve controlled premixed or partially premixed combustion in IC engines, the real-time measurement and closed-loop control of in-cylinder local equivalence ratios are desirable. The present work is an attempt to utilize natural chemiluminescence emissions to diagnose equivalence ratios in premixed atmospheric methane-air flames with two different sensing methodologies: (1) a whole-spectrum multivariate calibration model and (2) an OH^*/CH^* peak intensity ratio calibration model.

Chemiluminescence emissions from OH^* , CH^* , and C_2^* formed within the reaction zone of premixed flames depend upon the air-fuel ratio in the burning mixture [8-10]. Easy, nonintrusive experimental detection of chemiluminescence coupled with fast response time provides a convenient approach for the equivalence ratio determination. Many researchers have investigated the variations in OH^* , CH^* , and C_2^* intensity ratios with the equivalence ratio [11-13]. For example, Docquier *et al.* [11] studied the effect of pressure on OH^* , CH^* , and C_2^* chemiluminescence intensity in methane-air premixed flames. They found a strong correlation between the chemiluminescence signal and pressure and suggested the need for a multi-wavelength sensor for direct monitoring of the equivalence ratio. Hardalupas *et al.* [2] showed that in natural-gas-fuelled, premixed, counter-flow flames, OH^*/CH^* is independent of strain rate and that C_2^*/CH^* and C_2^*/OH^* show a strong dependence on strain rate. In a recent study [14], it was shown that in premixed counter-flow methanol and ethanol flames, the OH^*/CH^* intensity ratio also shows dependence on strain rate. The aforementioned studies clearly indicate the need for the development of a robust sensing methodology that is applicable over a range of combustion conditions.

Many approaches have been employed for sensing equivalence ratios from chemiluminescence spectra [15]. Muruganandam *et al.* [3] and Hardalupas *et al.* [16] used the peak intensity ratio of OH^*/CH^* for sensing the equivalence ratio in combustors fueled with natural gas. Artificial intelligence-based data analysis techniques have also been explored for monitoring as well as controlling combustion processes [17]. Recently, Ballester *et al.* [18] applied the artificial neural network technique on chemiluminescence spectra obtained from the combustion of natural gas blended with hydrogen in a swirl combustor for monitoring equivalence ratios.

All of the previous studies show that the chemiluminescence emissions of OH^* , CH^* , C_2^* , and CO_2^* (the nonlinear continuous background) from the reaction zone depend on the equivalence ratio. In this work, a new multi-wavelength (multivariate) sensing methodology is proposed for the determination of equivalence ratios in premixed methane-air flames. Most of the previously reported work does not consider the whole spectrum approach. A model based on multivariate statistics is relevant for a two-dimensional (X, Y variables) data set, where the response Y-variable (equivalence ratio) depends on several explanatory X-variables (spectral wavelengths). A wide chemiluminescence spectrum (250 – 650 nm) was used to develop the multivariate calibration model. This approach ensures that the spectral intensity variations from all the excited species within the measured wavelength range are used in the development of the multivariate calibration model. The experimental results presented in this paper demonstrate that the multivariate calibration model can differentiate fuel-rich, fuel-lean, and stoichiometric premixed flames. Also, a partial least square regression (PLS-R) based multivariate calibration model is developed for equivalence ratio prediction and it

is shown that the PLS-R model successfully predicts the equivalence ratios within the developed calibration range.

Specific Objectives

The specific objectives of the present work are

- [1] To develop a multi-wavelength sensing methodology for equivalence ratio estimation and monitoring in premixed atmospheric methane-air flames.
- [2] To evaluate the predictive capability of the developed multivariate calibration model and compare its performance with an OH^*/CH^* intensity ratio calibration model over a range of equivalence ratios.

Experimental Setup

A rectangular slot burner (length: 11.2 cm, width: 0.55 cm, and height: 26 cm) was used to generate the atmospheric, premixed methane-air flames used in this study. Fuel (99.97%-pure methane) and oxidizer (breathing grade air) were mixed at room temperature, prior to entering the slot burner from the bottom end. Correlated rotameters ($\pm 2\%$ accuracy full scale) were used to measure the flow rates of methane and air. A schematic diagram of the experimental setup is shown in Figure 5.1. To cut off fuel supply to the burner in case of an emergency, a safety shutdown switch was used in the fuel line as shown in Figure 5.1. A flash arrester was also attached to the fuel cylinder as a safety precaution.

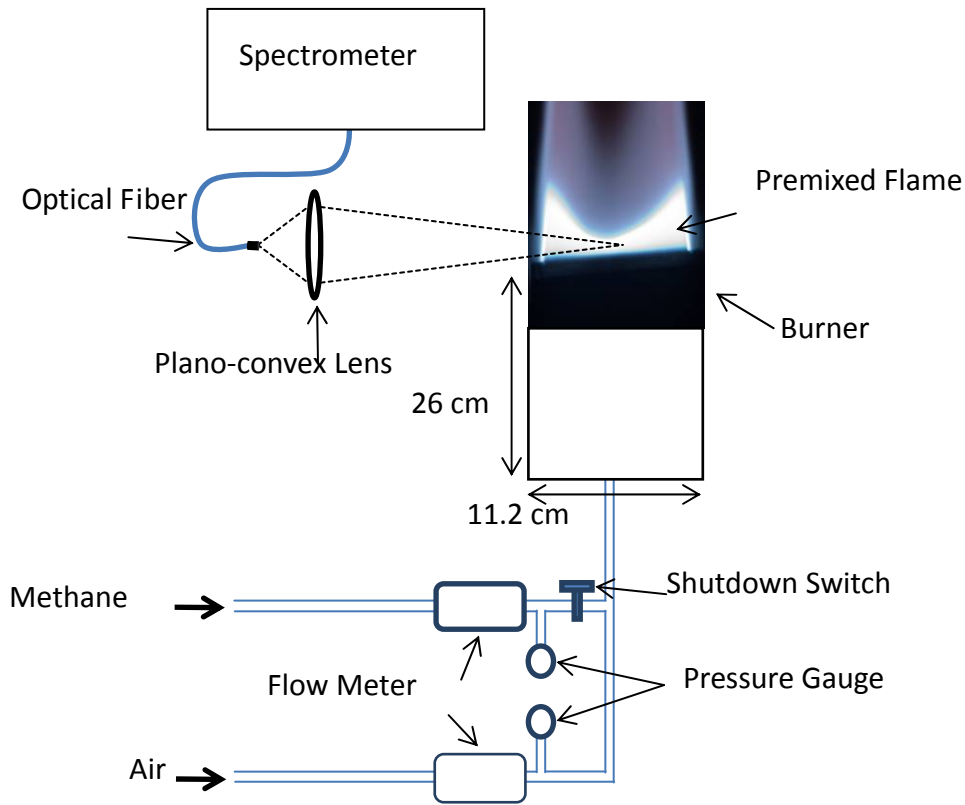


Figure 5.1

Schematic diagram of the experimental setup

Flame equivalence ratios were calculated from the volume flow rates of fuel and air measured with the rotameters and the measured air and fuel pressures ($\pm 1\%$ accuracy full scale) at the outlet of the rotameters. Both fuel and air at the rotameter outlets were assumed to be at ambient temperature (298 K) and the ideal gas equation of state was used to obtain the respective mass flow rates. The equivalence ratio was defined as follows:

$$\text{Equivalence ratio } (\phi) = \frac{AFR_s}{AFR_a} \quad (5.1)$$

where, AFR_s is the stoichiometric mass-based air-fuel ratio (17.16 for methane-air combustion), and AFR_a is the actual mass-based air-fuel ratio computed from measured fuel and air mass flow rates.

The uncertainty of the measured equivalence ratios in this study was between 3 to 5 percent. The uncertainty was estimated using the following equation [19]:

$$\frac{U_\phi^2}{\phi^2} = \left(\frac{V_f}{\phi} \frac{\partial \phi}{\partial V_f} \right)^2 \left(\frac{U_{V_f}}{V_f} \right)^2 + \left(\frac{V_a}{\phi} \frac{\partial \phi}{\partial V_a} \right)^2 \left(\frac{U_{V_a}}{V_a} \right)^2 + \left(\frac{P_f}{\phi} \frac{\partial \phi}{\partial P_f} \right)^2 \left(\frac{U_{P_f}}{P_f} \right)^2 + \left(\frac{P_a}{\phi} \frac{\partial \phi}{\partial P_a} \right)^2 \left(\frac{U_{P_a}}{P_a} \right)^2 \quad (5.2)$$

where, ϕ is equivalence ratio; V_f and V_a are fuel and air volume flow rates respectively; P_f and P_a are the pressures of fuel and air at the outlets of the respective flow meters; U_ϕ , U_{V_f} , U_{V_a} , U_{P_f} and U_{P_a} are the uncertainties associated with ϕ , V_f , V_a , P_f and P_a , respectively.

All optical measurements were performed approximately 2 mm above the burner edge. A fused silica, plano-convex, spherical lens with a 10 cm focal length and a 1.27 cm diameter focused at the center of the burner was used to collect the chemiluminescence spectra. The collected optical signal was coupled to the single end of a bifurcated optical fiber (Ocean Optics, QBIF400-UV-VIS). One of the bifurcated ends of the optical fiber was connected to an Ocean Optics USB 2000 spectrometer (600 grooves/mm grating) with a spectral resolution of 3.8 nm (full-width half-maximum) to record the chemiluminescence emission spectra. The other end was used to locate spatial position in the flame by sending a separate laser beam through it before the experimental measurements were performed. This end was closed while recording the chemiluminescence spectra. Each chemiluminescence spectrum was acquired with a 25 ms exposure time. Each recorded spectrum was an average of 20 accumulated spectra.

A total of ten such averaged spectra were recorded for each equivalence ratio condition. It is well known that the chemiluminescence emissions are superimposed on the dark current background spectrum. Hence, the dark current background was also collected for each experimental condition by blocking the natural flame chemiluminescence emissions. The experiments were replicated five times in the course of three days.

Data Analysis

Two separate analyses were performed with the recorded chemiluminescence spectra: (1) intensity ratio analysis, and (2) multivariate data analysis. A MATLAB code was written for processing the chemiluminescence data. In the first step, the dark current background was subtracted from the raw spectra and the resulting processed spectra were saved for the multivariate data analysis (described below). In the second step, the nonlinear background emissions were subtracted from the dark current background-subtracted spectra and the OH^* , CH^* , and C_2^* peak intensities were saved for the intensity ratio analysis. The following procedure was adopted for generation of the dark current nonlinear background. After selecting the 250-650 nm spectral region, the spectral peaks of OH^* , CH^* , and C_2^* were filtered from the spectrum. Using the rest of the spectrum, an n^{th} order polynomial (where n depended on the nonlinear background that varied with equivalence ratio) was generated by minimizing the root mean square (RMS) of error between the spectral intensity and the generated background.

The multivariate data analysis was performed using Unscrambler[®] version 9.7 (CAMO, Corvallis, OR, USA). A detailed method of performing multivariate data analysis can be found elsewhere [20-21]; however, a brief description of the method is

given below. Multivariate data analysis can provide important information if the variation of any analytical parameter is correlated with more than one variable. In the present case, the variation of the equivalence ratio can be correlated with the variation of spectral intensities associated with various chemical species (i.e., OH^* , CH^* , C_2^* , and CO_2^*). The key difference between the intensity ratio analysis and the multivariate data analysis lies in the inclusion of the nonlinear background (associated with CO_2^* emissions) in the latter for developing the calibration model. Therefore, multivariate data analysis, as will be shown later, can provide a more robust calibration model compared to the intensity ratio method for sensing applications. The partial least squares regression (PLS-R) approach [20] was used to develop the multivariate calibration model for prediction of equivalence ratios. The inputs to the multivariate calibration model were the chemiluminescence spectra at different equivalence ratios. The PLS-R relates variations in an analytical parameter (i.e., equivalence ratio) with variations in several explanatory variables (i.e., spectral intensities). Chemiluminescence intensities from the entire spectral range of interest (i.e., 250-650 nm) were considered as the explanatory variables. Initially, the spectral data was stored in a “X matrix” and the equivalence ratio data (calculated from the measured fuel and air mass flow rates) were stored in a “Y matrix.” In the X matrix, chemiluminescence intensities in the 250-650 nm spectral range at each equivalence ratio condition were stored in each row. Equivalence ratios were stored in the corresponding row in the Y matrix, which was essentially a column vector. The PLS-R determines the directions of maximum variations in the X matrix by simultaneously using the variations in the X and Y matrices. These directions of variations are indicated by the principal components (PCs), with the first principal

component (PC1) indicating the direction of maximum variations in the entire data set, the second principal component (PC2) indicating the next significant direction of variations, and so on. Subsequently, the spectral data were linearly regressed on the obtained PCs to develop the multivariate calibration model. While PLS-R provides a reasonable multivariate calibration with spectroscopic data, it also has a tendency toward over-fitting the available data. Therefore, it is important to analyze the “one-vector loading-weight plot” (the variation of the “loading weight” with the spectral wavelength), which is explained in “Results and Discussion” section. Additional details regarding the PLS-R approach used in the present work are available in Ref. [20].

Full cross-validation, based on the leave-one-out cross validation (LOOCV) methodology, was used to validate the calibration model. In the LOOCV method, the spectral data for one equivalence ratio was left out for validation while the rest of the spectral data set was used for developing the calibration model. This validation process (LOOCV) was then repeated for each equivalence ratio in the entire data set [20]. After the LOOCV was performed on the developed calibration model, the predictive capability of the model was further tested using an unknown data set.

Results and Discussion

In this section, the chemiluminescence spectra at different equivalence ratios and peak intensities for OH^* , CH^* , and C_2^* are discussed first. Subsequently, results from both the intensity ratio calibration model as well as the multivariate calibration model are presented and discussed. Also, the predicted equivalence ratios are compared to

measured equivalence ratios for both models and the relative benefits of the multivariate calibration model are described.

Table 5.1

List of equivalence ratios considered in the development of both the intensity ratio and the multivariate calibration models

<i>Equivalence Ratio</i>	<i>Uncertainty (\pm)</i>
0.73	0.02
0.78	0.03
0.90	0.03
0.97	0.04
1.04	0.04
1.19	0.05
1.30	0.05
1.40	0.07
1.48	0.06

For the development of both the intensity ratio and multivariate calibration models, equivalence ratios ranging from 0.73 to 1.48 were considered in this study. All equivalence ratios considered in the development of the calibration models are given in Table 5.1. The number of replications was selected after close observation of the flame chemiluminescence spectra for five days, with two recordings taken every day. A spectral range of 250-650 nm was used in this study, as the range covers most of the chemiluminescence emissions from all the species of interest. The signal-to-noise ratio (SNR) in these measurements was different for various spectral peaks at different equivalence ratios. However, the minimum SNR of the measurements was calculated by determining the SNR of the OH* peak at rich equivalence ratios (OH* will have the minimum peak intensity among all spectral peaks for CH*, OH*, and C₂* at rich

conditions). Therefore, for these measurements, the minimum SNR was determined as the ratio of the difference between the OH^* peak intensity and the background to the square root of the background. The background is determined from the average spectral intensity in the 200-250 nm range where the chemiluminescence signal is absent. For the richest equivalence ratio examined in this study ($\phi = 1.48$), the minimum SNR for the OH^* spectral peak at 309 nm (with a 25 ms exposure time and 20 spectra accumulations) was 18.

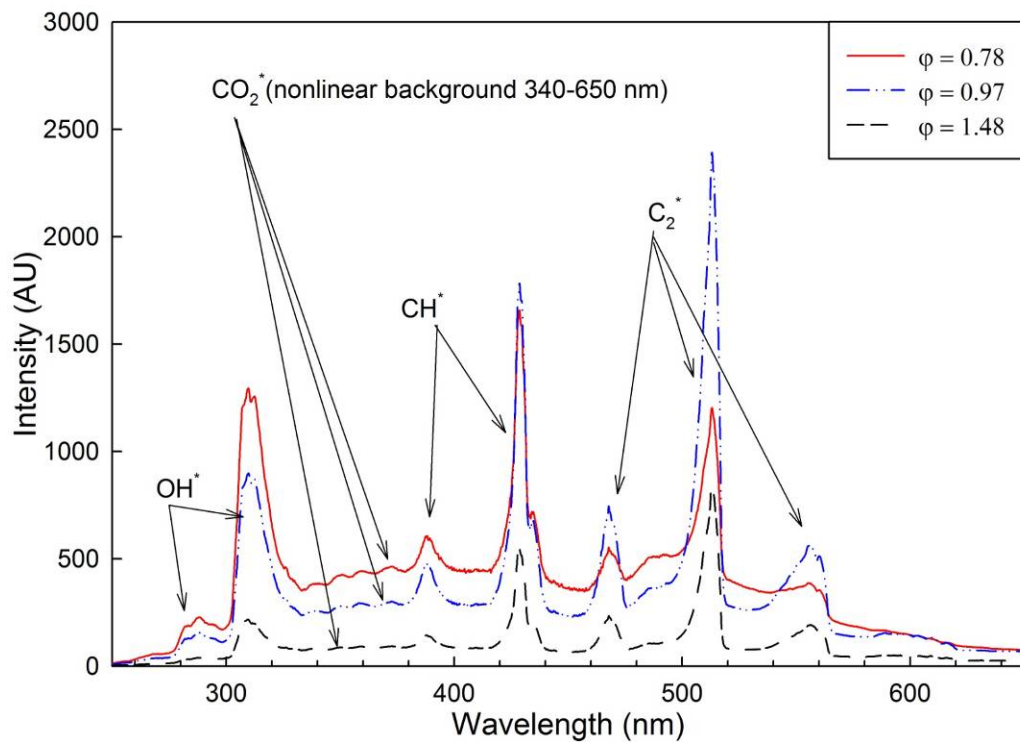


Figure 5.2

Chemiluminescence spectra of premixed atmospheric methane-air flames at different measured equivalence ratios

Figure 5.2 shows chemiluminescence spectra acquired at various equivalence ratios in the spectral range of interest. All of the three spectra shown in Figure 5.2 are plotted on the same scale. Hence, the spectral intensities can be compared directly. It can be observed from Figure 5.2 that along with the spectral peaks of OH^* , CH^* , and C_2^* , the nonlinear background (which is primarily due to CO_2^*) varied with the equivalence ratio. Particularly at $\phi = 1.48$, all the spectral peak intensities are reduced because of suppression in the nonlinear background. This can be associated with lower production of CO_2 in rich flames, where the presence of excess fuel (compared to oxidizer) favors the partial oxidation of some of the fuel into CO rather than CO_2 . These observations support the inclusion of the nonlinear background in addition to the OH^* , CH^* and C_2^* spectral peaks in the sensing of equivalence ratios, especially in rich premixed flames.

Figure 5.3 shows the variation of OH^* , CH^* , and C_2^* chemiluminescence peak intensities as the equivalence ratio was increased from a lean condition ($\phi = 0.78$) to a near-stoichiometric condition ($\phi = 0.97$), and then to a rich condition ($\phi = 1.48$). To obtain the spectral peak intensity, the nonlinear background was subtracted from the spectrum by the method described in “Data Analysis” section. It can be observed from Figure 5.3 that the OH^* peak intensity, while significantly high for lean equivalence ratios (due to the abundance of OH radicals), was relatively low in comparison to the CH^* and C_2^* chemiluminescence peak intensities for rich flames. Also, the spectral peak of C_2^* shows more variations with the equivalence ratio in comparison with OH^* , and CH^* spectral peak intensities. For example, the C_2^* peak intensities first increased when the equivalence ratio was increased from $\phi = 0.78$ to $\phi = 0.97$ but decreased to a lower value at the richest condition of $\phi = 1.48$. It is also evident from Figure 5.3 that the CH^*

spectral peak intensities showed a similar behavior with the equivalence ratio but the magnitude of the CH^* variations were much smaller than the C_2^* variations.

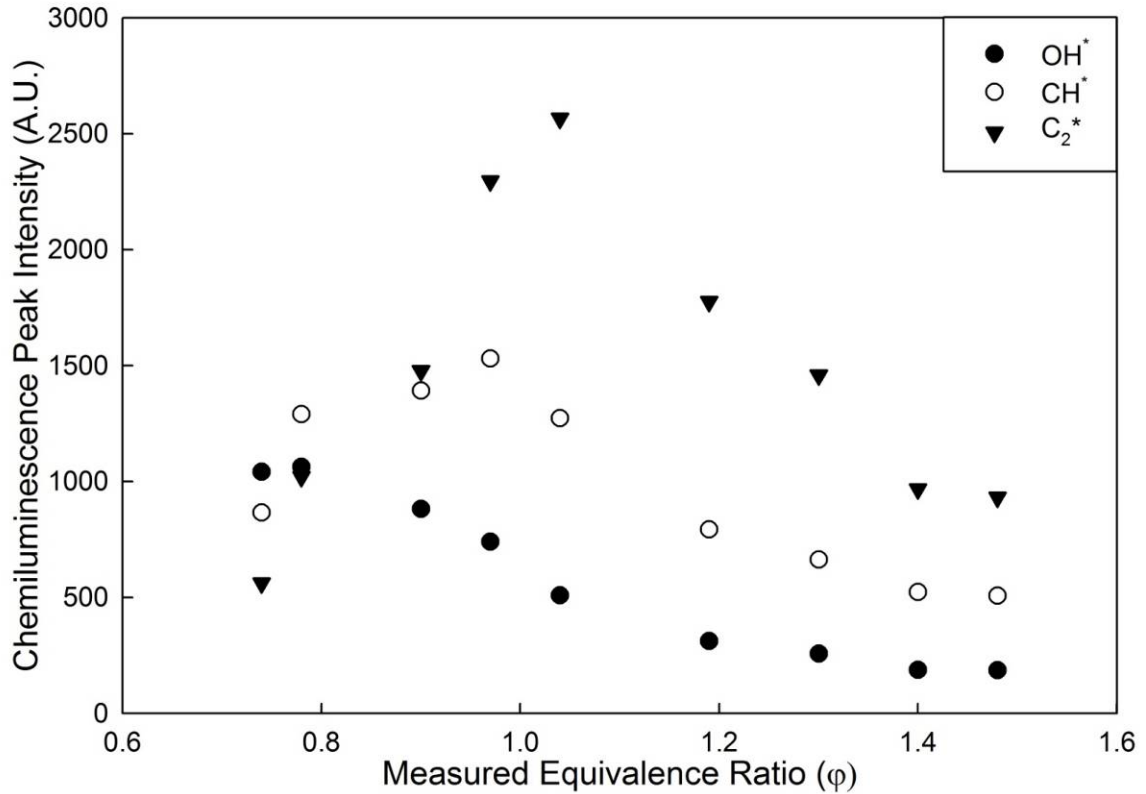


Figure 5.3

Variation of chemiluminescence peak intensities for OH^* , CH^* , and C_2^* with measured equivalence ratio

Intensity Ratio Calibration

In the literature, many researchers have employed the OH^*/CH^* peak intensity ratio as a metric for sensing equivalence ratios. As a first step in the development of the intensity ratio calibration model, the variations of the OH^*/CH^* chemiluminescence intensity ratios with the equivalence ratio are shown in Figure 5.4 along with data from

Kojima *et al.* [13], who did similar studies but used Cassegrain optics instead, for collecting the chemiluminescence spectra. As evident from Figure 5.4, the general behavior of the OH^{*}/CH^{*} data in the present work is similar to previously reported results [3, 13, 16]. However, despite the similarity of the general trends, comparison of the present data with those from Kojima *et al.* shows significant differences in the absolute magnitudes of the OH^{*}/CH^{*} intensity ratios. This can be attributed to the difference in the detection efficiencies of the spectrometers used in the present study and in the study of Kojima *et al.* Also, since Kojima *et al.* used Cassegrain optics for the collection of highly resolved optical signal with better collection efficiencies, their peak intensities could have been higher. In Figure 5.4, the increasing trend of OH^{*}/CH^{*} intensity ratio with decreasing the equivalence ratio is associated with the high OH^{*} production for lean equivalence ratios (due to excess air) [22]. The standard deviations shown with the data points for the present study were calculated based on the experimental results of five replications.

A three-parameter exponential decay curve was fitted to the calibration data. The equation of the best-fitted curve for the OH^{*}/CH^{*} intensity ratios are given below:

$$\frac{OH^*}{CH^*} = 0.37 + 594.84 \exp(-8.91\varphi) \quad (5.3)$$

As given in Figure 5.4, the R² (goodness of fit) of the fitted curve was 0.97. Root mean square error in calibration (RMSEC), which is another measure of the overall goodness of fit of the OH^{*}/CH^{*} intensity ratio calibration model, needs to be carefully studied during model development. The calculated RMSEC for the OH^{*}/CH^{*} intensity ratio analysis was 0.05. The RMSEC for any calibration model is defined below:

$$RMSEC = \sqrt{\frac{\sum_{i=1}^n (Y_i^p - Y_i^c)^2}{n}} \quad (5.4)$$

where, Y^c is the dependent variable data (intensity ratio in this case) used in the development of the calibration, Y^p is the predicted dependent variable data (again, intensity ratio here) by using the developed OH^*/CH^* intensity ratio calibration model (the exponential decay equation), and n is the number of equivalence ratios used in developing the calibration model.

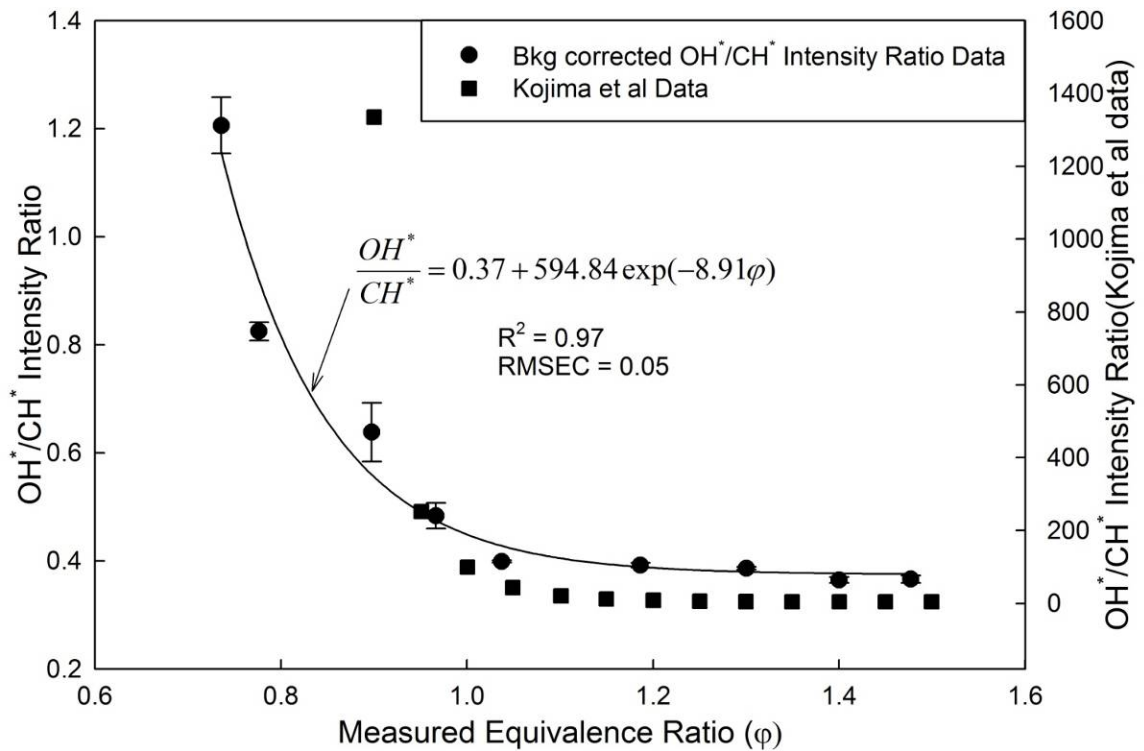


Figure 5.4

Correlation of background-corrected OH^*/CH^* intensity ratio with measured equivalence ratio

Multivariate Calibration

A PLS-R based multivariate calibration model was developed for sensing equivalence ratios in premixed methane-air flames. In this process, the multivariate model was first developed and calibrated with an initial data set consisting of chemiluminescence spectra at different equivalence ratios. Later, equivalence ratio prediction capability of the developed multivariate model was validated with an unknown spectral data set. In the model development phase, the PLS-R based regression was performed on spectra collected at nine different equivalence ratios in the range of 0.73 to 1.48 with five replications at each equivalence ratio.

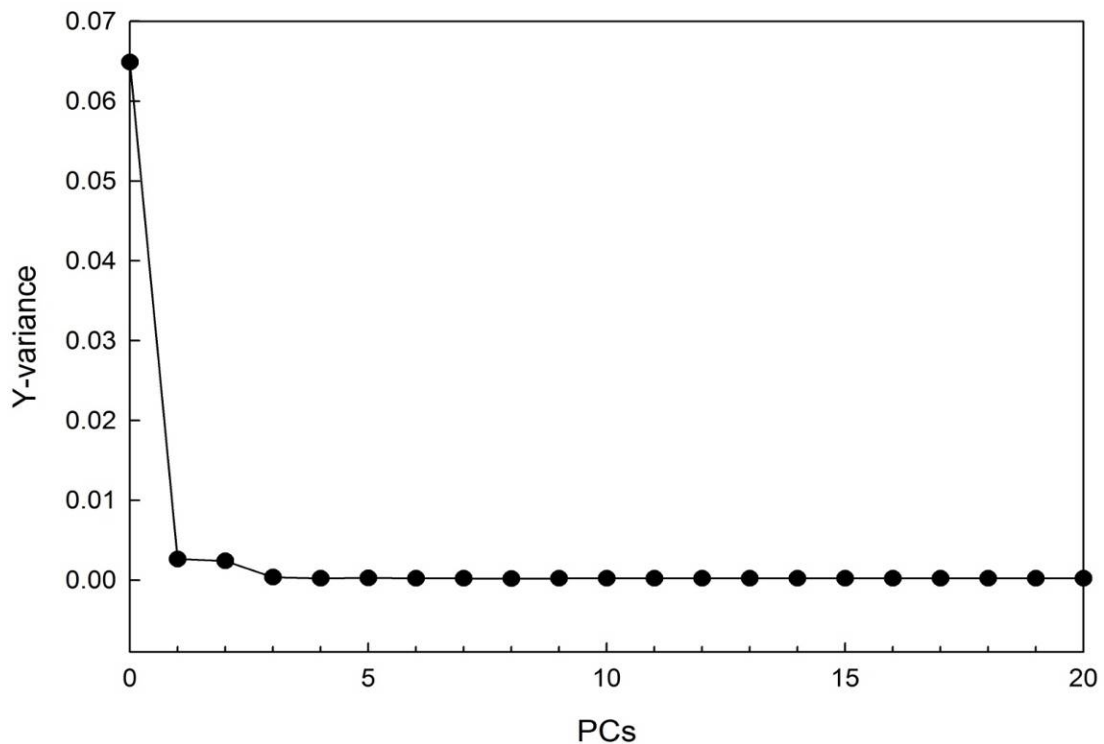


Figure 5.5

Residual validation Y-variance vs. number of principal components (PCs) used in the development of the PLS-R based multivariate calibration model

The equivalence ratios used in the development of the multivariate calibration model were calculated from measured fuel and air mass flow rates. Data from the forty-five spectra were processed for developing the multivariate calibration model. As mentioned before, a whole spectrum approach was used in developing the multivariate calibration model. In this approach, the entire spectrum in the spectral range of interest (including the nonlinear background) was used to develop the calibration model. This method helped in investigating the importance of the nonlinear background vis-à-vis the predictive capabilities of the calibration model and also to ascertain if the nonlinear background showed any variations with the equivalence ratio.

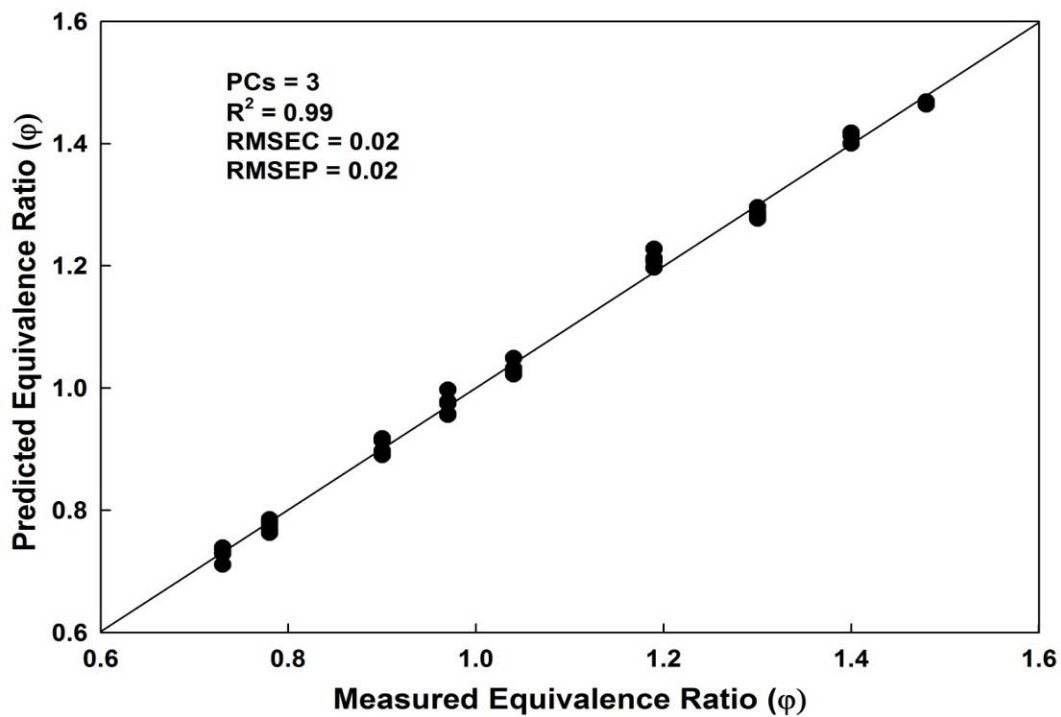


Figure 5.6

Comparison of equivalence ratios predicted with PLS-R based multivariate calibration model (using the calibration data set) and measured equivalence ratios

As discussed in “Data Analysis” section, the PLS-R determines the directions of maximum variations in the X matrix (each row of X has the spectral intensities over the entire range of wavelengths for a given equivalence ratio) by simultaneously using variations in the X and Y matrices (where the Y matrix is a column vector storing the corresponding measured equivalence ratios). Since the PCs indicate the directions of variations in the data set, the number of PCs included in the development of the multivariate calibration model is very important [20]. To understand how many PCs are needed for the development of an accurate calibration model, it is useful to examine the residual validation variance for the developed calibration model as the number of PCs used for model development is increased. The residual validation variance for Y (equivalence ratio in the present case) is a measure of how well the model will perform in predictions with a similar but unknown X-data set [20]. In other words, the smaller the residual variance, the better the model will perform in predictions with an unknown X-data set and vice versa. For the present X-data set (with LOOCV validation), the residual validation Y-variance for the PLS-R based model is shown as a function of the number of PCs in Figure 5.5. As evident from this figure, the residual variance decreases sharply as the number of PCs is increased from 0 to 3 and then remains constant (near zero) as the number of PCs is increased beyond 3 (up to a maximum of 20). Thus, Figure 5.5 clearly establishes that it is sufficient to employ only three PCs in the development of the multivariate calibration model. If additional PCs are used, then no additional benefits are realized in the calibration model. On the other hand, if four or more PCs are used in the model development for the present data set, then the model may attempt to over-fit the available X-data (and result in modeling “noise”) instead of accurately capturing the

actual variations in the X-data set; therefore, the prediction accuracy of the multivariate calibration model could potentially be compromised.

Figure 5.6 shows the predicted equivalence ratios obtained from the multivariate calibration model using the calibration data set versus the measured equivalence ratios. As mentioned above, the multivariate calibration model was developed with three PCs. In other words, the calibration model used three directions of variations in the original spectral data matrix to explain the variations of the chemiluminescence spectra with equivalence ratios. The measured equivalence ratios in Figure 5.6 refer to the equivalence ratios that were calculated from the measured fuel and air mass flow rates, i.e., the equivalence ratios in the Y-matrix. In a comparison plot such as Figure 5.6, a perfect calibration model would ensure that all of the data points in Figure 5.6 lie on the 45-degree line (i.e., predicted equivalence ratios will be exactly equal to the measured equivalence ratios at all conditions). The high R^2 value (goodness of fit) for the data points in Figure 5.6 indicates good fidelity in the multivariate calibration model. Compared to the OH^*/CH^* intensity ratio calibration ($R^2 = 0.97$), it is evident that the R^2 for the multivariate calibration model improved to 0.99. During the development of any calibration model, minimizing the RMSEC is very important [20]. Both the RMSEC and the root mean square error in prediction (RMSEP) of the multivariate calibration model (with LOOCV validation) were evaluated using an equation similar to Equation 5.4. As shown in Figure 5.6, both the RMSEC and RMSEP for the multivariate calibration model were 0.02 (which was equal to the minimum uncertainty in the equivalence ratio measurements); by comparison, the RMSEC value for the OH^*/CH^* intensity ratio calibration model was 0.05. Despite these favorable indications for the multivariate

calibration model, the final test of this model will be its ability to predict equivalence ratios in an unknown spectral data set. The outcomes of this test for both the multivariate calibration and the intensity ratio calibration are discussed in the following section.

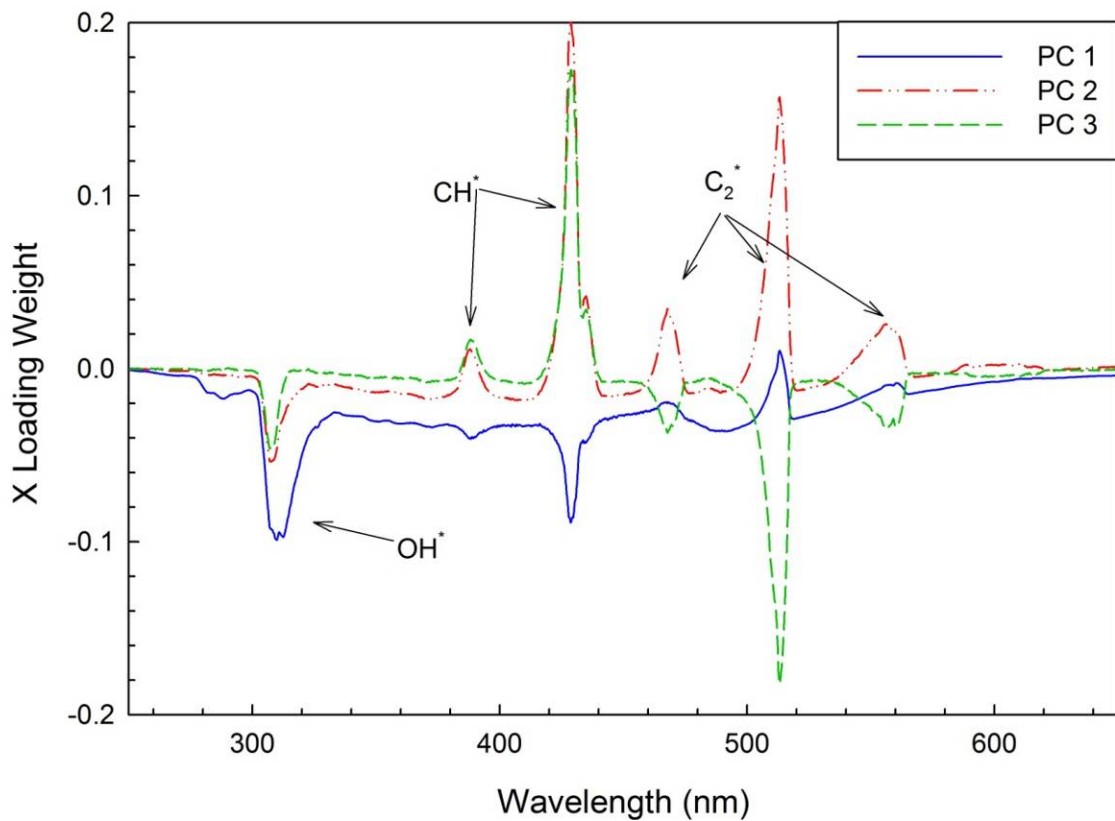


Figure 5.7

One-vector loading-weight plots along the three PCs for the developed PLS-R based multivariate calibration model

The “loading-weight” plot is another very important plot that should be analyzed while developing multivariate calibration models with spectroscopic data. The loading-weight provides information on the extent to which each explanatory variable (i.e., each spectral wavelength in the present scenario) has contributed to explaining the analytical

parameter (equivalence ratio) along each PC in the multivariate calibration model [20]. Figure 5.7 shows the variation of loading weights with wavelength along each PC (i.e., “one-vector loading-weight” plot) for the developed multivariate calibration model. Wavelengths with large (non-zero) loading-weights along a particular PC exert more influence on the developed multivariate calibration model compared to others. In other words, a PLS-R based multivariate calibration model may yield inaccurate (or even completely false) results if it does not have significant contributions from the spectral wavelengths that are known to be important in a given situation. For example, in the present case, it is well established that the spectral peak intensities of OH^* , CH^* , and C_2^* vary significantly with the equivalence ratio (see Figure 5.3); in fact, this was the foundation on which the OH^*/CH^* intensity ratio calibration discussed above was developed. Therefore, during the development of the PLS-R based multivariate calibration model, it may be expected that the one-vector loading-weight plot must show relatively large loading-weights at wavelengths corresponding to the spectral peaks of interest (OH^* , CH^* , and C_2^*). Otherwise, the developed multivariate calibration may not explain the variations in equivalence ratios correctly. In fact, it is quite evident from Figure 5.7 that, along PC1, the spectral wavelengths corresponding to OH^* , CH^* , and C_2^* show non-zero loading-weights. Moreover, the nonlinear background (especially between 300 and 500 nm) also shows non-zero loading-weights. Hence, along PC1, the spectral information from the nonlinear background (due to CO_2^* chemiluminescence emissions) as well as from the OH^* , CH^* , C_2^* chemiluminescence emissions was used to model the variations in equivalence ratios. The loading-weights along PC2 also show similar trends but with relatively larger loading-weights at wavelengths corresponding to

OH^* , CH^* , and C_2^* spectral peak intensities and lower contributions from the nonlinear background compared to PC1. Finally, along PC3, the loading-weight curve shows that only OH^* , CH^* , and C_2^* spectral peaks were used in the development of the PLS-R based multivariate calibration model, with minimal contribution from the nonlinear background. In summary, the loading-weight trends in Figure 5.7 clearly establish that while the OH^* , CH^* , and C_2^* spectral peak intensities were certainly very important contributors, the nonlinear CO_2^* background also played a non-trivial part in the development of the PLS-R based multivariate calibration model.

Prediction of Equivalence Ratios from Unknown Spectral Data Set

The predictive power of the OH^*/CH^* intensity ratio and multivariate calibration models developed in previous two sections were evaluated using an unknown, unbiased spectral data set for twenty-eight (28) different equivalence ratios between 0.71 and 1.67. This data set was taken independently after developing the two calibration models and was not used either as a training or validation data set for the LOOCV methodology used to develop the PLS-R based multivariate calibration model. The predicted equivalence ratios from the unknown unbiased spectral data are shown in Figure 5.8 for the OH^*/CH^* intensity ratio calibration model and in Figure 5.9 for the multivariate calibration model. In each of these figures, two sets of data are presented: open circles represent the equivalence ratio conditions that were included in the model development and filled circles represent the equivalence ratio conditions that were not included in model development. The 45 degree line (indicating perfect calibration) and the uncertainty bands for measured equivalence ratios are also shown in both figures. The uncertainty at

each equivalence ratio was calculated using Equation 5.2 and the errors associated with the volume flow rate and pressure measurements. Comparing figures 5.8 and 5.9, it is evident that the prediction results of the PLS-R based calibration model are better than the OH^*/CH^* intensity ratio model. The performance of the OH^*/CH^* intensity ratio model was poor especially for rich equivalence ratios and for ϕ values not used in the original calibration. The poor predictive capability of the OH^*/CH^* intensity ratio model at rich conditions was also observed by Hardalupas *et al.* in their work reported in Ref. [16]. The reasons for this trend may be associated with lower OH^* peak intensities and a relatively low change in the OH^*/CH^* intensity ratio with changing ϕ for rich flames. On the other hand, the PLS-R based multivariate calibration yielded better predictions even at rich equivalence ratios, ostensibly due to the fact that additional spectral information from other species (C_2^* and CO_2^*) were included in the development of the multivariate calibration model. Additional support for this hypothesis (i.e., improvement of multivariate PLS-R predictions due to the inclusion of C_2^* and CO_2^* spectral information) is found qualitatively in figures 5.2 and 5.3. In Figure 5.2, it can be seen that the nonlinear background (due to CO_2^* chemiluminescence) changes significantly with the equivalence ratio. For example, for $\phi = 1.48$, the nonlinear background is suppressed probably due to partial fuel oxidation, which reduces CO_2 production, and therefore, chemiluminescence emissions from CO_2^* . In addition, for rich conditions (as shown in Figure 5.3), the C_2^* spectral peaks vary more significantly with the equivalence ratio compared to the OH^* and CH^* peaks. Therefore, it may be argued that one reason for the better performance of the multivariate calibration model compared to the OH^*/CH^*

intensity ratio model may be the inclusion of the C_2^* and CO_2^* chemiluminescence in the former.

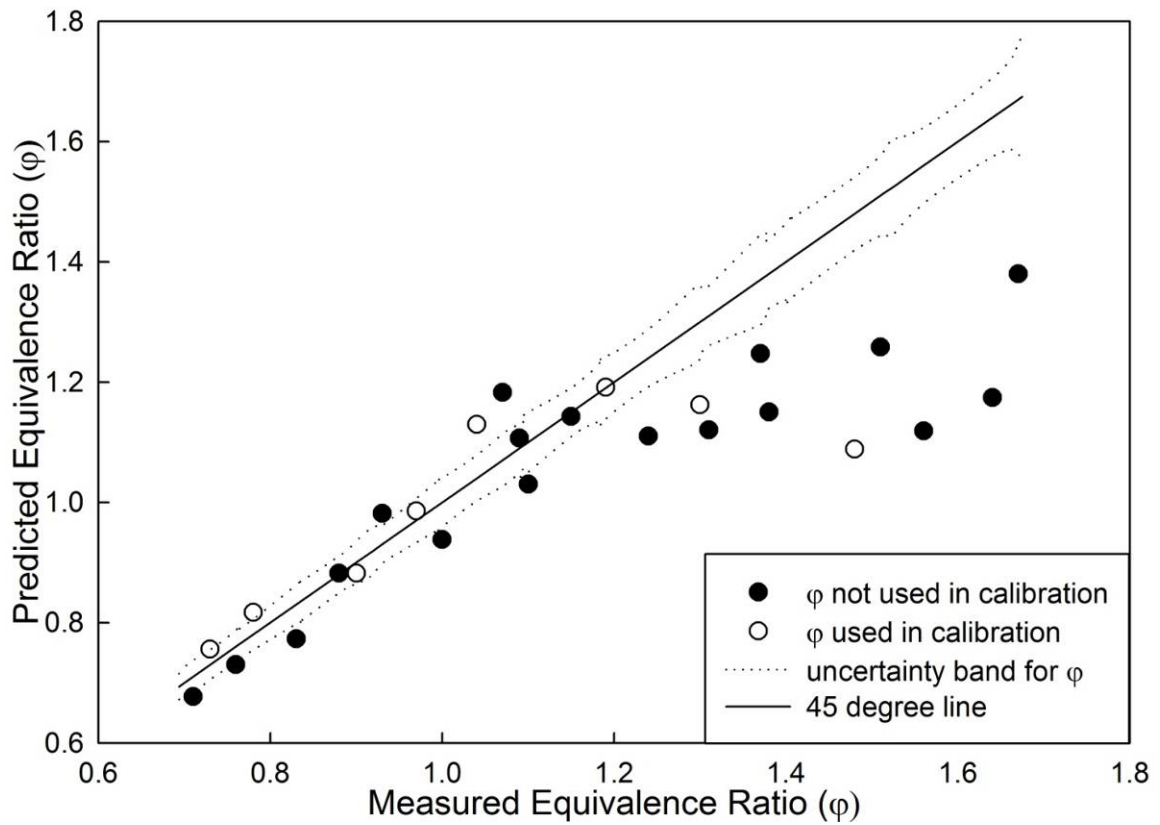


Figure 5.8

Comparison of equivalence ratios predicted using intensity ratio model (exponential decay curve from Equation 5.3) and measured equivalence ratios for an unknown data set

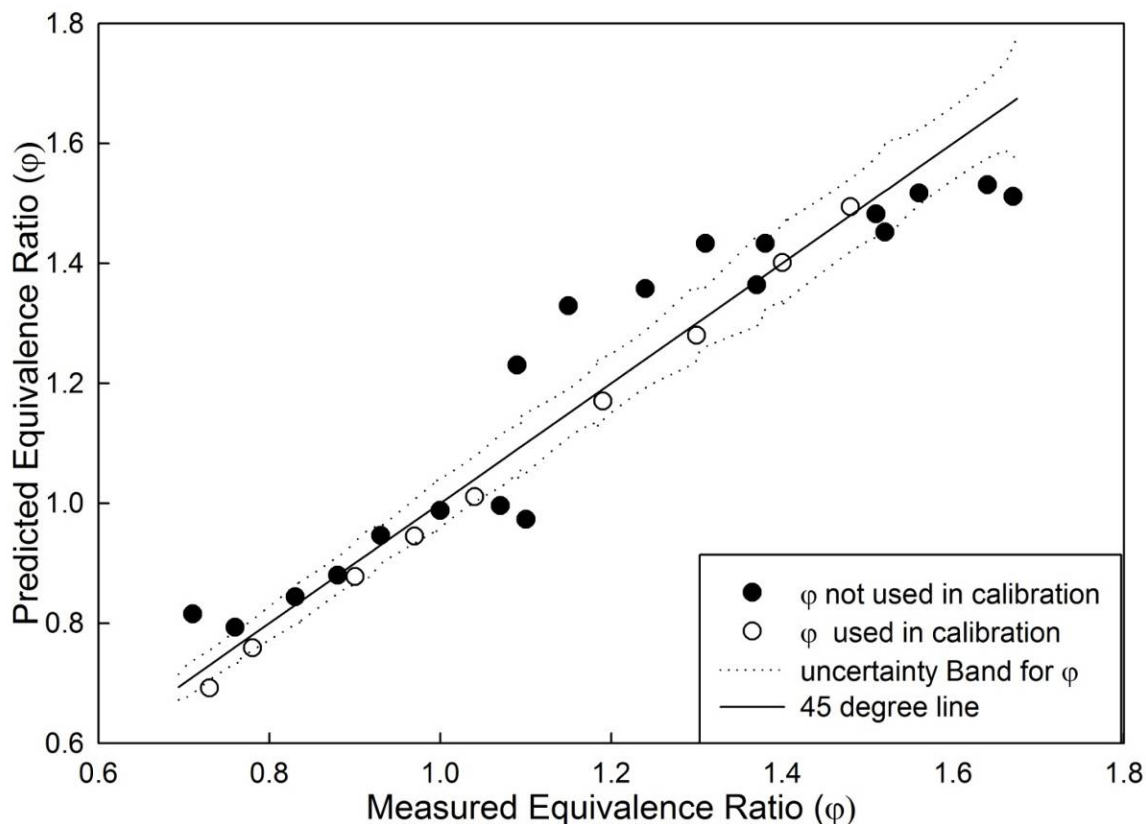


Figure 5.9

Comparison of equivalence ratios predicted using PLS-R-based multivariate calibration model and measured equivalence ratios for an unknown data set

Discussion of the Practical Implications of the Present Work

The proposed chemiluminescence-based sensing methodology has several practical advantages as well as some potential issues. A significant advantage of the multivariate calibration methodology over the OH^*/CH^* intensity ratio approach for equivalence ratio sensing is the removal of the need to perform nonlinear background subtraction from the raw measured spectra. This is especially important because nonlinear background subtraction, if performed without adequate care, could induce artificial errors in intensity ratio-based approaches. In addition, the inclusion of the

nonlinear background may actually be beneficial under some conditions for the multivariate calibration model (e.g., for rich equivalence ratios as observed in Figure 5.9). On the other hand, an obvious concern with both approaches is signal trapping, which can lead to significant errors in chemiluminescence-based equivalence ratio measurements. For example, sooty flames and other optically dense scenarios in practical combustors may impede the collection of chemiluminescence emissions, thus confounding or even completely preventing the sensing of equivalence ratios. To resolve these issues, a correction factor could be added to overcome the error introduced by signal trapping. However, in other practical combustors that encounter lean premixed flames or flameless (volumetric) combustion under low soot conditions (e.g., HCCI and lean-burn spark ignition engines), the proposed methodology may still be applied. Another difficult situation could arise in high-pressure combustion environments, as spectral peak intensities in chemiluminescence spectra are pressure-dependent [4]. Therefore, it is important to ensure that the calibration process for both the multivariate calibration model as well as the OH^*/CH^* intensity ratio calibration model is performed under practically relevant pressure conditions.

A potential benefit of the multivariate calibration methodology may be realized when sensing equivalence ratios in recirculation zones in combustors where exhaust gas may mix with the fresh fuel-air mixture or in IC engines with significant residual or recycled exhaust gas within the cylinder. Under these conditions, it may be necessary to revisit the definition of the parameter that quantifies mixture strength. The issue of redefinition of the equivalence ratio will also arise for oxygenated fuels (with oxygen atoms present in the fuel molecule), or when fuel molecules are present in the oxidizer

[23]. Instead of using the traditional “fuel-air equivalence ratio,” it may be more meaningful to define and use an oxygen-based equivalence ratio to quantify mixture strength. Nevertheless, the authors believe that the chemiluminescence-based sensing methodology could still work under these conditions. The only difference would be that instead of using the traditional equivalence ratio to “calibrate” the multivariate calibration model, the variations in the spectral data associated with variations in the new quantity that characterizes mixture strength (e.g., oxygen-based equivalence ratio or fuel-oxygen ratio) should be used. In this manner, any other quantity (similar to the equivalence ratio) can be predicted (after careful initial calibrations) using the multivariate data analysis methodology presented in this paper. Finally, the output from chemiluminescence-based sensors will also vary with variations in operating conditions of practical combustors. This must be considered carefully during the calibration process. Also, the calibration data set must include as wide a range of practically relevant operating conditions as possible.

Conclusions

Real time measurement of local fuel-air equivalence ratios (ϕ) can be helpful in monitoring pollutant formation in premixed combustors, in prevention of damages to combustors, and in the development of advanced combustion strategies, amongst other applications. In the present paper, a new partial least squares regression (PLS-R) based multivariate sensing methodology was investigated and compared with an OH^*/CH^* intensity ratio-based calibration model for sensing the equivalence ratio in atmospheric methane-air premixed flames, ranging from fuel-lean to fuel-rich conditions. Five

replications of spectral data at nine different equivalence ratios ranging from 0.73 to 1.48 were used in the calibration of both models. An unbiased spectral data set (not used in the PLS-R model development), for 28 different equivalence ratio conditions ranging from 0.71 to 1.67, was used to predict equivalence ratios using the PLS-R and the intensity ratio calibration models. The major experimental results presented in this paper can be summarized as follows:

- Since the PLS-R model used raw spectral intensities from the entire spectrum, it did not need subtraction of the nonlinear background CO_2^* emission, which was required in the OH^*/CH^* intensity ratio calibration model to obtain OH^* and CH^* spectral peak intensities.
- The PLS-R based multivariate calibration model ensured a better calibration of the original spectral data set compared to the OH^*/CH^* intensity ratio calibration model with an improved R^2 value (0.97 to 0.99) and lower root mean square error in calibration (0.05 to 0.02).
- The OH^*/CH^* intensity ratio calibration model grossly under-predicted equivalence ratios in the unknown spectral data set compared to measured equivalence ratios, especially under rich conditions ($\phi > 1.2$). By comparison, the PLS-R based multivariate calibration model performed better in predicting equivalence ratios (to within 7 percent of measurements) from the unknown spectral data set.

These results demonstrate a proof-of-concept for the development of multivariate sensing strategies for monitoring and/or control of equivalence ratios in practical combustors. Further studies are required to evaluate the performance of the multivariate calibration model in high-pressure environments and for premixed flames with other

fuels. Finally, the multivariate measurement methodology needs to be demonstrated and validated in practical premixed combustors.

Acknowledgments

This material is based upon work performed through the Sustainable Energy Research Center at Mississippi State University and is supported by the Department of Energy under Award Number DE-FG3606GO86025.

References

- [1] Docquier N, and Candel S. Combustion control and sensors: a review. *Progress in Energy and Combustion Science* 2002; 28:107-150.
- [2] Hardalupas Y, and Orain M. Local measurements of the time-dependent heat release rate and equivalence ratio using chemiluminescent emission from a flame. *Combustion and Flame* 2004; 139:188-207.
- [3] Muruganandam TM, Kim BH, Morrell MR, Nori V, Patel M, Romig BW, and Seitzman JM. Optical equivalence ratio sensors for gas turbine combustors. *Proceedings of the Combustion Institute* 2005; 30:1601-1609.
- [4] Docquier N, Lacas F, and Candel S. Closed-loop equivalence ratio control of premixed combustors using spectrally resolved chemiluminescence measurements. *Proceedings of the Combustion Institute* 2002; 29:139-145.
- [5] Zhao F, Asmus TM, Assanis DN, Dec JE, Eng JA, and Najt PM. Homogeneous charge compression ignition (HCCI) engines: Key Research and Development Issues, SAE International; 2003. PT-94, ISBN 0-7680-1123-x
- [6] Musculus MPB. Multiple simultaneous optical diagnostic imaging of early-injection low-temperature combustion in a heavy-duty diesel engine. SAE paper 2006-01-0079.
- [7] Zhao F, Lai MC, and Harrington DL. Automotive spark-ignited direct-injection gasoline engines. *Progress in Energy and Combustion Science* 1999; 25:437-562.
- [8] Kojima J, Ikeda Y, and Nakajima T. Basic aspects of OH(A), CH(A), and C₂(d) chemiluminescence in the reaction zone of laminar methane-air premixed flames. *Combustion and Flame* 2005; 140:34-45.
- [9] Ikeda Y, Kojima J, and Hashimoto H. Local chemiluminescence spectra measurements in a high-pressure laminar methane/air premixed flame. *Proceedings of the Combustion Institute* 2002; 29:1495-1501.
- [10] Jeong YK, Jeon CH, and Chang YJ. Evaluation of the equivalence ratio of the reacting mixture using intensity ratio of chemiluminescence in laminar partially premixed CH₄-air flames. *Experimental Thermal and Fluid Science* 2006; 30: 663-673.
- [11] Docquier N, Belhafaoui S, Lacas F, Darabiha N, and Rolon C. Experimental and numerical study of chemiluminescence in methane/air high-pressure flames for active control applications. *Proceedings of the Combustion Institute* 2000; 28: 1765-1774.

- [12] Morrell MR, Seitzman JM, Wilensky M, Lubarsky E, Lee J, and Zinn B. Interpretation of optical emissions for sensors in liquid fueled combustors. AIAA 2001-0787.
- [13] Kojima J, Ikeda Y, and Nakajima T. Spatially resolved measurement of OH*, CH*, and C₂* chemiluminescence in the reaction zone of laminar methane/air premixed flames. Proceedings of the Combustion Institute 2000; 28:1757-1764.
- [14] Orain M, and Hardalupas Y. Effect of fuel type on equivalence ratio measurements using chemiluminescence in premixed flames. Comptes Rendus Mecanique 2010; 338:241-254.
- [15] Ballester J, and Garcia-Armingol T. Diagnostic techniques for the monitoring and control of practical flames. Progress in Energy and Combustion Science 2010; 36:375-411.
- [16] Hardalupas Y, Orain M, Panoutsos CS, Taylor AMKP, Olofsson J, Seyfried H, Richter M, Hult J, Alden M, Hermann F, and Klingmann J. Chemiluminescence sensor for local equivalence ratio of reacting mixtures of fuel and air (FLAMESEEK). Applied Thermal Engineering 2004; 24:1619-1632.
- [17] Kalogirou SA. Artificial intelligence for the modeling and control of combustion processes: a review. Progress in Energy and Combustion Science 2003; 29:515-566.
- [18] Ballester J, Hernandez R, Sanz A, Smolarz A, Barroso J, and Pina A. Chemiluminescence monitoring in premixed flames of natural gas and its blends with hydrogen. Proceedings of the Combustion Institute 2009; 32:2983-2991.
- [19] Coleman HW, and Steele Jr. WG. Experimentation and Uncertainty Analysis for Engineers 2nd ed. John Wiley & Sons; 1999.
- [20] Esbensen KH. Multivariate Data Analysis -in Practice. 5th ed. Camo Inc; 2004.
- [21] Tripathi MM, Hassan EM, Yueh F, Singh JP, Steele PH, and Ingram Jr. LL. Reflection-absorption-based near infrared spectroscopy for predicting water content in bio-oil. Sensors and Actuators B: Chemical 2009; 136:20-25.
- [22] Panoutsos CS, Hardalupas Y, and Taylor AMKP. Numerical evaluation of equivalence ratio measurement using OH* and CH* chemiluminescence in premixed and non-premixed methane-air flames, Combustion and Flame 2009; 156:273-291.
- [23] Mueller, CJ. The quantification of mixture stoichiometry when fuel molecules contain oxidizer elements or oxidizer molecules contain fuel elements, SAE Paper 2005-01-3705; presented at the SAE Powertrain & Fluid Systems Conference & Exhibition, October 2005, San Antonio, TX, USA, DOI: 10.4271/2005-01-3705.

CHAPTER VI
A COMPARISON OF MULTIVARIATE LIBS AND CHEMILUMINESCENCE
BASED LOCAL EQUIVALENCE RATIO MEASUREMENTS IN
METHANE-AIR PREMIXED FLAMES*

Abstract

In the present work, a comparative study of fuel-air equivalence ratio measurements in atmospheric, premixed methane-air flames with ungated laser-induced breakdown spectroscopy (LIBS) and natural chemiluminescence emission spectroscopy is presented. With ungated LIBS, the strong elastically scattered laser light greatly reduces the measurement dynamic range and sensitivity. For effectively suppressing the elastically scattered laser light in ungated LIBS detection, a polarizer and a notch filter in the signal collection system were tested. It was observed that a polarizer performed better compared to a notch filter in suppressing the elastically scattered laser light. The LIBS spectra collected at ten different equivalence ratios ranging from 0.74 to 1.42 were

* Note: Most of the content of this chapter is based on an article written by author and co-workers,

Markandey M. Tripathi, Kalyan K. Srinivasan, Sundar R. Krishnan, Fang-Yu Yueh, and Jagdish P. Singh, A comparison of multivariate LIBS and chemiluminescence based local equivalence ratio measurements in methane-air premixed flames, which is currently under review to be published in Fuel journal.

used to develop the equivalence ratio calibration model using atomic line intensity ratios as well as broad spectral features with a partial least squares regression (PLS-R) approach. The developed calibration models were tested with an unknown data set comprising LIBS spectra taken at similar experimental conditions at all the equivalence ratio conditions used in developing the calibration model. The LIBS-based prediction results were also compared with the chemiluminescence-based predictions from the same experimental setup. It was found that the LIBS-based calibration provides better predictions of equivalence ratios compared to the chemiluminescence-based calibration.

Introduction

Laser-induced breakdown spectroscopy (LIBS) is an analytical method in which a high energy laser pulse is tightly focused on a small area of a sample, measuring a few microns in diameter. The high irradiance (\sim Gigawatt/cm²) imposed by the laser radiation results breakdown in the sample. The resulting plasma from the breakdown contains the spectral information of the constituent elements. This spectral information can be utilized to probe the elemental composition of a wide variety of samples. A detailed discussion on LIBS can be found elsewhere [1, 2]. In species concentration measurement, the advantage of using LIBS over some other commonly available techniques (such as Raman, fluorescence spectroscopy, etc.) include high detection efficiency and multispecies measurement. For instance, Kiefer *et al.* have reported weak Raman signal while measuring local fuel concentration for mixture formation diagnostics [3]. Fluorescence spectroscopy based species measurement requires a species-specific excitation source [4].

In recent years, LIBS has expanded its horizon to the field of combustion diagnostics [5-8]. Most of the LIBS-based combustion diagnostic studies are focused on fuel-air equivalence ratio measurements in premixed combustion systems. For example, Michalakou *et al.* have employed LIBS to determine equivalence ratios in three different methane-, ethylene-, and propane-air mixtures. [9]. It was observed that the atomic line intensity ratios $H_{656.3 \text{ nm}}/O_{777 \text{ nm}}$ and $C_{833.5 \text{ nm}}/O_{844.6 \text{ nm}}$ in the LIBS spectra from Bunsen burner laminar flames showed very good correlations with equivalence ratio. Joshi *et al.* have reported LIBS for in-cylinder equivalence ratio measurements in laser-ignited natural gas engines [10]. They employed a 1064 nm Nd:YAG laser as an optical spark plug to initiate combustion in a single cylinder natural gas engine and the optical emission in the plasma produced during combustion initiation was analyzed. A good correlation between line area ratios $H_{656.3 \text{ nm}}/O_{777 \text{ nm}}$, $H_{656.3 \text{ nm}}/N_{746 \text{ nm}}$, and $H_{656.3 \text{ nm}}/N_{(746 \text{ nm}+744 \text{ nm}+742 \text{ nm})}$ was observed with equivalence ratios measured by a wide band universal exhaust gas oxygen (UEGO) sensor. Ferioli *et al.* have reported application of LIBS for equivalence ratio measurement in spark ignited engines running under laboratory conditions [11]. It was shown that spectral features $C_{711.3 \text{ nm}}$, $O_{776.6 \text{ nm}}$, $N_{746.3 \text{ nm}}$, $N_{743.8 \text{ nm}}$, and broadband $CN_{707-734 \text{ nm}}$ in the LIBS emission can be utilized to quantify equivalence ratio.

In previous research efforts, most LIBS experiments have been performed in gated detection mode. The gated detection approach facilitates the introduction of a temporal delay (or the order of micro- or nanoseconds) between the laser pulse and the optical signal collection from the laser generated plasma. The continuum radiation from the plasma emission and the characteristic radiation (consist of various spectral lines)

decay at different rates. Therefore, time-gated detection avoids the initial intense continuum emission and improves the signal-to-background ratio. Also, this arrangement blocks the elastically scattered high intensity laser beam (after induced breakdown occurs) that can saturate the detector system. However, some recent research investigations have shown that ungated detection system (with an appropriate arrangement to block scattered laser light) can also be employed for LIBS measurements [12-14]. The advantage of ungated detection system is that it provides a simple, robust, and cost-effective approach for signal detection. Eseller *et al.* employed an ungated LIBS setup to measure equivalence ratio in methane-air premixed flames and demonstrated the application of LIBS in a biodiesel diffusion flame [12]. Kiefer *et al.* have employed a polarization filter along with ungated detection for the LIBS measurements [13]. They have also shown an online background signal correction scheme that can simplify LIBS data analysis. This arrangement was used to perform LIBS combustion diagnostics of methane and dimethyl ether flames [14].

This work discuss the use of a multivariate calibration of broadband LIBS spectra, obtained from premixed methane-air flames, utilizing an ungated detection system, to predict equivalence ratios. In literature, several researchers have reported that multivariate calibration of LIBS spectra provides a better calibration in comparison to intensity ratio calibration [15-17]. However, till date, multivariate calibration of LIBS spectra has not been investigated for equivalence ratio measurement. In this effort, the performance of a polarizer and a notch filter for suppressing scattered laser light for ungated LIBS detection were compared. It was observed that the polarizer provides better suppression of the elastically scattered laser light in comparison to the notch filter.

A partial least squares regression (PLS-R) based multivariate calibration was developed on the broadband LIBS spectra obtained from atmospheric methane-air premixed flames in a rectangular slot burner. Finally, the predictive power of the developed calibration model was compared with chemiluminescence based multivariate calibration model developed in our previous research work [18].

Specific Objectives

The specific objectives of the present work are

- [1] To evaluate ungated LIBS for equivalence ratio measurements in premixed atmospheric methane-air flames with two different approaches for data analysis.
- [2] To compare the equivalence ratio measurements obtained from LIBS (the intensity ratio approach and the multivariate calibration) with those based on multivariate calibration of the natural chemiluminescence emission spectra.

Experimental Setup

The experimental setup for the LIBS based equivalence ratio measurements is shown in the Figure 6.1. The LIBS measurements were performed in the methane-air premixed flame generated in a rectangular slot burner (length: 11.2 cm, width: 0.55 cm, and height: 26 cm). Methane (99.97 % pure) and air (breathing grade) were mixed at room temperature prior to introduction from the bottom end of the slot burner. The flow of methane and air was controlled with in-line flow meters (Cole Palmer rotameters,

$\pm 2\%$ accuracy full scale). A detailed description of the equivalence ratio calculation for the premixed mixture can be found in [18].

A frequency doubled Nd:YAG pulse laser (BigSky/Quantel CFR 400 10Hz, 532 nm, 180 mJ, 9-mm beam diameter) was used to create laser-induced-plasma in the methane-air premixed flame. The laser beam of 87 mJ pulse energy was focused approximately 2 mm above the burner by employing a plano-convex lens of 200 mm focal length. The LIBS signal was collected by employing the ungated detection technique. A polarizer (Karl Lambrecht Corporation, MGLS-SW-15) was employed to suppress the elastically scattered laser light. For some experiments, the polarizer was replaced with a notch filter (Kaiser Optical Systems, Inc., HSPF-532-1.5) to evaluate its performance. A fused silica, plano-convex, spherical lens with 100 mm focal length and 12.7 mm diameter collected and coupled the optical signal to the single end of a bifurcated optical fiber (Ocean Optics, QBIF400-UV-VIS). It is important to mention here that in LIBS the primary plasma at the focused spot radiates intense continuous emission in a short time. The secondary plasma, expanded from the primary plasma, radiates strong atomic emission with less background. The secondary plasma is more suitable for ungated LIBS measurements. Hence, while making LIBS measurements, the optical signal in the elliptically evolving laser-induced plasma (along the laser axis) was collected from the location that was a little offset (~ 2 mm axially) from the point at which laser-induced plasma was generated (see inset in Figure 6.1). This arrangement also helped in minimizing the presence of elastically scattered laser light in the collected signal without disturbing the LIBS measurements. One of the bifurcated ends of the optical fiber was connected to an Ocean Optics USB 2000 spectrometer (600

grooves/mm grating) with a spectral resolution of 3.8 nm (full-width half-maximum) to record the LIBS spectra. The other end was used for optical alignment in the flame by sending a separate laser beam through it before the experimental measurements were performed. This end was closed while performing LIBS experiments. At each equivalence ratio condition, 100 spectra were collected with 50 ms exposure time and single accumulation. Single accumulation implies that there was no on-board spectra accumulation by the detector, while recording the spectrum. Since the laser was pulsing at 10 Hz frequency (and hence two successive laser pulses were separated by a time difference of 100 ms), out of 100 collected spectra every other spectrum will capture the LIBS signal while the next one will collect the background. This method enables online background correction, which was also demonstrated by Kiefer *et al.* [13]. The LIBS experiments were replicated five times in the course of three days.

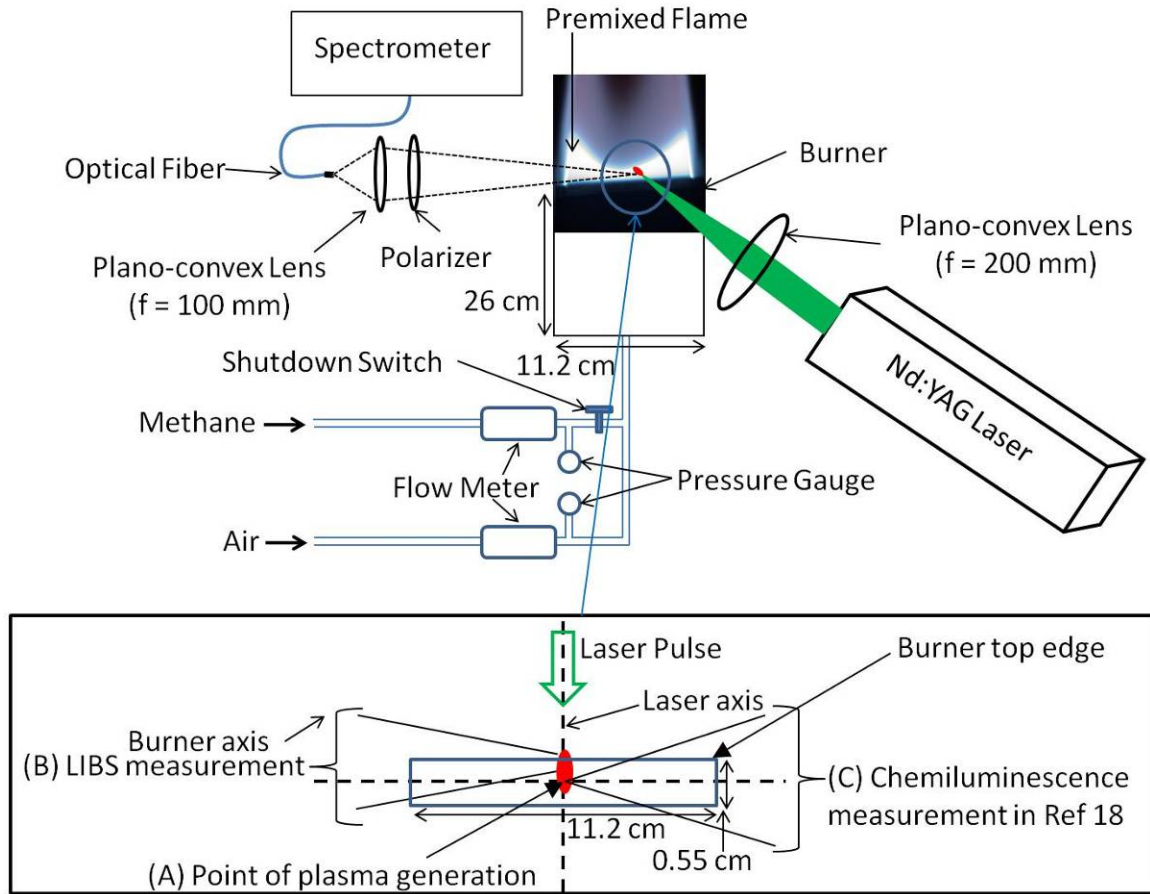


Figure 6.1

Schematic diagram of the experimental setup for LIBS based equivalence ratio measurements

Data Analysis

At each equivalence ratio condition, 100 spectra were acquired (as mentioned in the previous section). Since the laser pulses were spaced 100 ms apart and spectra were acquired every 50 ms, approximately half of the spectra were comprised of LIBS signal and half were background information. The LIBS spectra and the background spectra were separately averaged and finally the averaged background spectrum was subtracted from the averaged LIBS spectrum to generate the background-corrected LIBS spectrum.

This background-corrected LIBS spectrum was then used for the intensity ratio and the multivariate analyses.

The multivariate data analysis was performed using Unscrambler® version 9.7 (CAMO, Corvallis, OR, USA). Multivariate analysis can provide a robust calibration as variations in several spectral peaks (i.e. H_{656.3 nm}, O_{777 nm}, N_{746 nm}, N_{500 nm}, etc.) in the LIBS spectrum are correlated with the variations in equivalence ratio. A partial least squares regression (PLS-R) based multivariate calibration model was developed for equivalence ratio predictions. The inputs to the multivariate calibration model were the LIBS spectra at different equivalence ratios. Initially, all LIBS spectra in the spectral range of interest (i.e. 450-878 nm) were stored in a matrix, X. Each row of the X matrix (from first column to the last column) contains LIBS spectral peak intensities (at different wavelengths; i.e. 450-878 nm) recorded at one equivalence ratio condition. In each column (from the first row to the last row) the LIBS spectral peak intensities (at different equivalence ratios) recorded at one wavelength are stored. The equivalence ratio calculated from the measured fuel and air mass flow rates is stored in a Y matrix (which is a column vector) in such a way that the corresponding row in the X matrix contains the LIBS spectrum recorded at that equivalence ratio. The PLS-R determines the directions of maximum variations (principal components or PCs) in the X matrix by simultaneously using variations in the X and Y matrices. Subsequently, the spectral data were linearly regressed on the obtained PCs to develop the multivariate calibration model. The developed calibration model was validated by full cross-validation, based on the leave-one-out cross validation (LOOCV) methodology. A detailed description of the multivariate data analysis can be found elsewhere [18, 19].

Results and Discussion

In this section, the performance comparison of a notch filter and a polarizer for suppressing the elastically scattered laser light in ungated LIBS detection is first presented. Afterward, results from the intensity ratio calibration and the multivariate calibration are reported and discussed. The predictive capabilities of the intensity ratio calibration and the multivariate LIBS calibration were tested by employing an unknown data set. Finally, the predictions from the chemiluminescence-based multivariate calibration reported in the previous work [18] are compared with the LIBS-based prediction results.

Performance Comparison of Notch Filter and Polarizer for Ungated LIBS Detection

The laser light employed for laser-induced plasma generation in LIBS also gets elastically scattered during the process. This randomly scattered laser light (in 4π sphere) can enter and saturate the detector due to its high intensity. Since most of the LIBS spectral lines appear in ultraviolet and visible (UV-Vis) region. One option to avoid damaging the detector is by using the Nd:YAG laser emitting the laser light in the fundamental frequency of 1064 nm while setting the LIBS detector in the UV-Vis region. However, the health hazard associated with the high energy, invisible laser pulse of 1064 nm has limited its use in LIBS systems [13]. One of the most commonly used setups for LIBS detection involves a frequency-doubled Nd:YAG laser pulsing at 532 nm for laser-induced plasma generation and a gated detector system to detect temporally resolved LIBS signal from the generated plasma. In gated detection systems, a trigger pulse generated from the laser can be employed to introduce an appropriate delay (of several

micro- or nanoseconds) between the laser pulse and the LIBS signal detection in the generated plasma (the generated laser-induced plasma sustains for several μs). It has been reported that for some combustion diagnostics applications, the sophisticated and complex gated detection system can be replaced with a simple, robust, and cost-effective ungated detection system with an arrangement for suppressing elastically scattered laser light [12, 14].

In this section, the performances of the two most commonly used methods for suppressing the scattered laser light are compared (for ungated LIBS in combustion diagnostics) - a notch filter and a polarizer. The notch filter used in the work was a holographic SuperNotch-Plus™ filter (Kaiser Optical System, Inc.) with optical density attenuation > 6.0 and bandwidth < 10 nm at 532 nm wavelength and the polarizer was a Glan laser prism polarizer (Karl Lambrecht Corporation) with single escape window and 15 mm clear aperture. Figure 6.2 shows the LIBS spectra collected from a premixed methane-air flame with both arrangements. The LIBS spectrum without both arrangements was not recorded as the elastically scattered laser light would saturate the detector. It can be observed from Figure 6.2 that the polarizer performed better in suppressing the laser light. Also, the LIBS spectra with the polarizer had more spectral features (specifically at shorter wavelengths) in comparison with the LIBS spectra with the notch filter. In the laser-induced plasma, the LIBS spectra were collected from a location that was away (~ 2 mm axially) from the point of plasma generation (see inset Figure 6.1). This position was optimized while closely watching the real-time LIBS signal. This arrangement also helped in reducing the presence of scattered laser light.

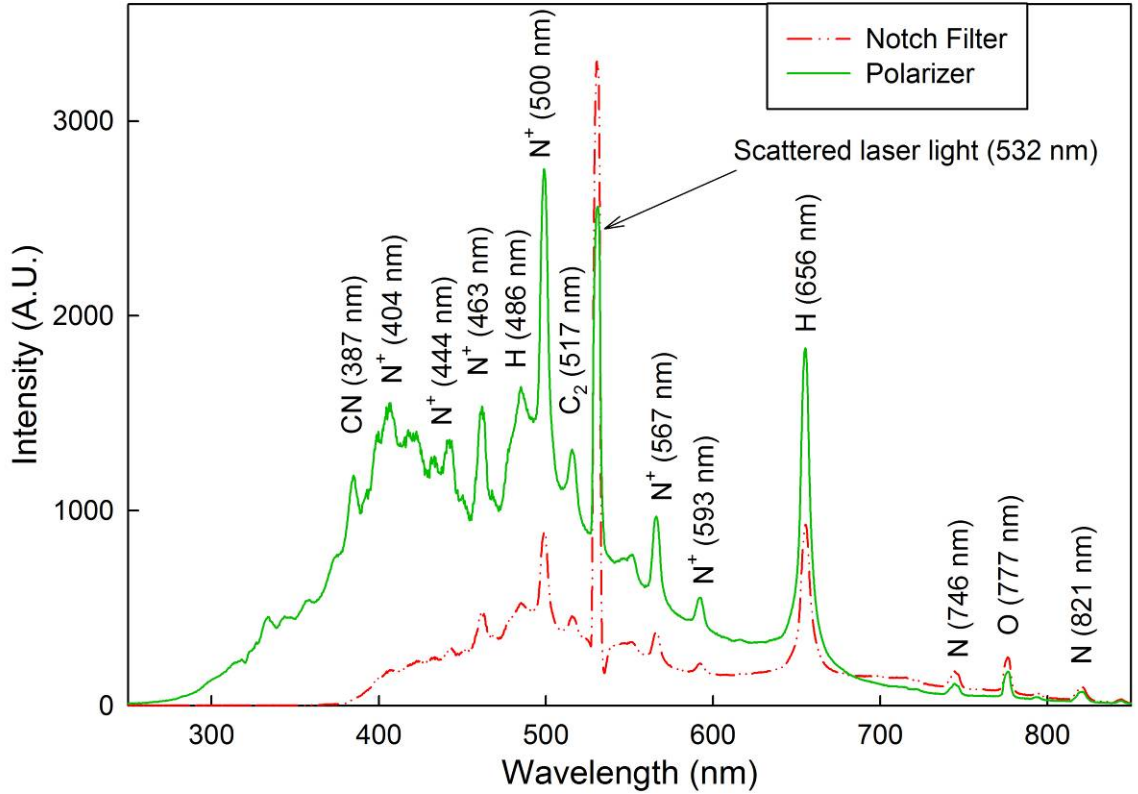


Figure 6.2

Comparison of LIBS spectra collected from methane-air premixed flame with a notch filter and a polarizer

Univariate Calibration of LIBS Spectra

The LIBS experiments were performed at 10 different equivalence ratio conditions (between 0.74-1.42) in a methane-air premixed flame. Table 6.1 summarizes the equivalence ratios calculated with the measured air and methane flow rates. The uncertainties associated with the measured equivalence ratios were calculated based on following equation [20]:

$$\frac{U_{\varphi}^2}{\varphi^2} = \left(\frac{V_f}{\varphi} \frac{\partial \varphi}{\partial V_f} \right)^2 \left(\frac{U_{V_f}}{V_f} \right)^2 + \left(\frac{V_a}{\varphi} \frac{\partial \varphi}{\partial V_a} \right)^2 \left(\frac{U_{V_a}}{V_a} \right)^2 + \left(\frac{P_f}{\varphi} \frac{\partial \varphi}{\partial P_f} \right)^2 \left(\frac{U_{P_f}}{P_f} \right)^2 + \left(\frac{P_a}{\varphi} \frac{\partial \varphi}{\partial P_a} \right)^2 \left(\frac{U_{P_a}}{P_a} \right)^2 \quad (6.1)$$

where, φ is the equivalence ratio; V_f and V_a are fuel and air volume flow rates respectively; P_f and P_a are the pressures of fuel and air at the outlets of the respective flow meters; U_φ , U_{V_f} , U_{V_a} , U_{P_f} , and U_{P_a} are the uncertainties associated with φ , V_f , V_a , P_f and P_a , respectively.

Table 6.1

Equivalence ratios considered in the LIBS experiments and the corresponding uncertainties

<i>Equivalence Ratio</i>	<i>Uncertainty (\pm)</i>
0.74	0.04
0.79	0.04
0.83	0.04
0.90	0.04
0.96	0.05
1.04	0.05
1.13	0.07
1.21	0.06
1.32	0.07
1.42	0.08

The background-corrected LIBS spectra (processed by the method described in the data analysis section) were employed for univariate calibration. A univariate calibration studies the variation of a single parameter with the property of interest. For instance, in the present case, the study of the variation in the spectral intensity of any of the hydrogen, nitrogen, or oxygen line (or their intensity ratio) with equivalence ratio, present in the LIBS spectra can be considered as univariate calibration. All spectral lines were corrected to eliminate the contribution from the continuum plasma emission. The individual peak intensity of the spectral peaks was extracted by subtracting the continuum

plasma background. The plasma background at individual spectral peaks was generated by employing the background plasma information on both sides of the individual spectral peak and by developing a two point baseline. Figure 6.3 shows the variation of the spectral peak intensities of hydrogen (656 nm), nitrogen (500 nm), and oxygen (777 nm) at different equivalence ratios. The hydrogen ($H_{656 \text{ nm}}$) and oxygen ($O_{777 \text{ nm}}$) lines were from neutral atom emission, and nitrogen line ($N^+_{500 \text{ nm}}$) corresponded to the singly ionized nitrogen atom [21]. The error bars shown with the data points represent the standard deviations in the spectral peak intensities recorded in five replications for developing the calibration model. In Figure 6.3, it can be observed that the spectral peak intensity of $N^+_{500 \text{ nm}}$, and $O_{777 \text{ nm}}$ was decreasing with an increase in the equivalence ratio. This can be explained with the fact that the increase in equivalence ratio from lean (0.74) to near-stoichiometric (0.96) and then near-stoichiometric (0.96) to rich (1.42) involves a reduction of the air mass fraction in the premixed methane-air mixture. Hence, the concentration of nitrogen and oxygen decreases (with an increase in equivalence ratio) in the laser induced plasma of methane-air premixed flames. Similarly, the concentration of methane increases with an increase in equivalence ratio from lean (0.74) to near-stoichiometric (0.96) and then near-stoichiometric (0.96) to rich (1.42) equivalence ratios. Hence, the concentration of hydrogen increases (with an increase in equivalence ratio) in the laser induced plasma of methane-air premixed flames. This can also be observed from the increase in the $H_{656 \text{ nm}}$ spectral line intensity with increase in equivalence ratio. It can also be observed that there are high standard deviations associated with the spectral peak intensities in the replicated data. The high standard deviations may arise from the minor shot-to-shot variations in the laser pulse energy. A very small change in the laser

pulse energy can alter the characteristics of the induced plasma, and thereby, the spectral peak intensity. The high standard deviations in the individual spectral peak intensities is one of the primary reasons behind the popularity of relative intensity analysis (or intensity ratio analysis) or multivariate data analysis of LIBS data among researchers.

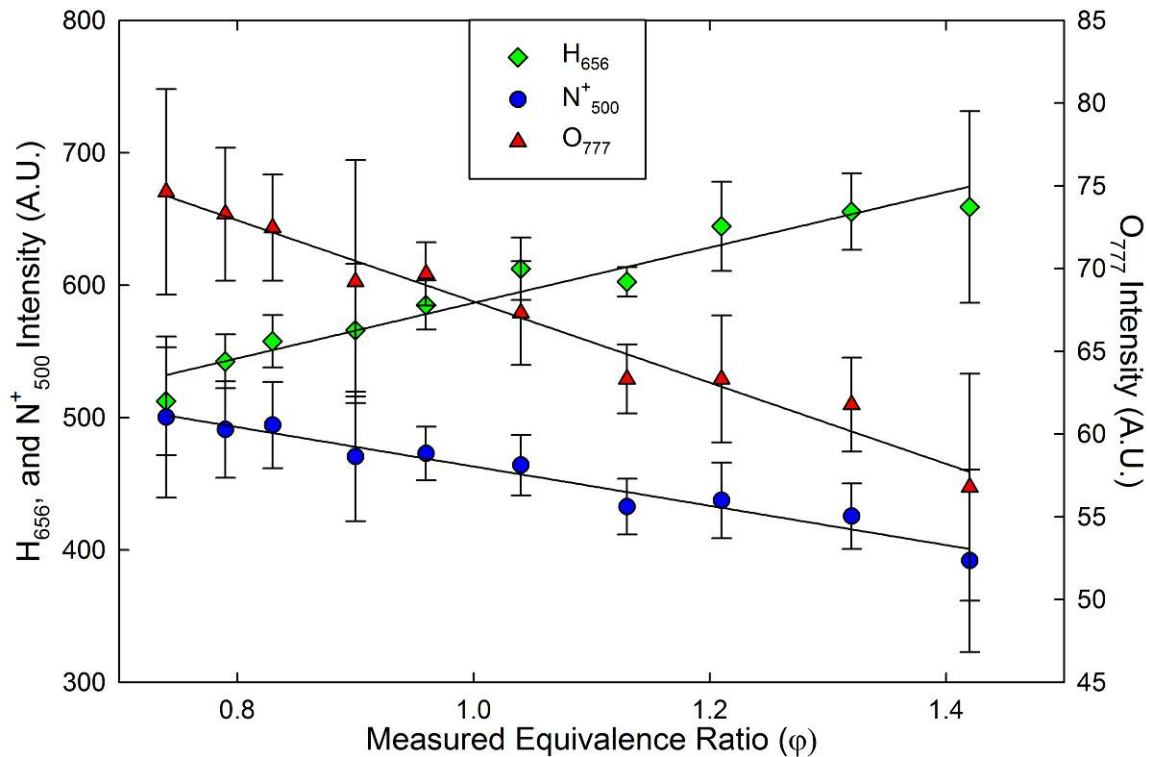


Figure 6.3

Variation of spectral peak intensities of hydrogen ($H_{656 \text{ nm}}$), nitrogen ($N_{500 \text{ nm}}^+$), and oxygen ($O_{777 \text{ nm}}$) with measured equivalence ratio in LIBS spectra

To reduce the standard deviation due to shot-to-shot fluctuations in the laser pulse energy, an intensity ratio-based calibration was developed for equivalence ratio measurement. Figure 6.4 shows the variation of the developed $H_{656 \text{ nm}}/N_{500 \text{ nm}}^+$ and $H_{656 \text{ nm}}/O_{777 \text{ nm}}$ based intensity ratio calibrations for equivalence ratio prediction. It can be

observed from Figure 6.4 that there is a significant reduction in the standard deviation in the equivalence ratios at a given equivalence ratio. For instance, in near-stoichiometric conditions (at $\phi = 0.96$), the relative standard deviations (RSD) in $H_{656 \text{ nm}}$, $N^+_{500 \text{ nm}}$, and $O_{777 \text{ nm}}$ spectral peaks were 3.17%, 4.27%, and 2.75%, respectively. However, the RSD values in $H_{656 \text{ nm}}/N^+_{500 \text{ nm}}$ and $H_{656 \text{ nm}}/O_{777 \text{ nm}}$ intensity ratios at the same equivalence ratios were 2.01% and 0.99%, respectively. The RSD value is defined as

$$RSD = \frac{\sigma_x}{\bar{X}} \quad (6.2)$$

where, σ_x is the standard deviation in the replications, and \bar{X} is the average value of the replications.

This improvement in the intensity ratio based result is mainly because the relative intensities of the spectral lines will be unaltered in the relatively weak (or strong) laser-induced plasma generated due to shot-to-shot fluctuation in the laser pulse energy. The intensity ratio of the spectral peaks will be correlated with the relative concentration of elemental composition at a given equivalence ratio condition (although, there will be some variations while repeating experiments due to uncertainties associated with equivalence ratio measurement). A linear regression was performed on both intensity ratio ($H_{656 \text{ nm}}/N^+_{500 \text{ nm}}$ and $H_{656 \text{ nm}}/O_{777 \text{ nm}}$) calibration data to obtain calibration equations. The best-fitted two-parameter linear curves to the calibration data are:

$$H_{656} / N^+_{500} = 0.3630 + 0.9201\phi \quad (6.3)$$

$$H_{656} / O_{777} = 2.1672 + 6.5678\phi \quad (6.4)$$

As given in Figure 6.4, the R^2 (goodness of fit) of both fitted curves was 0.99. However, the slope of $H_{656 \text{ nm}}/O_{777 \text{ nm}}$ intensity ratio calibration line (6.5678) is higher than $H_{656 \text{ nm}}/N^+_{500 \text{ nm}}$ intensity ratio calibration line (0.9201). Since, higher slope represents higher sensitivity of a calibration line; $H_{656 \text{ nm}}/O_{777 \text{ nm}}$ intensity ratio calibration will be more sensitive than $H_{656 \text{ nm}}/N^+_{500 \text{ nm}}$ intensity ratio calibration. The calculated RMSEC values for the $H_{656 \text{ nm}}/N^+_{500 \text{ nm}}$ and $H_{656 \text{ nm}}/O_{777 \text{ nm}}$ intensity ratio analysis were 0.02 and 0.11 respectively. The RMSEC for the calibration model was defined by:

$$RMSEC = \sqrt{\frac{\sum_{i=1}^n (Y_i^p - Y_i^c)^2}{n}} \quad (6.5)$$

Where, Y_c is the dependent variable data (intensity ratio in this case) used in the development of the calibration, Y_p is the predicted dependent variable data (again, intensity ratio here) by using the developed intensity ratio calibration model (the linear equation), and n is the number of data points (equivalence ratios, in this case) used in developing the calibration model.

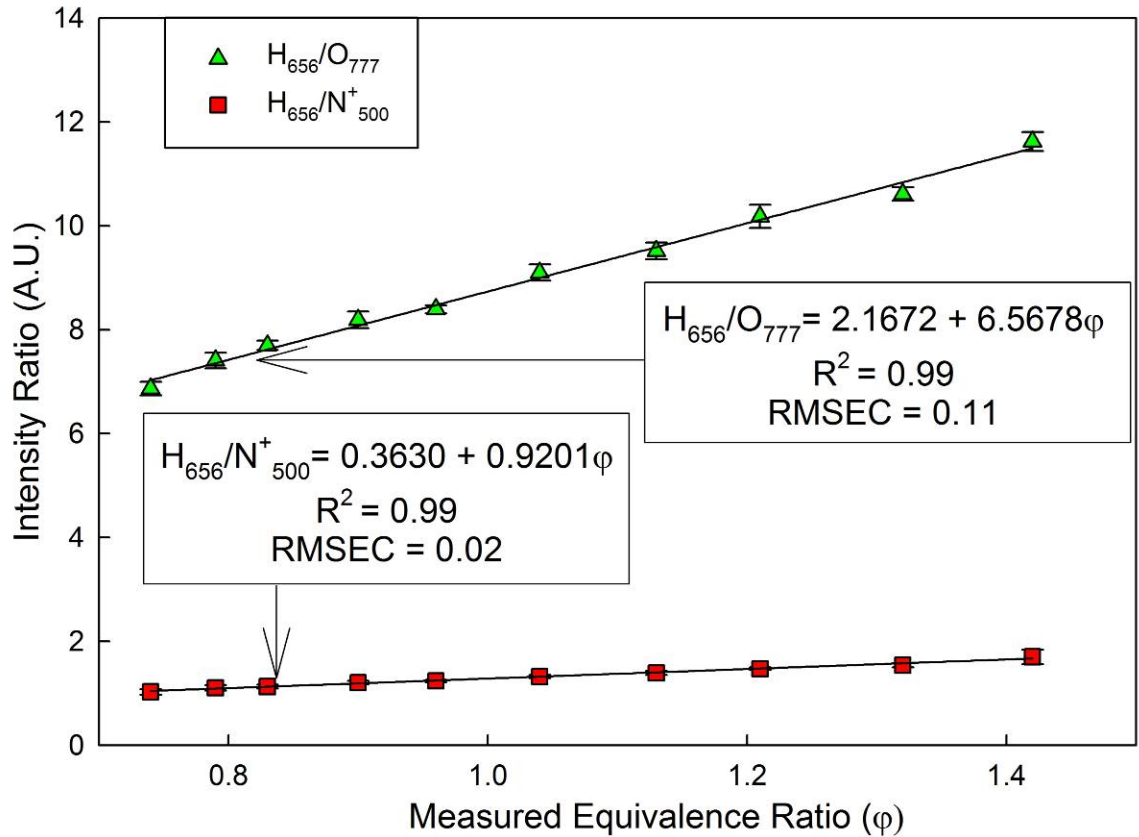


Figure 6.4

Correlation of $H_{656 \text{ nm}}/N^+_{500 \text{ nm}}$ and $H_{656 \text{ nm}}/O_{777 \text{ nm}}$ intensity ratios with measured equivalence ratio

Multivariate Calibration of LIBS spectra

A PLS-R based multivariate calibration was also developed from the LIBS spectra obtained from premixed methane-air flames. In this process, the multivariate calibration was developed with a data set consisting of LIBS spectra at ten different equivalence ratios in the range of 0.74 to 1.42 with five replications at each equivalence ratio. In the model development phase, the PLS-R based regression was performed on the spectral data, which was then validated with the leave-one-out cross validation (LOOCV) approach. Later, the predictive capability of the developed calibration was

compared with the intensity ratio calibration by predicting equivalence ratios from an unknown spectral data set.

The reference (or true) value of the equivalence ratio for calibration development was obtained from the measured methane and air flow rates. Data from fifty spectra (five at each equivalence ratio for ten different equivalence ratios) were processed for the development of the multivariate calibration. Various spectral ranges were tested for developing the optimal multivariate calibration with high R^2 and low RMSEC. It was observed that the whole LIBS spectrum in the spectral range of 450-878 nm could provide the best calibration model for equivalence ratio predictions. This spectral range contains most of the spectral features of the LIBS spectra from premixed methane-air flames. An important step while developing the multivariate calibration (with ungated LIBS data) was to eliminate the spectral contribution of laser light in the LIBS spectra prior to developing the calibration model. The inclusion of the random laser spectral intensities during calibration development may lead to an overfitted (or false) calibration. Hence, spectral intensities in the 526-536 nm range in the LIBS spectra were ignored while developing the multivariate calibration.

The PLS-R based multivariate calibration initially determines the direction of maximum variance (or principal components, PCs) in the spectral data (or X matrix in which LIBS spectral intensities at a given equivalence ratio were stored in each row for the entire wavelength range of interest) by simultaneously using variations in spectral data and equivalence ratios (or Y matrix which is a column vector storing measured equivalence ratios corresponding to each row of the X matrix). The spectral data were then linearly regressed on the obtained PCs to develop the calibration model [19]. Hence,

the number of PCs included in developing the multivariate calibration must be optimized. The decision on the inclusion of a certain number of PCs in a multivariate calibration model can be made by the study of the residual validation variance with PCs for the developed calibration model [19]. In the present case, the residual validation variance is a measure of how well the model will perform while predicting equivalence ratios with an unknown LIBS spectrum. A detailed discussion on the residual validation variance can be found elsewhere [18, 19]. Figure 6.5 shows the variation of residual validation Y-variance with the number of PCs for the developed calibration model. Again model was validated with LOOCV. It can be clearly observed from Figure 6.5 that the residual validation variance remains nearly constant (close to zero) after PC_03. Hence, Figure 6.5 clearly suggests that 3 PCs will be sufficient for the development of the calibration model. In the present work, up to 8 PCs were tested while developing the calibration model. An inclusion of higher number of PCs (beyond 3) may lead towards over-fitting the spectral data, and, therefore, can affect the prediction accuracies while employing the calibration model to an unknown data set.

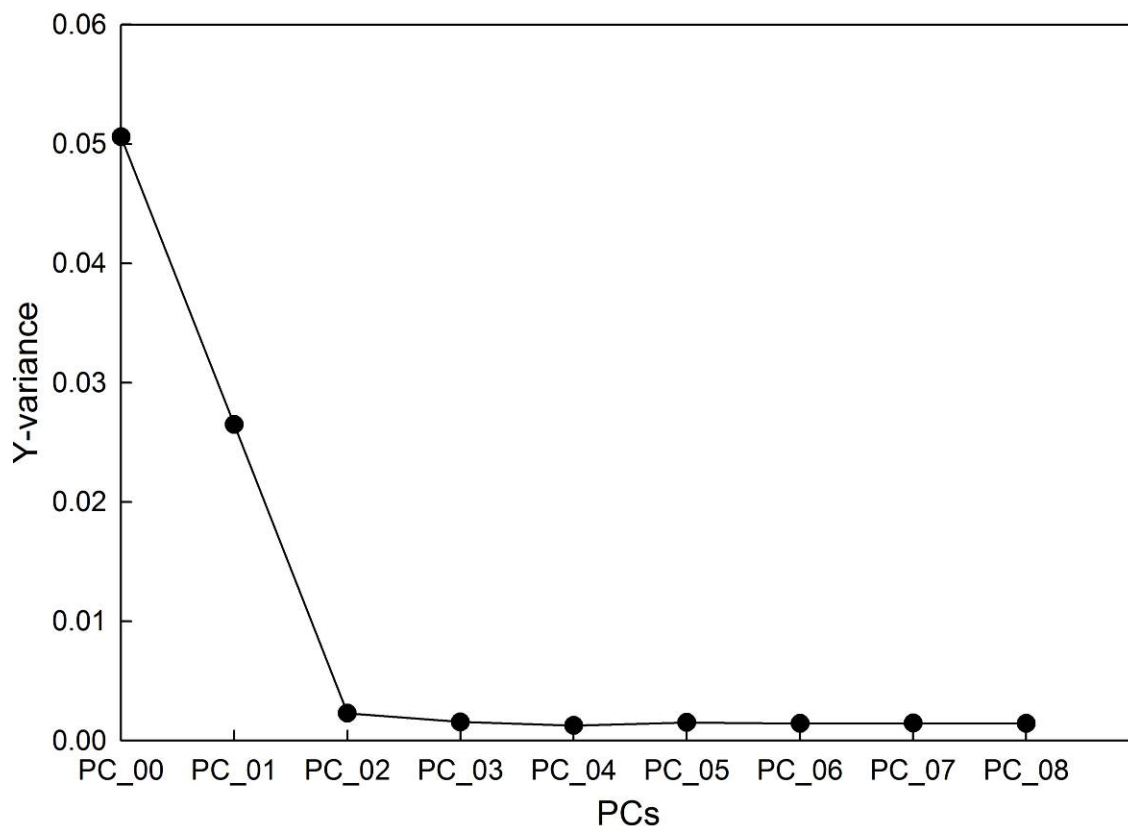


Figure 6.5

Residual validation Y-variance vs. number of principal components (PCs) used in the development of the PLS-R based multivariate calibration on LIBS spectra

Figure 6.6 shows predicted equivalence ratios obtained from the multivariate calibration model using the calibration data set. These predictions are based on LOOCV while validating the developed calibration model. This model employed three PCs (or three directions of variation in the spectral data X matrix) to explain the variations in LIBS data with equivalence ratios. The equivalence ratios in the Y matrix (calculated with measured methane and air flow rates) were considered reference values (referred to as measured equivalence ratios in Figure 6.6). It can be observed that the R^2 (goodness of fit) for multivariate calibration was a little low (0.98) in comparison to both H_{656}

nm/N⁺_{500 nm} ($R^2 = 0.99$) and H_{656 nm}/O_{777 nm} ($R^2 = 0.99$) intensity ratio calibrations. However, RMSEC improved to 0.04 compared to H_{656 nm}/O_{777 nm} (RMSEC = 0.11) intensity ratio calibration. However, RMSEC value was a little higher compared to H_{656 nm}/N⁺_{500 nm} (RMSEC = 0.02). Despite the slight increase in the RMSEC in comparison to H_{656 nm}/N⁺_{500 nm}, the difference was insignificant as the minimum uncertainty in the measured equivalence ratio was 0.04 (see Table 6.1). The root mean square error in prediction (RMSEP) was also 0.04. Both the RMSEC and the root mean square error in prediction (RMSEP) of the multivariate calibration model (with LOOCV validation) were evaluated using an equation similar to Equation 6.5.

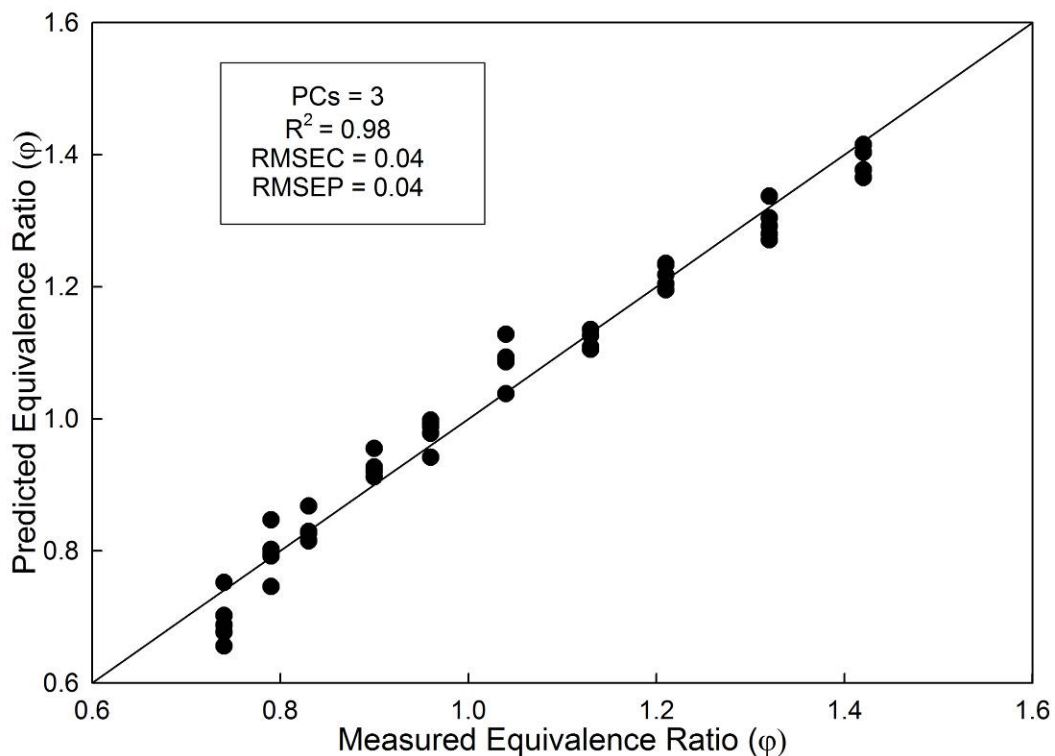


Figure 6.6

PLS-R based prediction of equivalence ratios while validating the developed multivariate calibration model with LOOCV (using the calibration data set)

Figure 6.7 shows one-vector loading-weight plots for the developed multivariate calibration model on LIBS spectra. The loading-weight provides information on the extent to which each spectral wavelength (explanatory variable) has contributed in explaining variation in equivalence ratio (analytical parameter) along each PC in the multivariate calibration model [19]. Wavelengths with large (non-zero) loading-weights along a particular PC exert more influence on the developed multivariate calibration model compared to others. The study of the loading weight plot is very important to understand the specific contribution of spectral wavelengths (i.e., the wavelengths that are expected or not expected to contribute in the development of the calibration model; otherwise, PLS-R based multivariate calibration model may yield inaccurate or false results). For instance in the present study, the recorded LIBS spectrum also contains spectral intensities from the scattered laser light and it is reasonable to expect the multivariate calibration model not to include spectral intensities from the scattered laser light. However, while studying the loading weight plot of the calibration developed with the full spectrum, it was observed that the calibration model was over fitting the spectral data by including the contribution from the 532 nm scattered laser intensities. The study of the loading weight plot helped in the decision to ignore the 526-536 nm spectral range during the development of calibration model to avoid over fitting in the spectral data. The loading plot shown in Figure 6.7 is from the reduced spectral range 450-878 nm (while ignoring the 526-536 nm spectral range) that provided the optimal calibration result. From Figure 6.7, it is evident that most of the wavelengths that correspond to hydrogen, oxygen, and nitrogen spectral emissions have contributed in the development of the calibration model. In the next section, the predictive power of the multivariate

calibration model is compared with that of the intensity ratio based calibration by testing it with an unknown data set.

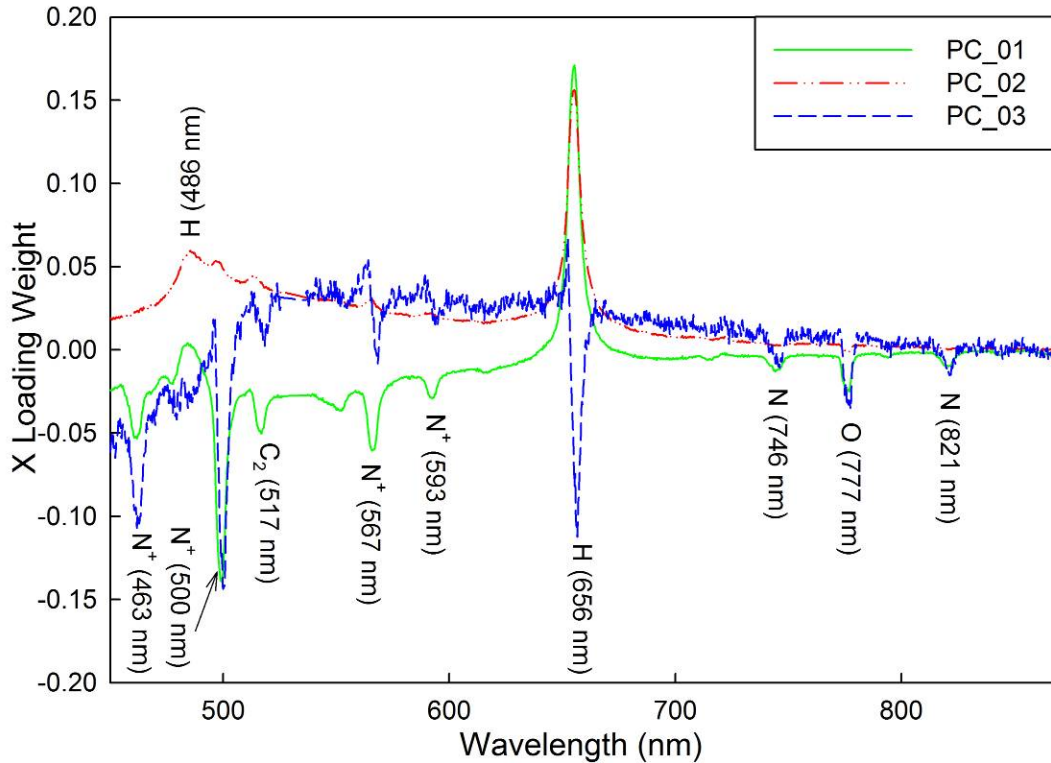


Figure 6.7

One-vector loading-weight plots for the developed PLS-R based multivariate calibration model on LIBS spectra

Comparison of the Predictive Power of LIBS Intensity Ratio Calibration, Multivariate LIBS Calibration, and Multivariate Chemiluminescence Calibration

The predictive power of the $H_{656 \text{ nm}}/N_{500 \text{ nm}}$ and $H_{656 \text{ nm}}/O_{777 \text{ nm}}$ intensity ratio calibration was tested with an unknown, independent data set that was collected separately. This data set consists of LIBS spectra collected at all the ten equivalence ratio

conditions that were considered for the development of the calibration model. Predictions from the $H_{656 \text{ nm}}/N_{500 \text{ nm}}^+$, $H_{656 \text{ nm}}/O_{777 \text{ nm}}$ intensity ratio calibration and the PLS-R based multivariate calibration are presented in Figure 6.8. For a similar range of equivalence ratios, the prediction results from the chemiluminescence-based multivariate calibration model developed in our previously reported work [18] are also shown in Figure 6.8. The chemiluminescence experiments were performed on the same setup under similar experimental conditions. A detailed description of the experimental parameters can be found in [18]. It is important to mention that the chemiluminescence and LIBS measurements were performed at slightly different locations (see inset Figure 6.1). The LIBS spectral data were collected from the secondary plasma that originated from the same spot where the chemiluminescence measurements were performed. Hence, it will provide equivalence ratio value at the same location as the chemiluminescence measurements.

Comparing the LIBS prediction results, it can be observed that the predictions from the $H_{656 \text{ nm}}/O_{777 \text{ nm}}$ intensity ratio calibration and the PLS-R based multivariate calibration closer to the 45 degree line (indicating perfect calibration) in comparison to the $H_{656 \text{ nm}}/N_{500 \text{ nm}}^+$ intensity ratio calibration. However, between the $H_{656 \text{ nm}}/O_{777 \text{ nm}}$ intensity ratio calibration and the PLS-R based multivariate calibration, one of the key advantages with multivariate calibration is that it does not involve intensity correction for the overriding continuum plasma emission. Also, the oxygen line at 777 nm has a relatively low intensity (see Figure 6.2). So in a noisy environment (with low signal-to-noise ratio), the intensity ratio calibration may lead to more erroneous predictions. On

the other hand, the multivariate calibration incorporates more spectral emissions (see Figure 6.7), which will improve the robustness of the calibration model.

Comparing the chemiluminescence-based prediction results with the LIBS-based prediction results, it can be clearly observed that the LIBS-based calibrations provide better predictions. The main reason behind this difference is that LIBS is a point measurement while chemiluminescence is a line-of-sight measurement. In LIBS, a laser pulse is tightly focused with a spot diameter of the order of a micron. Hence, the generated plasma carries spectroscopic information from a “point like volume”. On the other hand, in chemiluminescence the spectral information from the entire line-of-sight is collected by the collection lens. Therefore, it may be argued that while performing the LIBS experiment, the laser can be precisely focused in a very small control volume in the premixed zone resulting in more “local” measurements and better calibration/predictions.

Conclusions

An ungated LIBS detection methodology can provide a simple, robust, and cost effective tool to measure local equivalence ratios. In the present work, a comparative study of ungated LIBS based equivalence ratio measurements with chemiluminescence based equivalence measurement was performed in atmospheric methane-air premixed flames. The LIBS experiments were performed at ten different equivalence ratio conditions ranging from 0.74 to 1.42. To test repeatability, five experimental replications were performed for each equivalence ratio. Hydrogen (656 nm) to oxygen (777 nm) intensity ratio, hydrogen (656 nm) to nitrogen (500 nm) intensity ratio, and PLS-R based

multivariate calibration were developed and compared. The predictive power of the developed calibrations was tested with an unbiased data set and compared with chemiluminescence-based prediction of equivalence ratios. The major results can be summarized as follows:

- For ungated LIBS detection, a polarizer in the detection system can effectively suppress the elastically scattered laser light. The strong continuum background can be suppressed by collecting LIBS spectrum from the secondary plasma (i.e., a little away the primary laser plasma at the laser focal spot).
- The R^2 values for the hydrogen (656 nm) to nitrogen (500 nm) intensity ratio, hydrogen (656 nm) to oxygen (777 nm) intensity ratio, and PLS-R based calibration are 0.99, 0.99, and 0.98, respectively. The RMSEC for the hydrogen (656 nm) to nitrogen (500 nm) intensity ratio, hydrogen (656 nm) to oxygen (777 nm) intensity ratio, and PLS-R based calibration are 0.11, 0.02, and 0.04, respectively.
- For prediction of the unknown data set, the hydrogen (656 nm) to oxygen (777 nm) and PLS-R based calibrations provides better results in comparison to the hydrogen (656 nm) to nitrogen (500 nm) approach.
- The better predictions from the hydrogen (656 nm) to oxygen (777 nm) calibration compared to the hydrogen (656 nm) to nitrogen (500 nm) approach may be associated with higher sensitivity (due to higher slope) of the calibration line. The better prediction results from the PLS-R based calibration may be associated with the inclusion of several spectral lines in the

multivariate calibration. However, the low signal intensity associated with the oxygen line suggests that multivariate LIBS (PLS-R based) may provide better results in noisy environments when several spectral lines are included.

These results demonstrate that LIBS performs better in comparison to chemiluminescence-based equivalence ratio measurements. Multivariate sensing can provide a robust calibration by including several spectral lines. Also in multivariate calibration, there is no need of continuum background subtraction (due to plasma emission) which is normally required for the intensity ratio calibrations. This can allow easier sensing of equivalence ratios, where a raw LIBS spectrum can be directly fed to the multivariate calibration model.

Acknowledgments

This material is based upon work performed through the Sustainable Energy Research Center at Mississippi State University and is supported by the Department of Energy under Award Number DE-FG3606GO86025.

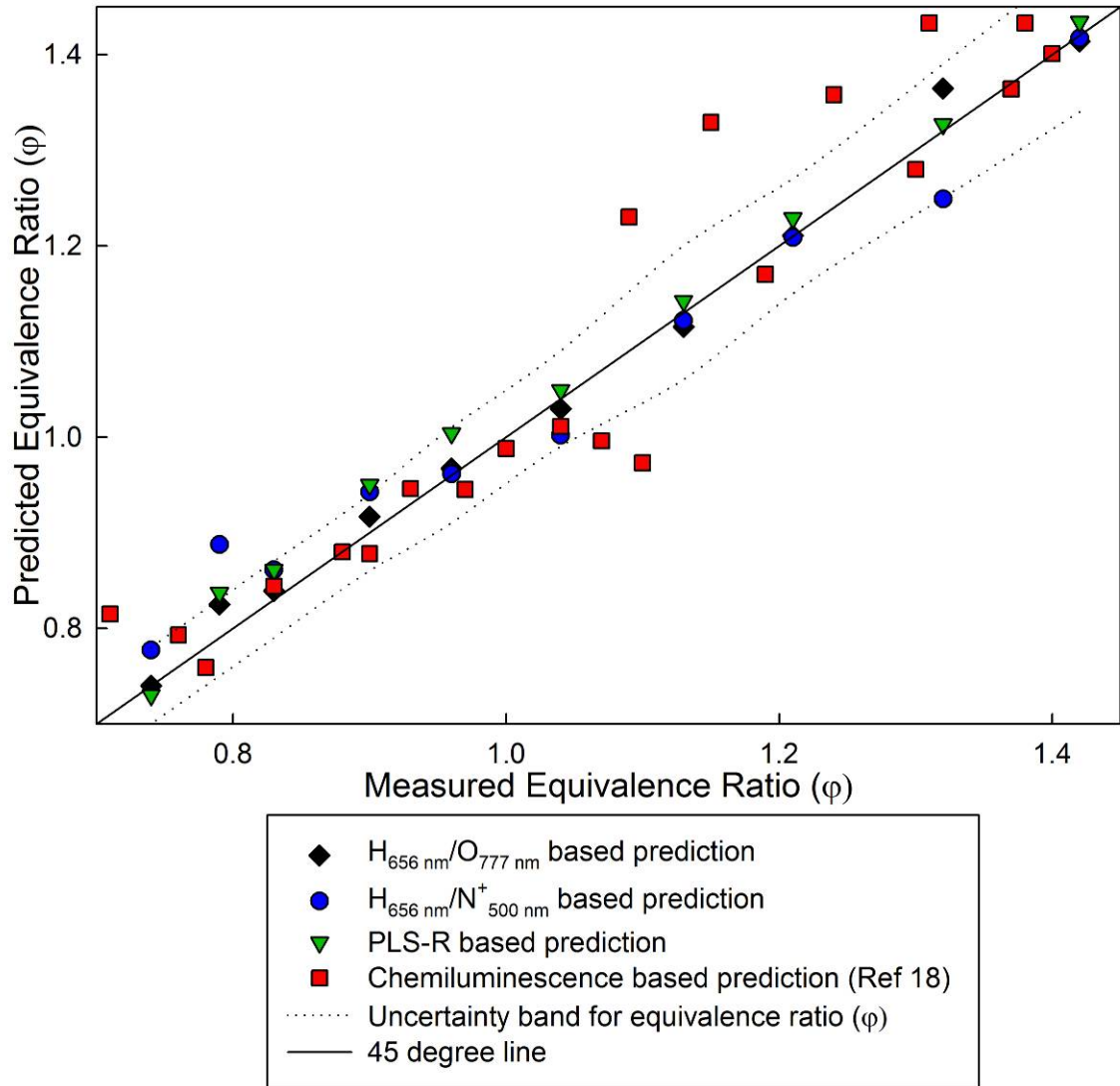


Figure 6.8

Prediction results from $H_{656 \text{ nm}}/N^+_{500 \text{ nm}}$ intensity ratio calibration, $H_{656 \text{ nm}}/O_{777 \text{ nm}}$ intensity ratio calibration, PLS-R based multivariate calibration, and Chemiluminescence based multivariate calibration

References

- [1] Singh JP, and Thakur SN. Laser-Induced Breakdown Spectroscopy. Elsevier Science B. V., 2007.
- [2] Miziolek AW, Palleschi V, and Schechter I. Laser-Induced Breakdown Spectroscopy (LIBS): Fundamentals and Applications. Cambridge University Press, 2006.
- [3] Kiefer J, Kozlov DN, Seeger T, and Leipertz A. Local fuel concentration measurements for mixture formation diagnostics using diffraction by laser-induced gratings in comparison to spontaneous Raman scattering. *Journal of Raman Spectroscopy* 2008; 39:711-721.
- [4] Singla G, Scouflaire P, Rolon C, and Candel S. Planar laser-induced fluorescence of OH in high-pressure cryogenic LO_x/GH₂ jet flames. *Combustion and Flame* 2006; 144: 151-169.
- [5] Phuoc TX, and White FP. Laser-induced spark for measurements of the fuel-to-air ratio of a combustible mixture. *Fuel* 2002; 81:1761-1765.
- [6] Zimmer L, Okai K, and Kurosawa Y. Combined laser induced ignition and plasma spectroscopy: Fundamentals and application to a hydrogen–air combustor. *Spectrochimica Acta Part B: Atomic Spectroscopy* 2007; 62:1484-1495.
- [7] Lee TW, and Hegde N. Laser-induced breakdown spectroscopy for in situ diagnostics of combustion parameters including temperature. *Combustion and Flame* 2005; 142:314-316
- [8] Ctvrtnickova T, Mateo MP, Yañez A, and Nicolas G. Laser Induced Breakdown Spectroscopy application for ash characterisation for a coal fired power plant. *Spectrochimica Acta Part B: Atomic Spectroscopy* 2010; 65:734-737.
- [9] Michalakou A, Stavropoulos P, and Couris S. Laser-induced breakdown spectroscopy in reactive flows of hydrocarbon-air mixtures. *Applied Physics Letters* 2008; 92: 081501 (3pp).
- [10] Joshi S, Olsen DB, Dumitrescu C, Puzinauskas PV, and Yalin AP. Laser-induced breakdown spectroscopy for in-cylinder equivalence ratio measurements in laser-ignited natural gas engines. *Applied Spectroscopy* 2009; 63:549-554.

- [11] Ferioli F, Puzinauskas PV, and Buckley SG. Laser-Induced Breakdown Spectroscopy for On-Line Engine Equivalence Ratio Measurements. *Applied Spectroscopy* 2003; 57: 1183-1189.
- [12] Eseller KE, Yueh FY, and Singh JP. Laser-induced breakdown spectroscopy measurement in methane and biodiesel flames using an ungated detector. *Applied Optics* 2008; 47: G144-G148.
- [13] Kiefer J, Tröger JW, Seeger T, Leipertz A, Li B, Li ZS, and Aldén M. Laser-induced breakdown spectroscopy in gases using ungated detection in combination with polarization filtering and online background correction. *Measurement Science and Technology* 2010; 21: 065303 (7pp).
- [14] Kiefer J, Tröger JW, Li ZS, Aldén M. Laser-induced plasma in methane and dimethyl ether for flame ignition and combustion diagnostics. *Applied Physics B* 2011; 103: 229–236.
- [15] Stipe CB, Hensley BD, Boersema JL, and Buckley SG. Laser-Induced Breakdown Spectroscopy of Steel: A Comparison of Univariate and Multivariate Calibration Methods. *Applied Spectroscopy* 2010; 64:154-160.
- [16] Yao S, Lu J, Zheng J, and Dong M. Analyzing unburned carbon in fly ash using laser-induced breakdown spectroscopy with multivariate calibration method, *Journal of Analytical Atomic Spectrometry* 2012; DOI: 10.1039/C2JA10229C.
- [17] Tripathi MM, Eseller KE, Yueh FY, Singh JP. Multivariate calibration of spectra obtained by Laser Induced Breakdown Spectroscopy of plutonium oxide surrogate residues. *Spectrochimica Acta Part B: Atomic Spectroscopy* 2009; 64:1212-1218.
- [18] Tripathi MM, Krishnan SR, Srinivasan KK, Yueh FY, and Singh JP. Chemiluminescence-based multivariate sensing of local equivalence ratios in premixed atmospheric methane–air flames. *Fuel* 2012; 93:684-691.
- [19] Esbensen KH. *Multivariate Data Analysis -in Practice*. 5th ed. Camo Inc; 2004.
- [20] Coleman HW, and Steele Jr. WG. *Experimentation and Uncertainty Analysis for Engineers* 2nd ed. John Wiley & Sons; 1999.
- [21] http://physics.nist.gov/PhysRefData/ASD/lines_form.html

CHAPTER VII

SUMMARY AND RECOMMENDATIONS FOR FUTURE RESEARCH

A summary of the dissertation work described in Chapter 2 through Chapter 6 on the development of different optical sensing methodologies for various energy applications is presented in this chapter. In addition, some recommendations for future work in this research area are also presented.

Research Summary

Chapter 2 discussed the development of a fiber-optic NIR system based on the reflection-absorption phenomenon for predicting water content in bio-oil. The usage of bio-oil obtained from fast pyrolysis of biomass as a future energy source is limited by the presence of water in its composition. A fast and effective technique for water concentration determination is essential for bio-oil upgrading by water removal. The developed NIR system successfully overcomes the sampling limitations posed by the dark and sticky nature of bio-oil. The feasibility of using the designed NIR system for estimating the water content in bio-oil was tested by applying multivariate analysis to the NIR spectral data (900–2100 nm range) obtained from bio-oils with varying levels of water content. Multivariate calibration models with two regression methods- principal component regression (PCR) and partial least squares regression (PLS-R)-were

independently developed. The calibration results demonstrated that spectral information can successfully predict the bio-oil water content (from 16% to 36%) with less than 1% error and with a high coefficient of determination ($R^2 = 0.98$).

The effect of ultraviolet (UV) exposure on bio-oil was studied in Chapter 3 by employing laser-induced fluorescence spectroscopy. A typical pyrolysis-derived bio-oil sample can contain up to 45% (by mass) of reactive organic chemical species, including alkenes, aldehydes, ketones, and carboxylic acids. These highly oxygenated compounds have a strong tendency toward condensation reactions, which can be easily catalyzed by UV exposure while in shipment and storage. Hence, understanding of the effect of UV exposure on bio-oil is important for its quality improvement. As part of this effort, a synthetic bio-oil composed of ten chemicals, but having similar weight percentage (wt%) of compound groups and having similar spectroscopic properties as bio-oil, was prepared. The synthetic bio-oil simplifies the limitation in the study posed by the complex chemical composition in raw bio-oil (which can contain up to 400 chemical compounds). The UV radiation incident on the earth surface contains ~98% UV-A (315-400 nm); therefore, this study focused on this part of the solar radiation spectrum. To simulate this condition, a laser in the UV region (325 nm) was employed for continuous bio-oil excitation. The laser-induced fluorescence spectrum (signal), as a signature of chemical change, was recorded at different times from bio-oil produced from four different sources (pine lumber, pine bark, oak bark, and oak wood) as well as from the synthetic bio-oil. From this study, it was concluded that the phenols present in bio-oil show chemical instability in the presence of UV exposure.

In Chapter 4, the design, development, and test results of a state-of-the-art laser-induced breakdown spectroscopy (LIBS)-based optical sensor to detect four important trace level impurities (nitrogen, argon, oxygen, and helium) in hydrogen is presented. Hydrogen is the fuel used by the National Aeronautics and Space Administration (NASA) for the Space Shuttle Main Engine (SSME), among others. The purity of the hydrogen fuel is very important for the performance of hydrogen-fueled engines. The sensor can simultaneously measure the concentrations of nitrogen, argon, oxygen, and helium in hydrogen fuel storage tanks and supply lines. LABVIEW[®]-based software was also developed to control and operate the optical sensor. The software performs data analysis on LIBS spectra and provides elemental concentrations (in ppm) of these impurities. The sensor has estimated lower detection limits of 80 ppm for nitrogen, 97 ppm for argon, 10 ppm for oxygen, and 25 ppm for helium.

Chapter 5 describes chemiluminescence-based multivariate sensing of local equivalence ratios in premixed atmospheric methane-air flames. Real time measurement of local and global fuel-air equivalence ratios (ϕ) is essential for monitoring and closed-loop control of combustion systems. It can help in reducing pollutants formed during the combustion process, preventing serious accidents in gas turbines due to blow-off or flash back, and employing advanced combustion strategies in internal combustion (IC) engines to improve engine efficiencies, among others. It has been observed that the chemiluminescence emissions from OH^* , CH^* , C_2^* , and CO_2^* formed within the reaction zone of premixed flames depend upon the fuel-air equivalence ratio in the burning mixture. In the chapter, a new partial least squares regression (PLS-R) based multivariate sensing methodology is investigated and compared with an OH^*/CH^* intensity ratio-

based calibration model for sensing equivalence ratio. Chemiluminescence data from nine different equivalence ratio conditions ranging between 0.73-1.48 (fuel-lean to fuel-rich) were collected to develop both calibration models. It was found that the equivalence ratios predicted with the PLS-R based multivariate calibration model matched the experimentally measured equivalence ratios within 7 percent; whereas, the OH^*/CH^* intensity ratio calibration grossly under-predicted equivalence ratios in comparison to measured equivalence ratios, especially under rich conditions ($\phi > 1.2$).

In Chapter 6, a comparative study of the equivalence ratio measurement in atmospheric premixed methane-air flames with ungated laser-induced breakdown spectroscopy (LIBS) and chemiluminescence is presented. In LIBS, a laser pulse is tightly focused on a spot with micron-sized diameter. Hence, the generated plasma carries spectroscopic information from a “point like volume” which can be advantageous for local equivalence ratio measurements. In ungated LIBS, the strong elastically scattered laser light greatly reduces the measurement dynamic range and sensitivity. For effectively suppressing the elastically scattered laser light in ungated LIBS detection, a polarizer and a notch filter in the signal collection system were tested. It was observed that a polarizer performed better in comparison to a notch filter in suppressing the elastically scattered laser light. The LIBS spectra collected at ten different equivalence ratios ranging from 0.74 to 1.42 were used to develop an equivalence ratio calibration model using atomic line intensity ratio, as well as broad spectral feature, with a partial least squares regression (PLS-R). The LIBS based prediction results were compared with chemiluminescence-based predictions from the same experimental setup. It was found that LIBS based calibration provided better predictions of equivalence ratios.

Recommendations for Future Research

Following are the list of future recommendations for the prospective researchers based on each chapter-

1. The research work in Chapter 2 has demonstrated that there is good potential in multivariate NIR spectroscopy for water concentration measurement of bio-oil. The current technologies available for determination of bio-oil water content are relatively time consuming and no method is available to make this process in real time during bio-oil production. A rapid water content determination in real time by on-line procedures would benefit the development of bio-oil upgrading technologies. The future work in this area should focus on the translation of multivariate NIR sensing methodology to develop a sensor for online water concentration determination during bio-oil production.
2. It is shown in Chapter 3 that the phenolic compounds present in the bio-oil degrade due to UV exposure. The photo-reactions involved in the degradation will be dependent on the intensity and duration of UV exposure. A detailed study is required to understand the dependence of reaction dynamics on intensity and duration of the UV exposure on chemical stability of phenols present in bio-oil. Presently, bio-oils are produced at laboratory scale and are stored in containers that can absorb UV. In future, these studies may help in better energy resource management of bio-oil during large-scale production of bio-oil in refineries.
3. A LIBS based prototype optical sensor was designed developed and tested in Chapter 4 for four major impurity measurements in hydrogen as a rocket fuel. This sensor was calibrated with the laboratory setup. To deploy this optical sensor in field, a

- series of test experiments need to be performed for proper calibration of the instrument in real time field environment. The test results can also suggest appropriate modifications in the sensor design to improve the ruggedness and robustness of the instrument. An uncertainty analysis needs to be performed to establish measurement accuracy of the LIBS instrument for trace impurity measurement. This designed sensor currently monitors only nitrogen, argon, oxygen, and helium in hydrogen but it can be easily modified to monitor other gaseous impurities as well.
4. The experimental results in the Chapter 5 demonstrate a proof-of-concept for the development of chemiluminescence based multivariate sensing strategies for monitoring and/or control of equivalence ratios in practical combustors respectively. One of the main challenges in employing chemiluminescence based sensing is to reduce the chemiluminescence sampling volume by employing advanced optical detection system such as Cassegrain optics. Further studies are required to evaluate the performance of the multivariate calibration model in high-pressure environments and for premixed flames with other fuels. Finally, the multivariate measurement methodology needs to be demonstrated and validated in practical premixed combustors.
 5. Chapter 6 demonstrates the application of multivariate ungated LIBS for local equivalence ratio measurement in premixed flames. For application of ungated LIBS in practical combustors, the feasibility of sending laser light and collection of LIBS signal in practical combustors without compromising with its performance need to be evaluated and studied. The application of LIBS can also be extended to measure the

flame temperature in premixed flames. For this effort, a study of the variation in threshold breakdown energy with equivalence ratio needs to be performed. After establishing a quantitative relationship between equivalence ratio and threshold breakdown energy, the measured flame temperatures (may be from the CH* chemiluminescence-based vibrational temperature measurement for methane air premixed flames) can be used to calibrate LIBS based threshold energy measurement to predict flame temperatures.